Atomistic Simulations of Perpendicular Shape Anisotropy MRAM

Wayne Lack

Doctor of Philosophy

University of York
Physics, Engineering and Technology

June 2024

Abstract

The continuous growth in demand for high performance computing necessitates that future random access memory (RAM) demonstrate low power consumption without sacrificing performance or reliability. A strong contender to fill this market is the non-volatile magnetic RAM (MRAM) based on a CoFeB-MgO-CoFeB magnetic tunnel junction. One of the CoFeB layers is pinned (reference layer), while the other CoFeB layer may reverse its magnetisation (free layer). These two allowed magnetic states represent the binary digits. Out of plane MRAM, whereby the diameter of the cell is larger than the CoFeB thickness, boasts a fast read-write time, relatively low power consumption and low bit-error rate. This technology is currently available on the market, but suffers from a loss of stability when the diameter is reduced to < 20 nm, thus the memory density of this design is not competitive. An alternative design, is to increase the thickness of the free layer until it is larger than the diameter, thus the shape anisotropy is directed in-plane. This design is known as perpendicular shape anisotropy MRAM (PSA-MRAM) and has the potential for retaining the benefits of the MRAM on the current market while reduced to competitive node sizes.

The magnetic behaviours, stability, and properties of PSA-MRAM at reduced volumes is seldom explored in the current literature. This thesis utilises an atomistic spin model approach to explore the dynamic and equilibrium properties of PSA-MRAM. The use of an atomistic model is noteworthy, as it sits in an ideal position between micromagnetic and ab-initio density functional theory approaches. The continuum approach of the former does not capture finite size,edge or thermal effects, while the latter is not appropriate for the number of atoms that makeup the system.

The results show a change in reversal mechanism as the free layer is reduced in an external field from incoherent domain wall motion to coherent rotation. The shape anisotropy as the free layer is reduced is significant, as are the finite size effects due to the loss of exchange on the surfaces. Further, when subjected to a current density rather than an external field, the reversal mechanism is further complicated by these properties. Additionally, thermal fluctuations are capable of partially driving the reversal mechanism for small PSA-MRAM structures.

Table of contents

List of tables

List of figures

Dedicated to Travis Lack, and of course, Steve Irwin.

Acknowledgements

First and foremost, I would like to thank my supervisors, Prof. Roy Chantrell and Dr. Richard Evans, without whom this work would not have been possible. Their continued guidance, patience, and friendship have been unfaltering throughout this journey.

I would also like to extend this thanks to the computational magnetism group at York for many fruitful talks, plenty of advice, and a friendly environment. A special thanks to Sarah, Andrea, Sergiu, Mara, Luke and Daniel who welcomed me and supported me from my very first days.

Of course, I would not be here in the first place without the support of my Mum, and my brothers, Alfie and Frazer. Thank you for always believing in me. I would also never be here without initial inspiration from Mr. Hawkridge, Dr. Cawley, Dr. Dwyer, and a particular episode of What's New Scooby-Doo.

Similarly, I am very grateful for the lifelong friendships I have made over the years, and the support and joy they have brought me before, during and inevitably after my PhD journey. I would not be where I am today without Mohan, Zebedee, Triv, Charis, Thorpy, Sam (Dennison), Jonathan and Sam (Wareham). An extra special shout out to Triv and Charis for letting me stay with them during the write-up phase! The thesis was put together through the motivation and support provided by my loving partner, Laura, who I forever thank. Without this focus during the final year, this thesis would not have come together in time, and you make me better every day.

Finally some honourable mentions that I simply can't leave out. The Vanbrugh football club, led at the helm by Matt Rayson, gave me some of the best memories of my PhD years. The music of NF, Muse, Lin-Manuel Miranda, Jorge Rivera-Herrans, Hans Zimmer and Murray Gold have carried me through hard times. Iron man, Sherlock, and the cast of Friends can also take some credit.

Finally, I gratefully acknowledge the support and the funding of EPSRC for a PhD studentship.

Declaration

I hereby declare that except where specific reference is made to the work of others, the contents of this dissertation are original and have not been submitted in whole or in part for consideration for any other degree or qualification in this, or any other university. The majority of this thesis has been presented at various conferences by the author, including:

- The European School of Magnetism, Cluj-Napoca, Romania, 6th-17th Sep, 2021
- IOP Magnetism 2021, York, UK, 28th-29th Mar, 2022
- Joint European Magnetism Symposium (JEMS), Warsaw, Poland, 24th-29th Jul, 2022

The results presented in Chapter 3 are published in the following article, W. Lack et. al. "Thermodynamic properties and switching dynamics of perpendicular shape anisotropy MRAM", Journal of Physics: Condensed Matter, 145801, 2024
The results presented in Chapter 4 are from a paper awaiting publication entitled "Magnetisation switching dynamics of perpendicular shape anisotropy, spin transfer torque MRAM"

1

Introduction

1.1 Motivation

In recent decades, high performance computing (HPC) has played a vital role in the advancement of science in a large number of fields. Subsequent advancements in science typically fuel a gradual but continuous requirement for both more powerful machines and more digital data storage. While this could initially be achieved with improvements to the clock speed, recent decades have seen a growth in the number of cores that make up a HPC system in addition to improved hardware [1]. As HPC clusters have grown in capacity and computing power, so has the related energy costs to power the machines. This has forced an increased focus on efficiency during the Petascale era of HPC machines, where power consumption of current Petascale machines can vary between around 0.6 MW - 16 MW depending on the size [2]. At the time of writing, exascale HPC clusters are expected within the next few years, where the target is to use <20 MW in initial designs. HPC clusters will undoubtedly continue to increase capacity during the exascale era and beyond, so the reduction of power consumption is critical to this progress [3]. A significant proportion of modern HPC energy usage (between $25\% - 40\%$ [4, 5]) is consumed by the memory system. Due to this, there is a lot of motivation to find an alternative memory technology that has a low power consumption while retaining the speed, reliability and density of current data storage techniques.

One of the most promising candidates is magnetic random access memory (MRAM), which stores the binary digit as a magnetic state, in contrast to dynamic or static random access memory (DRAM and SRAM) which use electrical charge. MRAM is thus a non-volatile memory, which would significantly reduce the power consumption of HPC clusters. The initial target for exascale machines is for the memory architecture to use $< 30\%$ of the allotted 20 MW power, which DRAM cannot satisfy [6, 7]. In addition to being non-volatile,

MRAM has the potential for rapid read and write operations comparable to SRAM, a high density due to scalability to small node size and a virtually infinite endurance. For this reason, MRAM has attracted significant research in recent years and is often referred to a 'universal memory' contender. Commercial MRAM technologies entered the market in 2016, and have since been developed and improved for scalability and improved performance by Everspin, Samsung and IBM, amongst others.
Despite all the advantages of MRAM, it has not yet reached its potential to become a universal memory. There are multiple proposed ways to switch the magnetic state, such as toggle memory (applied magnetic field), spin transfer torque (STT), spin orbit torque (SOT) and thermally assisted switching. None of these have yet satisfied the requirements for high density, low power consumption and reliability simultaneously. The stability of the switchable layer is intricately related to the shape, size and temperature of the device. The stability in turn dictates the strength of the applied field, or switching current, required to write a new binary state. To find the right balance for a universal memory requires a a complete understanding of the nanoscale physics involved, which is currently lacking. At such scales, experimental research is limited and requires the support of analytical or computational approaches. Molecular dynamics or density functional theory models have provided useful insight into the structure details, but are unable to model the number of atoms in a full MRAM node and capture magnetic properties. Micromagnetic models discretise a system into macrocells which will fail to capture the key behaviours that are caused by edge effects, finite size and thermal fluctuations. This thesis therefore uses an atomistic model to explore the currently unknown switching mechanics and magnetic properties MRAM devices.

1.2 The Origins of Magnetism

Magnetism has inspired human curiosity for thousands of years, and guided scientific advancement and progress over time. The earliest recorded statement on magnetism was a discussion of the naturally magnetised mineral, lodestone, and took place around 600 B.C. by Thales of Miletus and Aristotle [8]. Very little advancement was achieved in magnetism between this and the 19th century, with the exception of the invention of the compass (1100, Alexandar Neckham, though sources vary) and the realisation of the Earths magnetic field (1600, William Gilbert). In the 20th century, discovery of atomic-level phenomena provided the first significant progress in this field, with the discovery of quantum mechanical exchange and relativistic spin-oribt coupling [9]. It became increasingly clear that macroscale magnetic behaviour is governed by complicated nano-scale phenomena.

1.2.1 Magnetic Moment

Physically, magnetism on the atomic scale arises due to the localised polarisation of an atoms electron cloud, stemming from unpaired electrons. Each electron has a magnetic moment, usually measured in Bohr magnetons (μ_B), that arises primarily from its intrinsic quantum spin number. The magnetic moment of each atom, therefore, is the vector sum of the constituent electron moments. The magnitude of the magnetic moment is therefore dependent on the species of atom and the subsequent ordering and orientation of its constituent electrons. The interaction between the atomic magnetic moments of each atom will dictate how a material behaves magnetically on the macroscale.

1.2.2 Magnetic Ordering

Interactions between the magnetic moments of each atomic site can give rise to four types of atomic ordering in materials. The first case is diamagnetism, whereby each spin up electron cancels with a spin down electron, leaving no net magnetic moment if there are no unpaired electrons. Diamagnetic materials are thus non-magnetic. The other three orderings have a net magnetic moment due to unpaired electrons. The second example is paramagnetic, whereby the unpaired electrons are free to align their magnetic moments in any direction. Since these magnetic moments are random, a paramagnetic material has no significant net magnetic moment, but when an external magnetic field is aligned the unpaired electrons will align with the field. The third ordering is ferromagnetic, which is similar to paramagnetic as the unpaired electrons may align in any direction. However, unlike paramagnetism, the unpaired electrons in a ferromagnetic material have a tendency to align in parallel with each other for the lowest energy state. The fundamental difference, therefore, is that ferromagnetic materials have a net magnetic moment even in the absence of an external field. The final type of ordering is anti-ferromagnetic, which is characterised as having two sub-lattices with opposite magnetisation, which gives rise to a zero net magnetisation. This thesis will focus on ferromagnetic materials.

1.2.3 Spintronics

Modelling magnetic materials using the local magnetic moment, as is done in atomistic studies, can first be attributed to Ising in 1925 [10]. Throughout the 20th century, most theoretical models of magnetism, including the Bloch model, the Heisenberg model and the Stoner model, continued to use electron spin as a central component. However, it wasn't until the late 20th century ($\approx 1980s$) that it was realised that electron spin can be

utilised to read/write digital binary digits [11]. This followed the critical discoveries of spin polarisation and spin transport torque (STT), giant magnetoresistance (GMR) and magnetic tunnel junctions (MTJs). Utilising the spin of the electron in solid state electronic devices is a field of research known as spintronics, a portmanteau of spin and electronics. Some sources [12, 11, 13] suggest an earlier date for spintronics, in technologies such as spin field effect transistors (SPINFETs) and spin bipolar junction transistors (SBJTs). Here, the electron spin plays a secondary role in the functionality, while the binary information is still encoded using charge, so these earlier examples are referred to as hybrid spintronic. For this thesis, the only solid state technology of importance is magnetic RAM (MRAM), where the use of electron spin to encode the binary digits is key. This is sometimes referred to as monolithic spintronics, and has become increasingly researched as high performance atomistic studies became possible in recent decades [12].

1.3 MRAM: A History

Magnetic, or magnetoresistive random access memory (MRAM) is a solid state storage device that uses magnetic states to store binary data. This is in contrast to the most dominant random access memory technologies on the market that utilise electric charge to store binary data. Dynamic RAM (DRAM) consists of a transistor and a capacitor, which is relatively cheap and can be packed together for a high density. DRAM therefore makes up the majority of current computer memory architecture. Static RAM (SRAM) consists of multiple transistors, so has lower storage density than DRAM, while also being more expensive. However, it is faster than DRAM and comparatively lower power consumption, making SRAM the dominant form of CPU cache memory. Both DRAM and SRAM are volatile, since they use charge for data storage, resulting in inefficient power consumption in large scale high performance computing systems. MRAM is often considered a universal memory, as it is non-volatile while maintaining a good compromise of the listed benefits of both DRAM and SRAM. Namely, MRAM has the potential to be fast, with a low power consumption, quasi-infinite durability and scalable to competitive density storage. MRAM devices are readily combined with complimentary metal oxide semiconductor (CMOS) circuits for easy implementation with modern electronics [11]. At the time of writing, MRAM is manufactured on 28 nm CMOS and offers $1Gb$ with Everspins ST-DDR4.

1.3.1 Magnetic Tunnel Junctions (MTJs)

A magnetic tunnel junction (MTJ) is central to the design of an MRAM cell. MTJs consist of two ferromagnetic layers which are separated by a thin (between 1 nm - 2 nm) non-magnetic spacer layer. This is similar to spin-valves, but the non-magnetic spacer is an insulator in MTJs rather than metallic. Since the insulating non-magnetic layer is very thin, electrons may tunnel across from one ferromagnet to the other according to the laws of quantum mechanics. The amount of tunneling is dictated by the relative orientation of the two ferromagnetic layers. One of the ferromagnetic layers has a fixed magnetisation direction, referred to as the reference layer in this thesis (sometimes called the pinned layer in literature). The other ferromagnetic layer, called the free layer, is able to switch magnetisation direction between two opposite directions. The two ferromagnetic layers can therefore align parallel or anti-parallel. The parallel state offers low resistance, since the majority band electrons in one ferromagnet may tunnel to the next. In contrast, the anti-parallel alignment offers a comparatively large resistance. This is known as the tunnel magnetoresistance (TMR) effect, which results in significantly different resistance between the two states and allows the state of the MRAM cell to be read. TMR was initially suggest by Julliere in 1975 [14], but verified observation took around 20 years, being observed by Moodera and Miyasaki in 1995 [15, 16]. These early MTJs used Al_2O_3 as the spacer layer, as did the first release of MRAM to the mass market in 2006. Research on MTJs and the TMR effect continued in an attempt to find material combinations that would yield the highest TMR ratio while maintaining functionality. The largest step of progress since the early MTJs was in 2004/05 when it was discovered that an MgO spacer can yield much higher ratios (up to around 200% at the time) [17, 18]. Modern MRAM MTJs are made using CoFeB ferromagnets with an MgO spacer layer, which display TMR ratios in excess of 600% due to improved structural quality [11, 19].

1.3.2 Switching Techniques

Switching the free layer from one orientation to the other can be achieved via differing approaches, each of which has received, or is currently receiving, significant research attention. Examples of switching methods includes external field switching, spin transfer torque (STT), spin orbit torque (SOT) and thermally assisted switching. It is worth pursuing multiple options for switching because they differ on speed and potential scaling density as well as operational temperature range and ease of implementation. So far, two approaches have been commercialised, each with limitations on functionality.
First generation MRAM is considered as those that use an external field to switch the free

layer [20]. By placing a write line above and below the MTJ, a field can be applied that will switch the orientation of the free layer. The problem with this simple approach, is that neighbouring MTJs in a highly dense layout are also at risk of unwanted switching from the same field, a problem referred to as the half select problem [12]. An improved external field method, called Savtchenko switching, utilises a sequence of write currents that produce a rotating field. This is coupled with a different free layer design involving a synthetic anti-ferromagnet (SAF) structure. With this design, it is possible to switch the free layer of one bit without accidentally switching neighbouring MTJ units. A 4 MB Toggle MRAM using Savtchenko switching was released in 2006 and is the only approach from the first generation to reach mass production. The major benefit of field switched MRAM is the virtually infinite read/write durability, and high stability. However, reducing the dimension size increases the switching field distribution width and increase bit error rate. To reach competetive densities, MRAM must function reliably at reduced dimension size.
Second generation MRAM uses spin transfer torque (STT) as the reversal mechanism for the free layer. STT was first predicted, independently, by Slonczewski and Berger in 1996 [21, 22]. A current passing through the stable magnetised reference layer can become spin polarized due to the transfer of angular momentum from the local atomic moments with the itinerant current electrons. After tunneling through the MgO spacer layer, the spin polarised current can exert a torque on the atomic sites in the free layer and reverse its magnetisation direction [23, 20]. This approach benefits in a smaller cell size than the field switching while still being fast and reasonably efficient. 64MB STT-MRAM entered the market in 2016, with further advancement leading towards the release of the 256MB STT-MRAM cell and more recently a 1GB standalone STT-MRAM device [24, 25]. However, there are still unanswered questions and improvements to be made for STT-MRAM. The switching current, switching time and incubation time are all intricately dependent on the device dimensions and shape as well as thermally linked. To understand the reliability, performance and lifetime of STT-MRAM at reduced dimensions requires further research and will be explored in depth in chapter 4. A high switching current will result in large power consumption and increased eroding of the MgO tunneling layer. However, the free layer must remain stable enough to avoid unwanted thermally driven rotation. A more stable free layer will require a larger current to rotate, so a compromise must be found, requiring a more detailed knowledge of nanoscale behaviours.

1.3.3 Perpendicular Magnetic Anisotropy (PMA)

Using a disc shape structure, whereby the width of an MRAM cell is greater than the height, the shape anisotropy directs the magnetisation in-plane. The shape anisotropy is a

consequence of the demagnetising field, which gives a tendency for atoms to align along the longest axis. From early studies on spin transfer torque, it was clear that perpendicular magnetisation of the free layer would be more efficient than in-plane magnetisation. This is because if the magnetisation is in-plane, the spin current has to overcome the in-plane shape anisotropy caused by the demagnetising field, resulting in more power drawn per reversal [26, 27]. In contrast, perpendicular magnetisation for the structures in this thesis can align with the anisotropy, for greater thermal stability at reduced dimensions. It proved challenging, however, to produce material combinations that result in perpendicular magnetisation of the free layer. This was eventually overcome with the discovery of the CoFeB-MgO-CoFeB MTJ combination. Physicallly, the hybridisation of the overlapping orbitals from the interfacial Fe-3d and O-2p interactions results in perpendicular magnetic anisotropy (PMA). If the free layer is sufficiently thin, this perpendicular interfacial anisotropy emerges as dominant over the shape anisotropy, allowing perpendicular magnetisation of the free layer. The CoFeB-MgO-CoFeB material combination is the only known option allowing for perpendicular magnetisation while maintaining a sufficiently high thermal stability, high tunnel magnetoresistance (TMR) and a low writing current. This design is referred to as PMA-MRAM and is the design of the most recent MRAM on the market.

While PMA-MRAM has competitive performance and density, it is limited, as further reduction in the free layer thickness results in a critical reduction in the thermal stability. The dimensions can be further reduced by introducing a second MgO layer, thus providing more PMA to the free layer. The resulting MTJs, which are disc shaped, can reach around 20 nm diameter, which is what is found on the commercial market at present. However, double MgO structures are not compatible with spin orbit torque (SOT) technologies, and reduction to cell sizes of less than 20 nm is the target of ongoing research.

1.3.4 Perpendicular Shape Anisotropy (PSA)

An alternative design, is to create tower like structures, whereby the height of the MRAM cell is greater than its width. In these circumstances, the shape anisotropy will now align perpendicular rather than in-plane. The resulting structures are referred to as perpendicular shape anisotropy MRAM (PSA-MRAM) and are the focus of this thesis. The shape anisotropy and the perpendicular magnetic anisotropy stemming from the Fe-O interaction are now along the same direction, rather than resisting each other. This provides sufficient thermal stability even at reduced sizes, and it is expected that PSA-MRAM can scale to sub-10 nm MTJs. Since the magnetisation direction is still perpendicular, this design is compatible with STT switching.

For commercial advancement, however, it is still unknown if the PSA-MRAM design can

achieve industrial validity. Firstly, the thermal stability must remain above industry targets for a wide range of operational temperatures. If the thermal stability is too low, the bits may become randomly reversed due to thermal fluctuations, which results in corrupted data. To satisfy industry criteria, PSA-MRAM should have a long term data retention rate of around 10 years. Secondly, the switching current required should be as low as possible. This is motivated partly for efficiency, as a large current would draw large amounts of power, reversing the benefits of a non-volatile storage technique. Additional motivation is that a large current is known to degrade the MgO layer over time. This leads to a reduced lifetime of the device, which may become prohibitively small. It also reduces the efficiency of the cell due to a lowered tunnel magnetoresistance (TMR), since the TMR ratio is heavily influenced by the crystal structure. A precise relationship between the thermal stability, cell volume size, switching current and temperature are currently unknown. More understanding of these intricate behaviours and properties is required before PSA-MRAM becomes a viable technology at competitive densities.

1.4 Modelling Methods

The most important criteria to consider when choosing a modelling method in magnetism are the length and time scale of the simulations. Short time and length scales may utilise first principle quantum mechanical formulations, but are too computationally expensive to extend to larger systems. On the other extreme, large time and length scales typically use a continuum micromagnetic approach. Between these extremes, classical atomistic modelling methods may be used.

On the short time and length scales, the quantum mechanical (ab-initio) formulation can determine the fundamental electronic properties of a system from the wave functions. Examples include density functional theory (DFT) and Green's function approaches. These methods have been used in the study of MRAM to determine the exchange energy, anisotropy energy, magnetic moment and various components of STT. However, due to the complexity of the models, these approaches are limited to only a few hundred atoms. These models are therefore unable to determine the behaviours and macroscale properties of complete nanoscale MRAM structures.

To model systems that consist of between $10^4 - 10^9$ atoms, for time scales up to the nanosecond regime, atomistic models are more appropriate. Here, each atomic site is treated as a local atomic magnetic moment, where the first and most simple atomistic approach was described by Ising [10]. The natural evolution of the Ising model is the Heisenberg model, which allows the magnetic moment to move in 3D, but each moment is

still affiliated with a localised atomic site. The Heisenberg model can also readily include thermal effects which can have a large impact on the properties and behaviours of nanoscale devices. Macroscopic properties, such as the energy and Curie temperature can be inferred from atomistic approaches by averaging over all the atomic sites. Equilibrium properties are accessed via Monte Carlo methods, but dynamic properties are also calculable using the Landau-Lifshitz-Gilber (LLG) equation [28].
For larger time-scales and length scales, micromagnetic continuum approaches are used. These do not capture the atomic scale details, instead treating the physical parameters as continuous. This is because, in a large enough system, neighbouring atomic sites can be approximated as perfectly aligned due to the exchange constant, thus the system can be discretised in to macrocells. This approach is therefore unable to capture material boundaries, surface effects, thermal fluctuations or material doping.
This thesis focuses on modelling nanoscale magnetic tunnel junctions for PSA-MRAM and uses an atomistic approach. The number of atoms in the structures studied in this thesis are too large for ab-intio approaches, but thermal fluctuations and finite size effects have significant impact on magnetic properties. This thesis utlises results found from previous ab-initio studies on CoFeB-MgO boundaries. All results in this thesis use the atomistic spin model implemented in the VAMPIRE software package [29, 30].

1.5 Thesis Outline

Perpendicular shape anisotropy MRAM is a novel design that could represent the next major step towards MRAM becoming a universal memory. However, to ensure the best compromise of a fast switching speed, low writing current and a large thermal stability factor, all at reduced volume, the nanoscale behaviours and properties must be understood. In this thesis, an atomistic study on the CoFeB-MgO PSA-MRAM tower structures is carried out to obtain an intricate overview of the magnetic properties.
First, the atomistic model implemented in the VAMPIRE software package is described. Then, the thermodynamic properties and switching mechanics of PSA-MRAM are studied to investigate a size dependence on the magnetic behaviours. While this is done using an external magnetic field, the following chapter uses STT to drive the magnetic reversal. The dynamics of PSA-MRAM under STT have not been detailed in literature at the time of writing. Finally, the energy barrier between the two magnetic states for PSA-MRAM is obtained, providing key insights into the validity PSA-MRAM of very small diameter and guiding future design.

2

Atomistic Spin Model

In this thesis, we have performed atomistic spin dynamics simulations using the VAMPIRE open source software package, freely available at [29]. In the following chapter, the atomistic spin model used in VAMPIRE is discussed. We start by outlining the fundamentals of the spin Hamiltonian, governing the energetics of the system and fundamentally arising from quantum mechanics. This is followed by a description of the integration techniques used to capture the dynamics of magnetic systems, including time evolution and thermal effects, which are treated classically [30]. The model for spin transfer torque is then described, allowing the dynamics of the spin accumulation to be discussed separately from the dynamics of the magnetic moment. These effects are solved self-consistently in the code, however, so these are separated only for the readers clarity. Finally, this chapter ends with the parameterisation of our MRAM towers used in the subsequent chapters.

2.1 Generalised Heisenberg Hamiltonian

The spatial and temporal evolution of magnetic spins in a system can be evaluated by considering the energetics of the system. In magnetism, the different forms of energy are caused by various interactions between the magnetic moments of the spins in the system. The total energy can be summarised by the Heisenberg Hamiltonian equation as the sum of individual components as follows;

$$\mathscr{H} = \mathscr{H}_{\text{exc}} + \mathscr{H}_{\text{ani}} + \mathscr{H}_{\text{app}} + \mathscr{H}_{\text{dip}} \tag{2.1}$$

The four terms from left to right describe the exchange energy between spins ($\mathscr{H}_{\text{exc}}$), the magnetic anisotropy per atom ($\mathscr{H}_{\text{ani}}$), the interaction between the externally applied magnetic field and the local magnetic moment ($\mathscr{H}_{\text{app}}$) and the magnetostatic dipolar interaction ($\mathscr{H}_{\text{dip}}$).

We outline these individual terms in detail in the following subsections, then the method for integrating this equation is described.

2.1.1 Exchange Energy

The first term in the Hamiltonian (Equation 2.1) is the Heisenberg exchange interaction and is the largest energy contribution in our system responsible for macroscopic ordering of spins. It is a quantum mechanical effect resulting from the Pauli exclusion principle [1] [31], first interpreted by Heisenberg and Dirac in the context of Schrodinger's equation for more than one particle [32, 33]. We now derive the exchange interaction by considering the simple case of two electrons on different atoms, a and b interacting. Electron a is in state $\psi_a(\mathbf{r}_1)$ at some position $\mathbf{r}_1$, while b will similarly be in state $\psi_b(\mathbf{r}_2)$ at position $\mathbf{r}_2$. There then must be a joint wavefunction that is a linear combination of the two individual states, $\Psi(\mathbf{r}_1,\mathbf{r}_2) = \psi_a(\mathbf{r}_1)\psi_b(\mathbf{r}_2)$, that will satisfy the Schrodinger equation

$$\left[-\frac{\hbar}{2m}\nabla_1^2 - \frac{\hbar}{2m}\nabla_2^2 + V(\mathbf{r}_1) + V(\mathbf{r}_2)\right]\Psi(\mathbf{r}_1,\mathbf{r}_2) = E\Psi(\mathbf{r}_1,\mathbf{r}_2) \tag{2.2}$$

where $\hbar$ is the reduced Plank's constant, m is the mass, $V(\mathbf{r})$ is the potential at point $\mathbf{r}$ and $E = E_a + E_b$ is the total energy of the two electrons. Since the electrons must be indistinguishable, $\psi_a(\mathbf{r}_2)\psi_b(\mathbf{r}_1)$ must also be a solution to the Schrodinger equation. This holds only if $\Psi(\mathbf{r}_1,\mathbf{r}_2) = \Psi(\mathbf{r}_2,\mathbf{r}_1)$ or $\Psi(\mathbf{r}_1,\mathbf{r}_2) = -\Psi(\mathbf{r}_2,\mathbf{r}_1)$ is true. These represent a symmetric and an anti-symmetric wavefunction respectively. We can reject the symmetric identity due to Pauli's exclusion principle, so we are now left with the anti-symmetric wavefunction for the rest of the derivation. For the rest of this derivation, we follow the work of Blundell [34]. We can divide the electrons wavefunction into two components, a radial component $\phi(\mathbf{r})$ and a spin component χ such that $\psi = \chi\phi(\mathbf{r})$. Since we are dealing with an anti-symmetric wavefunction, either the spin component is symmetric and the radial component is anti-symmetric, or vice versa. The spin component then takes one of two states, where the anti-symmetric case represents a singlet state with total quantum spin $(S = 0)$, and the symmetric case is a triplet state with total spin $(S = 1)$. The singlet state represents all electrons being paired up, while the triplet state represents two unpaired electrons [35]. We

[1] The Pauli exclusion principle states that no two fermions in the same quantum system can be in the same quantum mechanical state.

therefore have two possible wavefunctions for the singlet Ψ_S and triplet Ψ_T state as follows

$$\begin{aligned}\Psi_S &= \frac{1}{\sqrt{2}}\Big[\phi_a(\mathbf{r}_1)\phi_b(\mathbf{r}_2)+\phi_a(\mathbf{r}_2)\phi_b(\mathbf{r}_1)\Big]\chi_S,\\ \Psi_T &= \frac{1}{\sqrt{2}}\Big[\phi_a(\mathbf{r}_1)\phi_b(\mathbf{r}_2)-\phi_a(\mathbf{r}_2)\phi_b(\mathbf{r}_1)\Big]\chi_T\end{aligned} \tag{2.3}$$

containing both the spatial and the spin components. The energies for both states can be found using the Heitler-London approximation [36] and are given by

$$\begin{aligned}E_S &= \int\int \Psi_S^* \mathscr{H} \Psi_S d\mathbf{r}_1 d\mathbf{r}_2,\\ E_T &= \int\int \Psi_T^* \mathscr{H} \Psi_T d\mathbf{r}_1 d\mathbf{r}_2\end{aligned} \tag{2.4}$$

(where the spin components χ_S and χ_T are assumed to be normalised). The difference in these energies is then given by

$$J = E_S - E_T = 2\int\int \phi_a^*(\mathbf{r}_1)\phi_b^*(\mathbf{r}_2)\mathscr{H}\phi_a^*(\mathbf{r}_2)\phi_b^*(\mathbf{r}_1)d\mathbf{r}_1 d\mathbf{r}_2 \tag{2.5}$$

The difference between the singlet and the triplet state can be parameterised using $\mathbf{S}_1 \cdot \mathbf{S}_2$, where $\mathbf{S}_1$ and $\mathbf{S}_2$ are the spin operators for electron a and b respectively. For a singlet state, $\mathbf{S}_1 \cdot \mathbf{S}_2 = -\frac{3}{4}$, whereas for the triplet state, $\mathbf{S}_1 \cdot \mathbf{S}_2 = \frac{1}{4}$. We can now write an effective Hamiltonian as $\mathscr{H} = \frac{1}{4}\Big(E_S + 3E_T\Big) - \Big(E_S - E_T\Big)\mathbf{S}_1 \cdot \mathbf{S}_2$. This Hamiltonian consists of two terms, the first is a spin-independent radial term and can be absorbed into other energy constants while the second is a spin-dependent term. The spin-dependent term represents the exchange energy between the two electrons, and from Equation 2.5, we arrive at our final expression for the exchange energy Hamiltonian of two electrons a and b as

$$\mathscr{H}_{\text{exc}} = -J\mathbf{S}_1 \cdot \mathbf{S}_2 \tag{2.6}$$

If $J > 0$, then $E_S > E_T$ and the triplet state (S=1) will be favoured resulting in the two spins aligning in parallel. Else, if $J < 0$, $E_S < E_T$ and the singlet state (S=0) will be favoured resulting the spins aligning anti-parallel. This demonstrates how the exchange term of the Hamiltonian is responsible for macroscopic ordering of the spins, even in this simple system of two electrons. This concludes our derivation following the work of Blundell [34].

For a real system, each atom has more than one electron, and the system consists of thousands of atoms even at the nanoscale. The interactions between all of these electrons should be considered, but a mathematical description for many-body systems rapidly becomes intractable. One approach to address this problem is to extend the Heisenberg interaction

derived above to allow all interactions to be treated as pairs of electrons. To accomplish this, the spin at each atomic site in an atomistic model is the net spin of all electron spins and orbital contributions. This is an example where the model parameters are preferably calculated using DFT models. Equation 2.6 is then extended to an atomistic approach, using **S** to denote the net atomic spin, and thus becomes

$$\mathscr{H}_{\text{exc}} = -\sum_{i \neq j} J_{ij} \mathbf{S}_i \cdot \mathbf{S}_j \tag{2.7}$$

where the summation includes all interactions in the system without double counting, and J_{ij} is the exchange coupling constant between spin i and j. The exchange constant can be determined, at least in principle, for any given material from ab-initio methods. Using Equation 2.7, the interaction between every spin and every other spin could be calculated, but for a system with thousands of atoms (or more) this would be extremely computationally expensive, so it is usual to truncate to nearest neighbours only. This is a valid approximation for most materials since the exchange constant has a strong distance dependence, so nearest neighbours present the dominant interaction.

Equation 2.7 represents the simplest first order case where the exchange constant J_{ij} is a scalar value. In this isotropic case, the exchange only depends on the two spins relative orientation to each other and not their direction [30]. In more complicated systems, the exchange forms the tensor:

$$J_{ij} = \begin{bmatrix} J_{xx} & J_{xy} & J_{xz} \\ J_{yx} & J_{yy} & J_{yz} \\ J_{zx} & J_{zy} & J_{zz} \end{bmatrix} \tag{2.8}$$

In the second order case, the non-diagonal components of the exchange matrix of Equation 2.8 are zero, representing two-ion anisotropy exchange (if the diagonal components are not equal) [37]. In the third order case, all the terms of the matrix are filled representing the Dzyaloshinskii-Moriya exchange found in magnetic configurations [38]. For the second and third order cases, Equation 2.7 is rewritten as

$$\mathscr{H}_{\text{exc}} = -\sum_{i \neq j} \begin{bmatrix} \mathbf{S}_x^i & \mathbf{S}_y^i & \mathbf{S}_z^i \end{bmatrix} \begin{bmatrix} J_{xx} & J_{xy} & J_{xz} \\ J_{yx} & J_{yy} & J_{yz} \\ J_{zx} & J_{zy} & J_{zz} \end{bmatrix} \begin{bmatrix} \mathbf{S}_x^j \\ \mathbf{S}_y^j \\ \mathbf{S}_z^j \end{bmatrix} \tag{2.9}$$

2.1.2 Anisotropy

The second term in the Hamiltonian (Equation 2.1) is the anisotropy energy term. While this term is generally weaker than the exchange term, the anisotropy is the property responsible

for the directional preference for the atomic moments to align along. This is more challenging to obtain from DFT models and is often compared with experimental results. A material with a high anisotropy would normally have a high coercivity, while a material with low anisotropy has a low coercivity and would be easier to demagnetise. Anisotropy is a strongly temperature dependent property, the thermal stability of a material is therefore dictated by its total anisotropy [30]. There are multiple origins for the anisotropy in a magnetic system but for most materials the main source is the magnetocrystalline anisotropy. This arises from the interaction between the spin-orbit coupling of the magnetic moment and the local crystal field. The spin-orbit coupling arises from the spin of the electron interacting with its own magnetic field created by its motion around the nucleus [39]. Since this field interacts with the local crystal field, the magnitude of the resultant magnetocrystalline anisotropy depends on the competing strengths of these interactions. If the spin-orbit coupling is larger than the local crystal field, the orbital moment is relatively unquenched and there will be a large anisotropy. Similarly, if the local crystal field is larger than the spin-orbit coupling there will be a weaker anisotropy. The crystal field is related to the crystal ordering of atomic sites, and the magnetic moments of the elements at these atomic sites. The origin of the resulting magnetocrystalline anisotropy is therefore dependent on the shape and symmetry of the material. It will favour aligning spins along one crystallographic direction if the system is not symmetric in each direction along the crystal structure [40]. In the simplest case, the spins prefer one direction which is called the easy axis. This form of crystalline anisotropy is known as uniaxial anisotropy and is given by

$$\mathscr{H}_{\text{ani}} = k_u \sum_i (\mathbf{S}_i \cdot \mathbf{e})^2 \tag{2.10}$$

where k_u is the uniaxial anisotropy constant per atom and $\mathbf{e}$ is a unit vector in the direction of the easy axis.

2.1.3 External Applied Magnetic Field

The third term of Equation 2.1 describes the energy resulting from the interaction between the local spins and an externally applied magnetic field ($\mathbf{H}_{\text{app}}$). This interaction causes a torque on the local spins that could be used to switch the magnetisation of the system. The external field $\mathbf{H}_{\text{app}}$ could be stray fields from neighbouring magnetic materials systems or could be the field emanating from a current. The energy of this interaction is often called the

Zeeman energy [41] and is given by the coupling of the system with the external field as

$$\mathscr{H}_{\text{app}} = -\mu_s \sum_i \mathbf{S}_i \cdot \mathbf{H}_{\text{app}} \tag{2.11}$$

where μ_s is the spin magnetic moment and $\mathbf{H}_{\text{app}}$ is the field given in Tesla.

2.1.4 Dipole Interaction

The final term of Equation 2.1 is the magnetostatic term, sometimes called the dipolar energy or the demagnetising term, which governs the shape anisotropy of the system. This is particularly important for systems that have one dimension significantly larger than the others, or that are larger than the single domain limit of the material. The PSA-MRAM structures studied in this thesis are all taller (z-dimension) than they are wide (x-y plane) in order to introduce the perpendicular shape anisotropy, so capturing the effects of the dipole field is essential for this feature. The demagnetising field may be physically interpreted as a distribution of so called "bound" currents, if every dipole is imagined as a tiny current loop. Firstly, for a uniformly magnetised material, the internal current loops would cancel, since every dipole on the right side of its loop would be canceled by one on its left across many lattice points. However, the dipoles that are at the edge of the material will not cancel, so there is equivalent to a surface current around the material. To be clear, no current is actually flowing, there are only small residual current loops at each surface dipole which acts as if a current is flowing, thus a field will be produced. Following this physical interpretation, for a non-uniform magnetised material, the interior currents will not cancel either, again producing the effect of a current, without any current actually flowing. The demagnetising field is thus a consequence of the distribution of the dipoles themselves [42–44]. An expression for this field is obtained following Maxwell's equations (with the derivation found in [44]) as

$$\mathbf{H}(\mathbf{r}) = \frac{1}{4\pi}\Big[\int_V \frac{\mathbf{r}-\mathbf{r}'}{|\mathbf{r}-\mathbf{r}'|^3}\mathbf{J}_b(\mathbf{r}')dV + \int_S \frac{\mathbf{r}-\mathbf{r}'}{|\mathbf{r}-\mathbf{r}'|^3}\mathbf{K}_b(\mathbf{r}')da\Big] \tag{2.12}$$

where $\mathbf{J}_b = \nabla \times \mathbf{M}$ is the bound volume current and $\mathbf{K}_b = \mathbf{M} \times \hat{\mathbf{n}}$ is the bound surface current. This equation is not solvable analytically (apart from a few simple cases) but is a reasonable inclusion for outlining the origin of magnetostatic interactions. This aids with the following subsection, which outlines the dipolar fields implementation in VAMPIRE.

On a microscopic scale, the magnetic field originating from magnetostatic effects fluctuates constantly and rapidly, from one lattice space to the next. Clearly, the dipole interaction is a long range interaction between all spins, i, with all other spins, j. However, unlike the exchange energy, the strength of the dipolar field scales with $1/r_{ij}^3$, (where r_{ij} is the distance

between dipole i and j), so can not be truncated to a nearest neighbours approximation without sacrificing significant accuracy [45]. Still, it is too computationally expensive, and requires too much memory, to calculate atomistically for systems consisting of more than a few hundred atomic sites, so a micro-magnetic like approach is required. This approach discretises the system into macrocells, made up of multiple atomic sites, which are treated as having a uniform magnetisation (macrocells must be significantly smaller than the domain wall of the material for this assumption). Each macrocell is then treated as a point dipole, and the summation of these dipoles is used to calculate the dipole field. This approximation is almost as accurate as the atomistic calculation for a nanoscale device, since on the length-scale of a typical macrocell (a couple of atomic spacings), the exchange field discussed in subsection 2.1.1 is dominant, while the demagnetising fields are most impactful on the nanoscale, so the effect of neglecting the dipole at an atomistic resolution is minimised [46]. The dipolar energy enters the Hamiltonian of Equation 2.1 as the interaction between the spins and the dipole field

$$\mathscr{H}_{\text{dip}} = -\frac{1}{2}\sum_{i}\mu_s \mathbf{B}_{dip}\cdot\mathbf{S}_i \tag{2.13}$$

where μ_s is the atomic spin moment and $\mathbf{B}_{\text{dip}}$ is the dipole field. For atomistic resolution, the formula for the dipolar field is given by the summation over all magnetic moments as

$$\mathbf{B}_{\text{dip}} = \frac{\mu_0\mu_s}{4\pi}\sum_{i\neq j}\Big[\frac{3(\hat{\mathbf{r}}_{ij}\cdot\mathbf{S}_i)(\hat{\mathbf{r}}_{ij}\cdot\mathbf{S}_j)-(\mathbf{S}_i\cdot\mathbf{S}_j)}{r_{ij}^3}\Big] \tag{2.14}$$

where μ_0 is the permeability of free space, $\hat{\mathbf{r}}_{ij}$ is the unit vector from lattice point i to j, and r_{ij} is the distance between the spins $\mathbf{S}_i$ and $\mathbf{S}_j$.

We must first modify Equation 2.14 to sum the contributions from macrocells, rather than atomistic resolution atomic sites, which is described by the bare-macrocell approach. Let us start by describing the position of each macrocell, which will be saved as an array for efficient parallel computation in VAMPIRE. The position of each macrocell is given by the 'centre of mass', to account for macrocells that may be partially filled, for more complicated (non-cuboidal) shapes. This also allows intermixing of different materials that may contribute different magnetic moments within a given macrocell. The position of the macrocell, p_{mc}, is given by

$$p_{mc} = \frac{\sum_i^n \mu_i \overrightarrow{p_i}}{\sum_i^n \mu_i} \tag{2.15}$$

where n is the number of atoms in the macrocell, μ_i is the atomic spin moment of the atomic site i, and $\overrightarrow{p_i}$ is the position vector of each individual moment in the macrocell. The magnetic moment of each macrocell, $\mathbf{m}_{mc}$is then calculated as the sum of the individual atomistic

moments that make it up, given by

$$\mathbf{m}_{mc} = \sum_{i}^{n} \mu_i \overrightarrow{S_i} \tag{2.16}$$

where n and μ_i are as before, and $\overrightarrow{S_i}$ is the unit spin vector at each atomic site i. The demagnetisation field of one macrocell p, using the bare-macrocell approach, is then given by

$$\mathbf{B}^p_{\text{dip}} = \frac{\mu_0}{4\pi}\Big(\sum_{p\neq q} \frac{3\hat{r}_{pq}(\hat{r}_{pq}\cdot\mathbf{m}^q_{mc}) - \mathbf{m}^q_{mc}}{r^3_{pq}}\Big) - \frac{\mu_0}{3}\frac{\mathbf{m}^p_{mc}}{V^p_{mc}} \tag{2.17}$$

where we have reserved p and q as the indices of the macrocells. In the first term, similar to Equation 2.14, $\hat{r}_{pq}$ is the unit vector between macrocells p and q, while r_{pq} is the distance between macrocells p and q, and $\mathbf{m}^q_{mc}$ is the total magnetic moment of macrocell q. This first term thus represents the dipole interaction between the macrocell p and all the other macrocells in the system. We now have a secondary term, where $\mathbf{m}^p_{mc}$ is the total magnetic moment of macrocell p, and $V^p_{mc} = n^p_{mc}\frac{V_{uc}}{n_{uc}}$ is the volume of macrocell p, calculated from the number of atoms in the macrocell, n_{mc}, the number of atoms in a unit cell, n_{uc}, and the volume of a unit cell V_{uc}. This term represents the self-demagnetising field of macrocell p with itself, where the $\frac{1}{3}$ is derived for a macro-cell with a cubic shape, as the point-dipole approach yields a Lorentz field (the continuous Maxwellian internal field for a sphere has coefficient $\frac{2}{3}$) [47, 45]. By collating terms, it is possible to construct a demagnetising tensor, $\bar{D}$, for the geometric relationships between pairwise interactions in term one of Equation 2.17, given by

$$\bar{D}_{pq} = \frac{\mu_0}{4\pi r^5_{pq}}\begin{bmatrix} 3r_x^2 - r_{pq}^2 & 3r_x r_y & 3r_x r_z \\ 3r_y r_x & 3r_y^2 - r_{pq}^2 & 3r_y r_z \\ 3r_z r_x & 3r_z r_y & 3r_z^2 - r_{pq}^2 \end{bmatrix} \tag{2.18}$$

where r_x, r_y and r_z are the components of the unit vector in the direction $\overrightarrow{pq}$, and r_{pq} is the separation of the macrocells. The off-diagonal components of this matrix are symmetric ($xy = yx$ etc.), so only six numbers need be stored in memory rather than nine, improving efficiency. Equation 2.17 can then be rewritten more compactly in terms of the demag tensor as:

$$\mathbf{B}^p_{\text{dip}} = \sum_{p\neq q} (\bar{D}_{pq}\cdot\mathbf{m}^q_{mc}) - \frac{\mu_0}{3}\frac{\mathbf{m}^p_{mc}}{V^p_{mc}} \tag{2.19}$$

Once the field has been calculated for all macrocells in this approach, it is then applied to all atoms within each macrocell as an effective field, concluding the bare-macrocell approach [30].

In the PSA-MRAM structures studied in this thesis, there are multiple materials with differing magnetic parameters and therefore a complicated interaction between the close proximity layers. The bare-macrocell approach is not suited to capture sharp interfaces, due to its complete discretisation into macrocells. In this thesis, an extension to the bare-macrocell approach outlined above is used, known as the inter-intra dipole algorithm, and follows the approach of Bowden et al. [48]. Like the bare-macrocell approach, the system is first discretised into macrocells, but in this modified approach, neighbouring macrocells may be computed with atomistic resolution, which allows the magnetostatic interaction between sharp interfaces to be captured. A key difference in this modified bare-macrocell approach, is the dipole matrix now retains the key atomic information (such as the atomic positions, magnetic moments and spin directions for all atomic sites) as real-space coordinates. One benefit of this, is the macrocells can now be any shape, and the centre does not need to be adjusted for edges of the system. The contribution to the demagnetisation field for some macrocell p is then given in two parts, the inter-macrocell contribution given by the interaction between the atomic moments within the macrocell to the atomic moments of all other macrocells, and the intra-macrocell contribution for the atomic moments within the macrocell [49]. We can therefore write the demagnetisation field for the macrocell p in this modified bare-macrocell approach as the summation of the inter and intra macrocell contributions, [48]

$$\begin{aligned}\mathbf{B}_{\text{dip}}^{p} &= \mathbf{B}_{\text{dip}}^{q}(\text{inter}) + \mathbf{B}_{\text{dip}}^{p}(\text{intra}) \\ &= \bar{D}_{qp}^{\text{inter}} \cdot \mathbf{m}_{mc}^{q} + \bar{D}_{pp}^{\text{intra}} \cdot \mathbf{m}_{mc}^{p}\end{aligned} \tag{2.20}$$

where $\bar{D}_{qp}^{\text{inter}}$ and $\bar{D}_{pp}^{\text{intra}}$ are referred to as the effective dipole matrices [50]. These are given, respectively, by,

$$\begin{aligned}\bar{D}_{qp}^{\text{inter}} &= \frac{1}{n_p n_q} \sum_{qj=1}^{n_q} \sum_{pi=1}^{n_p} \bar{D}_{qj,pi}^{\text{inter}} \\ \bar{D}_{pp}^{\text{intra}} &= \frac{1}{n_p n_p} \sum_{pj \neq pi}^{n_p} \sum_{pi=1}^{n_p} \bar{D}_{pj,pi}^{\text{intra}}\end{aligned} \tag{2.21}$$

where, since the macrocells no longer have to be the same shape or size necessarily, the summations indices are $1 \leq p_i, p_j \leq n_p$ and $1 \leq q_j \leq n_q$, where n_p is the number of atoms in macrocell p and n_q is the number of atoms in macrocell q. Since the two effective matrices

are both describing dipole-dipole interactions, they have the same form as Equation 2.18,

$$\bar{D}^{\text{inter}}_{qj,pi} = \frac{\mu_0}{4\pi r^3_{piqj}} \begin{bmatrix} 3x^2-1 & 3xy & 3xz \\ 3yx & 3y^2-1 & 3yz \\ 3zx & 3zy & 3z^2-1 \end{bmatrix} \tag{2.22}$$

where r_{piqj} is the distance between the atomic dipole moments in macrocells p and q, and x, y, z are the Cartesian coordinates of the point qj. The intra dipole matrix is almost identical to Equation 2.22 but where qj has been replaced by pj [50].
In addition to exploiting the symmetry of the matrix to improve efficiency, the intra macrocell contribution is zero for a cubic macrocell if the magnetisation within the macrocell is uniform. It was also noted by Bowden et al. [48] that the bare macrocell approach and the inter-intra macrocell approach yield the same dipolar energy for macrocells separated by more than twelve macrocell units. We can therefore define a cutoff range, where if the interactions take place within the cutoff range the inter-intra macrocell approach is used for atomistic resolution, whereas beyond the cutoff range the inter macrocell term is replaced by the bare macrocell approach. This modified bare-macrocell approach, utilising the inter-intra macrocell approach within a cutoff range, is called the 'tensor' approach in VAMPIRE and is used for all simulations in this thesis. The obvious extension to this method, known as the hierarchical method, is to vary the resolution of the macrocells as a function of distance. With this modification, neighbouring cells are calculated atomistically, then the next neighbours are calculated using a small macrocell, then a larger macrocell for the the next neighbours, and so on, with concentrically larger macrocells as the distance increases. This method differs very little for the small size systems of this thesis, so is unused here, but is a significant improvement for larger systems, where the tensor method may become prohibitively slow [51].

2.2 Integration Techniques

The Hamiltonian discussed in section 2.1 gives us the energy of the magnetic system, but has not yet accounted for thermal fluctuations nor does it describe the time evolution of the system. In this thesis, we used two different integration methods, since we need to model both static and dynamic properties.
Static properties have been calculated using Monte Carlo methods where we use two different flavours of this technique. In chapter 3 we use the adaptive Monte Carlo method to calculate susceptibility and in chapter 5 we use the constrained Monte Carlo method in our calculation of the energy barrier. To model the dynamic behaviours in chapter 3 and chapter 4 we use the

Landau-Liftshitz-Gilbert (LLG) equation with a Heun integrator scheme and thermal effects were included via Langevin dynamics.

2.2.1 Monte Carlo Method

Monte Carlo techniques are time independent and well suited to finding the static equilibrium properties such as the temperature dependent magnetisation [52]. The Metropolis Monte Carlo algorithm is fast and efficient due to its rapid convergence to equilibrium and is outlined as followed [53, 54]. First, a random spin i is chosen and its spin direction $\mathbf{S}_i$ is changed to a random new spin direction $\mathbf{S}_i'$. This random change in the spin direction is known as the trial move and the second step is to calculate the difference in energy for this trial move ($\Delta E = E(\mathbf{S}_i') - E(\mathbf{S}_i)$). The trial move is then either accepted or rejected based on the probability

$$P = \exp\left(\frac{\Delta E}{k_B T}\right) \tag{2.23}$$

where k_B is the Boltzmann constant and T is the temperature. A probability P greater than 1 represents a reduction in the energy, ($\Delta E < 0$) so is accepted unconditionally. If the move is accepted the original spin is updated to the new spin direction, else the spin is returned to its initial state, this signals the end of the trial move. This process is then repeated until N trial moves have been attempted, where N is the total number of spins in the system. This constitutes one Monte Carlo Step.

How the trial move is chosen is important, since the Monte Carlo method must satisfy the requirement for ergodicity [2] and reversibility [3] [55]. There are three different trial moves that are used in our model, the spin flip, the Gaussian and the random trial move. The spin flip move is the same as the Ising Model, whereby the spin direction is simply reversed so

$$\mathbf{S}_i' = -\mathbf{S} \tag{2.24}$$

as shown in fig. 2.1 a). In the Gaussian move, there is a cone of acceptance around the initial spin direction and the trial move is placed randomly within this cone such that

$$\mathbf{S}_i' = \frac{\mathbf{S}_i + \sigma_g \Gamma}{|\mathbf{S}_i + \sigma_g \Gamma|} \tag{2.25}$$

where σ_g is the width of the cone and Γ is gaussian distributed random number. The Gaussian trial move is shown in fig. 2.1 b). Finally, the random trial move allows the new spin direction

[2] All states are equally accessible at equilibrium

[3] The probability of transition between two spin states is equal in both directions at equilibrium

to align in any direction in a sphere shown in fig. 2.1 c) and described by

$$\mathbf{S}_i' = \frac{\Gamma}{|\Gamma|} \tag{2.26}$$

Reversibility is satisfied with all of these, since the probability of acceptance in equation 2.23 depends only on the initial and final state. Ergodicity is not satisfied in the spin flip move individually since it does not span the whole of the phase space [30]. To solve this, Hinzke and Nowak produced an efficient Monte Carlo method that used a combination of the three trial moves, so ergodicity is then satisfied. They discovered that depending on the anisotropy and the temperature of the system, different trail moves performed better than others. For example, for a high anisotropy material, where the reversal may be domain wall nucleated, the spin flip trial move performed best. In contrast, a low anisotropy material which may reverse coherently is best modeled with a small step, where a random trial move is not efficient. At high temperatures, regardless of the anisotropy, a small step trial move is sub-optimal [56]. A further adaptation to the Hinzke-Nowak method was made by Alzate Cardona et al. [57] which ensures an acceptance rate of around 50%, which is a golden rule for efficient sampling in the Metropolis algorithm. This algorithm, known as the adaptive Monte Carlo method, is used in this thesis. It works by controlling the width of the cone, σ_g, in equation 2.25 to keep the acceptance rate around 50%. The width of the cone is recalculated at every Monte Carlo step by multiplying by some factor f which is calculated from the acceptance rate of the previous Monte Carlo step

$$f = \frac{0.5}{1-R} \tag{2.27}$$

where R is the rate of acceptance. Thus, if R was around 50% for the previous Monte Carlo step, the factor $f = 1$, so the width of the cone remains unchanged. If the acceptance rate was too high or too low, it is adjusted towards the optimum [57].

2.2.2 Constrained Monte Carlo Method

The standard Monte Carlo method outlined above is useful for a system at thermal equilibrium, where the magnetisation is still calculable. However, in this condition the magnetic anisotropy is not accessible since the magnetisation will always align with the equilibrium direction. A modification to the Monte Carlo method, first proposed by Asselin et al. [58] keeps the system in a quasi equilibrium state. This method is known as the Constrained Monte Carlo (cMC) method and acts on two spins at once, constraining the global magnetisation along any unit vector while allowing individual spins to reach thermal equilibrium. Since the system is

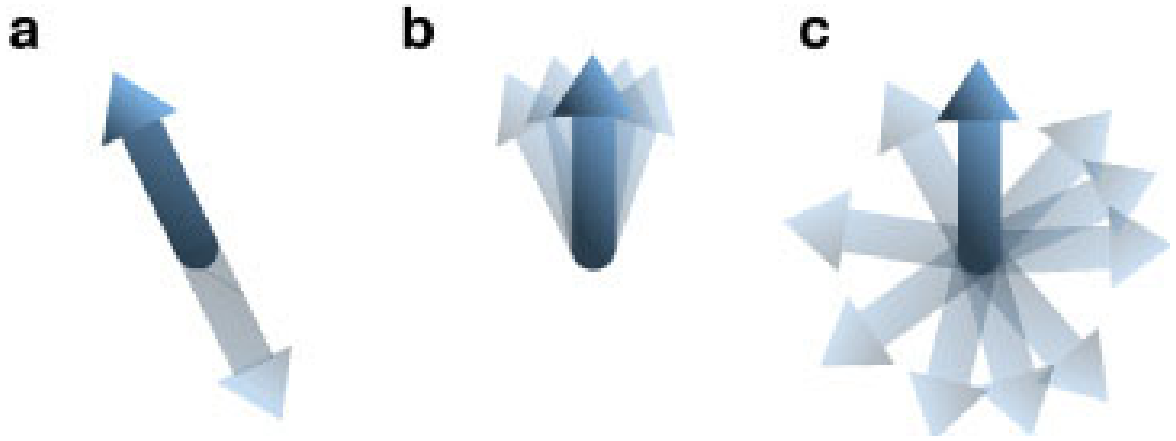

Fig. 2.1 A schematic of the three trail moves, a) Spin flip, b) Gaussian move, c) Random move. This image was taken from reference [30].

not in equilibrium, the torque acting on the magnetisation is not zero as it is in the Monte Carlo method. We take advantage of this to calculate the energy barrier separating two stable states. The method is outlined below for the global magnetisation constrained along the positive z axis.

1. Choose two spins, not necessarily neighbours, so you have a primary spin $\mathbf{S}_i$ and a compensation spin $\mathbf{S}_j$ ($i \neq j$).

2. Displace the primary spin as in the Monte Carlo method outlined in subsection 2.2.1 to produce a new spin $\mathbf{S}'_i$.

3. The compensation spin is then adjusted to preserve the magnetisation length of the x and y components such that $M_x = M_y = 0$

$$\begin{aligned} \mathbf{S}'_{jx} &= \mathbf{S}_{jx} + \mathbf{S}_{ix} - \mathbf{S}'_{ix} \\ \mathbf{S}'_{jy} &= \mathbf{S}_{jy} + \mathbf{S}_{iy} - \mathbf{S}'_{iy} \end{aligned} \tag{2.28}$$

4. Next we adjust the z component

$$\mathbf{S}'_{jz} = sign(\mathbf{S}_{jz})\sqrt{1 - \mathbf{S}'^2_{jx} - \mathbf{S}'^2_{jy}} \tag{2.29}$$

   If the content of the surd is negative ($\mathbf{S}'^2_{jx} + \mathbf{S}'^2_{jy} > 1$), the move stops and a null move is taken.

5. Calculate the new magnetisation

$$\mathbf{M}'_z = \mathbf{M}_z + \mathbf{S}'_{iz} + \mathbf{S}'_{jz} - \mathbf{S}_{iz} - \mathbf{S}_{jz} \tag{2.30}$$

   If $\mathbf{M}'_z \leq 0$ take a null move.

6. Compute the energy difference between the initial compensation spin and the final state, $\Delta E = E'_j - E_j$

7. Calculate the acceptance probability for the compensation spin

$$P = \min\Big[1, \frac{\mathbf{M}'_z}{\mathbf{M}_z}\frac{\mathbf{S}_{jz}}{\mathbf{S}'_{jz}}\exp\Big(-\frac{\Delta E}{k_B T}\Big)\Big] \tag{2.31}$$

   The acceptance probability has been modified from the standard Monte Carlo shown in equation 2.23 by a Jacobian prefactor $J = \frac{\mathbf{M}'_z}{\mathbf{M}_z}\frac{\mathbf{S}_{jz}}{\mathbf{S}'_{jz}}$ to ensure ergodicity

8. Finally, we either accept the move with probability P, or we take a null move with probability $1 - P$

The treatment of the primary spin is random since it's a regular Monte Carlo step, but the compensation spin is a deterministic treatment, so the pair of moves outlined here constitutes a single Monte Carlo step in the constrained method. The derivation of the Jacobian prefactor in step 7, along with the proof of ergodicity can be found in the appendices of the paper by Dr. P. Asselin [58]. The cMC has been used to produce results in agreement with experimental studies in papers on the temperature dependence of the anisotropy [59, 60] and calculations of the energy barriers of MRAM nanodots [61].
In chapter 5 we use the cMC method to calculate the energy barrier for PSA-MRAM towers. For this we need to find the free energy of the system, that is, the energy available to do work otherwise known as the Helmholtz free energy $\mathscr{F}$ in an isothermal system.

$$\mathscr{F} = U - TS \tag{2.32}$$

Where U is the internal energy of the system, T is the temperature and S is the entropy. At 0 Kelvin the free energy is the same as the internal energy of the system, which is the sum of the terms in the Hamiltonian outlined in section 2.1. For $T > 0$ we can not directly calculate the free energy since we can not calculate the entropy. However, we can navigate this problem with the cMC method because the torque does not vanish, and the total system torque is equivalent to the work done on the system. The magnitude of the total torque is

given by [58]

$$|\tau| = |\mathbf{S}_i \times \mathbf{B}_i| = -\frac{\partial \mathscr{F}}{\partial \theta} \tag{2.33}$$

Here, θ is the angle from the z-axis, $\mathbf{S}_i$ is spin moment and $\mathbf{B}_i$ is the net field at site i. We can therefore obtain the change in energy between two states by performing an integration between two states a and b,

$$\Delta\mathscr{F} = -\int_a^b |\tau| d\theta \tag{2.34}$$

Since $|\tau|$ is the magnitude of the total torque, we first find the sum of all individual spin torques to get the total torque ($\tau = \sum_i \tau_i = \sum_i \mathbf{S}_i \times \mathbf{B}_i$). Torque is a vector and thus has an x, y and z component, so to get the magnitude of the total torque we calculate thermodynamic average of the three components $|\tau| = |\langle\tau\rangle|$. The resulting $\Delta\mathscr{F}$ is then the effective energy barrier between two stable states, a and b, so we can then explore the angular dependence at different temperatures [61].

2.2.3 Landau-Liftshitz-Gilbert equation

While the Monte Carlo methods are appropriate for static properties, they are inappropriate to model the time evolution of dynamic properties. In 1935, Landau and Lifshitz derived their torque equation to model the macroscopic behaviours observed in early ferromagnetic resonance experiments [62]. In modern notation, the macroscopic Landau Lifshitz (LL) equation is given as

$$\frac{\partial \mathbf{m}}{\partial t} = -\gamma_e \Big[\mathbf{m} \times \mathbf{B}_{\text{eff}} + \alpha \mathbf{m} \times (\mathbf{m} \times \mathbf{B}_{\text{eff}})\Big] \tag{2.35}$$

where $\gamma_e = 1.76 \times 10^{11} \text{rad} s^{-1} T^{-1}$ is the gyro-magnetic ratio of the electron, $\mathbf{m}$ is the unit vector for the direction of the macro samples magnetisation, $\mathbf{B}_{\text{eff}}$ is the effective field on the sample, and α is the damping constant for the material. The LL equation thus describes the motion of the magnetic moments in an effective magnetic field, consisting of two terms representing two physical effects. The first term in Equation 2.35 represents the precession arising from the quantum mechanical interaction of the spin with the applied field. The second term is the relaxation of the spins towards the net field direction due to the energy dissipation. This term represents the coupling of the magnetic moments with a heat bath, causing a damped precessional motion until the spins align with the net effective field direction, where the strength of the damping is determined by α. In the LL equation, the damping is linearly related to α, which does not yield physical results with high damping materials. This was solved by Gilbert, who modified the LL equation to arrive at the Landau-Lifshitz-Gilbert

(LLG) equation [28], which for macroscopic dynamics is given by

$$\frac{\partial \mathbf{S}_i}{\partial t} = -\frac{\gamma_e}{1+\alpha^2}\Big[(\mathbf{S}_i \times \mathbf{B}_{\text{eff}}) + \alpha \mathbf{S}_i \times (\mathbf{S}_i \times \mathbf{B}_{\text{eff}})\Big] \tag{2.36}$$

where α is referred to as the Gilbert damping. The first term still represents the precession arising quantum mechanically from the interaction between the magnetisation and the effective field, but the second term describing the relaxation now relates the transfer of angular momentum from the spins to the heat bath. While the LLG equation was developed for macroscopic dynamics, it may also be used for atomistic studies, with the following important distinction [63]. In the macroscopic LLG equation in Equation 2.36, contributions to the Gilbert damping term, α, include both intrinsic (spin-lattice and spin-electron) contributions, and extrinsic (magnetostatic field, temperature and doping) contributions. This differs from the atomistic model, where only the intrinsic contributions are captured in the damping constant while the extrinsic effects are added separately (demagnetising is discussed in subsection 2.1.4 and temperature is discussed next, in subsection 2.2.4) [30, 64]. For clarity, we then replace α in Equation 2.36 with an atomistic damping term λ, as has been done in other atomistic studies using VAMPIRE. The form of the equation remains identical,

$$\frac{\partial \mathbf{S}_i}{\partial t} = -\frac{\gamma_e}{1+\lambda^2}\Big[(\mathbf{S}_i \times \mathbf{B}_{\text{eff}}) + \lambda \mathbf{S}_i \times (\mathbf{S}_i \times \mathbf{B}_{\text{eff}})\Big] \tag{2.37}$$

The Gilbert damping parameter can be obtained from experimental studies by means of ferromagnetic-resonance techniques (FMR), which can be coupled with all optical time-resolved magneto-optical Kerr effect (TRMOKE) using pump-probe technique [65, 66]. Additionally, theoretical first principle studies can provide estimates for the damping parameter [67, 68]. Finally, the effective field, $\mathbf{B}_{\text{eff}}$, in Equation 2.37 is given by the first derivative of the Hamiltonian in Equation 2.1,

$$\mathbf{B}_{\text{eff}} = -\frac{1}{\mu_s}\frac{\partial \mathscr{H}}{\partial \mathbf{S}_i} \tag{2.38}$$

where the coefficient produces a field measured in Tesla.

2.2.4 Langevin Dynamics

The LLG equation shown in Equation 2.37, with the effective field shown in Equation 2.38, is only applicable at 0 Kelvin. Thermal fluctuations are particularly important for the simulation of realistic nanoscale devices, since the anisotropy and thus stability of the system is directly affected by the finite temperature of the system. Increasing the temperature of the system

towards its Curie temperature should also demonstrate the transition from ferromagnetic to paramagnetic behaviour, as the thermal fluctuations become dominant over the exchange constant. Langevin dynamics, as developed by Brown [69], introduces a stochastic thermal field into the effective field shown in Equation 2.38 to couple the system to a heat bath. Equation 2.38 then becomes

$$\mathbf{B}_{\text{eff}} = -\frac{1}{\mu_s}\frac{\partial \mathscr{H}}{\partial \mathbf{S}_i} + \mathbf{B}_{\text{th}} \tag{2.39}$$

The added thermal field, $\mathbf{B}_{\text{th}}$, is represented as a Gaussian white noise term, where increasing the temperature of the system increases width of the Gaussian distribution, representing larger thermal fluctuations for the spins [70–72]. For this to be a valid assumption, the time-scale for fluctuations due to the thermal field has to be less than the spin motion. This assumption is satisfied throughout this thesis, as the the thermal fluctuations occur on around the femto-second timescale, while the magnetisation is closer to the pico-second. The thermal field, $\mathbf{B}_{\text{Th}}$, for each spin i for each time step is given by

$$\mathbf{B}^{i}_{\text{Th}} = \mathbf{\Gamma}(t)\sqrt{\frac{2\lambda k_B T}{\gamma \mu_s \Delta t}} \tag{2.40}$$

where $\mathbf{\Gamma}(t)$ is the three dimensional Gaussian distribution (with a mean of zero), λ is the Gilbert damping parameter, k_B is the Boltzmann constant, T is the temperature, γ is the gyro-magnetic ratio, μ_s is the magnetic spin moment, and Δt is the integration time step.

2.2.5 Heun Integration Scheme

To model the time evolution of the system, the LLG equation shown in Equation 2.37 must be solved numerically. For the majority of results in this thesis, $T \neq 0$, so the LLG equation is stochastic in nature due to the inclusion of random thermal noise (Equation 2.39). This limits the choice of solver, particularly as it must converge to the Stratonovich solution, and the magnitude of the spin must be conserved [71, 73]. While the simplest valid integration scheme is the Euler method, which assumes a linear change in the spin direction per time step. This thesis uses the Heun method, which is an improved Euler method (or a kind of second order Runge-Kutta algorithm) which benefits from a larger time-step than the Euler method due to its utilisation of a predictor-corrector algorithm. While the Heun method may use a larger time-step than the Euler method, it is limited to around femto-second step sizes due to the need to retain the precessional nature of the LLG equation, which drops to a smaller step size of $1 \times 10^{-16} s$ when the system approaches the Curie temperature [30]. Unlike the Monte Carlo methods, the Heun method can be easily parallelised for further

computational efficiency, and is the dominant integration technique for modelling the time evolution of atomistic resolution systems.
The Heun method comes in two steps, the first step, known as the predictor step, calculates a new spin position using an Euler step,

$$\mathbf{S}_i' = \left(-\frac{\gamma_e}{1+\lambda^2}\left[(\mathbf{S}_i \times \mathbf{B}_{\text{eff}}) + \lambda \mathbf{S}_i \times (\mathbf{S}_i \times \mathbf{B}_{\text{eff}})\right]\right)\Delta t \tag{2.41}$$

This step is repeated for all spins in the system (the thermal field is constant over the time-step). The second step, known as the corrector step, begins after every spin in the system has completed the predictor step, as it uses the predicted spins (with the new effective field calculated) to calculate the final spin positions.

$$\mathbf{S}_i(t+\Delta t) = \mathbf{S}_i(t) + \frac{1}{2}\left[\Delta \mathbf{S}_i(\mathbf{S}_i, t) + \Delta \mathbf{S}_i(\mathbf{S}_i', t)\right]\Delta t \tag{2.42}$$

The corrector step is also applied to all the spins in the system, which then concludes one complete integration step. This is then repeated many times to model the time progression of a dynamic system. It is important to note that these steps do not preserve the spin length, so the spin unit vector length must be re-normalized after every predictor and corrector step. Without this, it would not converge to the Stratonovich solution [30, 71].

2.2.6 Random Number Generators

Both the Monte Carlo methods and the LLG equation rely on the production of pseudo-random numbers. The Monte Carlo method uses them to produces a random trial position, and the LLG equation (for finite temperature) uses a Gaussian distribution to produce a random thermal field. The PSA-MRAM systems in this thesis consist of between $25,000 - 100,000$ atomic sites, with the majority of the simulations running for $100,000$ or more time-steps/Monte Carlo steps. Thus, the algorithm to produce a pseudo-random number for the work in this thesis needs to have a large sequence of numbers before any repeat, and produce a sufficiently uncorrelated sequence of numbers. With this in mind, VAMPIRE uses the Mersenne twister uniform random number generator, which has a period of $2^{19937} - 1$ [74], and utilises the Ziggurat method for efficient production of Gaussian distributions [75]. In VAMPIRE, the starting number in the random number sequence, known as the seed, can either be manually set to a chosen number, or if left blank will always default to the same seed. This is important, since the sequence of random numbers that follows the same seed will identical, ensuring reproducibility of the results. Changing the starting seed will subsequently produce a differing sequence of uncorrelated numbers, which can lead to a substantially

different time evolution and final result. This behaviour is utilised in all subsequent chapters, as the discrepancy in the final results with differing random number seeds is reflective of the chaotic and random nature of real thermal fluctuations. This then provides insight into the statistical behaviours of the system, which are particularly important when critiquing and testing PSA-MRAM at operational temperatures, where thermal fluctuations can impact the stability and thus validity of this design.

2.3 Modeling Spin Transfer Torque

In chapter 4 we study the switching properties for MRAM towers that are switched by spin transfer torque (STT-MRAM). We include spin transfer torque using an atomistic spin accumulation model in VAMPIRE. The STT mechanism, proposed first by Slonczewski [21] and Bergers [22] in 1996, uses an injected spin polarised current to reverse the free layer magnetisation. The STT mechanism impacts the reversal process which in turn dictates the switching properties of the system. The impact of STT on the reversal mechanism is intricately dependent on finite size and surface effects, where previous atomistic studies have focused on nanodots rather than tower structure PSA-MRAM [76, 77]. It is essential to determine the relationship between free layer size, injected current density and temperature for the long term reliability and validity of STT-PSA-MRAM. To capture thermal effects without sacrificing a continuous description, an STT model was added to the VAMPIRE software package. This work uses a spin accumulation model [78] to explore how a spin polarised current affects the behaviour of the free layer magnetisation dynamics. First, the Slonczewski approach and the spin accumulation model are described, then the calculation of spin torque via the integration of the LLG equation is outlined.

2.3.1 Slonczewski Approach

Slonczewski and Bergers were the first to outline the theoretical groundwork for STT switching in multilayer systems [21, 22]. The Slonczewski model, based on ballistic transport, modelled a trilayer consisting of two ferromagnetic layers separated by a thin non-magnetic metallic spacer. According to this model, there is a transfer of angular momentum between the conduction electrons (s electrons) and the electrons in a transition metal responsible for its local magnetisation (d electrons) via an s-d interaction. It is usual to make the assumption that the conduction electrons are s-type and neglect other interactions, since interactions such as intrinsic and side-jumping contribute significantly less to the transfer of momentum in these materials [79]. Due to this s-d interaction and the conservation of angular momentum

a torque is thus exerted on the local magnetisation and a restoring torque on the electrons [80, 81]. With this principle, Slonczewski considered the case where the first ferromagnetic layer (F_1) is pinned and the second ferromagnetic layer (F_2) is initially magnetised in the opposite direction to F_1 but is free to rotate. A current is then injected into F_1 perpendicular to the stack and the spins of the s electrons from this current will become aligned with the magnetisation direction of F_1 due to the s-d interaction. This is then a spin polarised current and will continue to flow through the non-magnetic metallic spacer until it reaches F_2. Since the magnetisation direction of F_2 is in the opposite direction to the spin polarised current, the current exerts a torque on the magnetic moments in this material due to the s-d interaction. If there is enough torque this can switch the magnetisation of F_2 and this is the core concept of STT switching [82]. There are two components to this spin transfer torque that are acting upon the magnetisation, an adiabatic and a non-adiabatic torque. The adiabatic torque is considered well understood and originates from the s electrons tending to align along the local magnetisation direction. This is a justified assumption since the magnetisation dynamics are orders of magnitude slower than that of the conduction electrons [83]. The physical interpretation of the non-adiabatic torque is still debated, but can be considered as the mis-tracking of the conduction electrons and the local magnetisation direction. The adiabatic torque is essential for the initial mechanics of a domain wall, since it causes domain wall distortion by aligning with the magnetisation direction thus transferring torque, but the adiabatic torque is responsible for the terminal velocity of the domain wall so must be included for accurate dynamics [81, 83, 84].

2.3.2 Spin Accumulation Model

The term 'spin accumulation' relates to the non-equilibrium density of spin states, a concept first suggested by Aranov [85] and experimentally verified by Johnson and Silsbee [86]. It can be described using a two-current model, one for spin-up and one for spin-down, given by $\delta m = (n^{\uparrow} - n^{\uparrow}_{eq}) - (n^{\downarrow} - n^{\downarrow}_{eq})$, where δm is the spin accumulation, n_{eq} is the equilibrium population, and $n^{\uparrow(\downarrow)}$ are the local spin densities. Zhang, Levy and Fert (ZLF) [78, 87], later developed a model, based on the drift-diffusion model, utilising the concept that a spin polarised current builds up a spin accumulation as it passes through a ferromagnet. In their model, the spin torque is described as the interaction between the local magnetisation of the ferromagnet and the spin accumulation acquired. It takes around $10^{-12}s$ for the spin current to reach a steady state at room temperature, during which, the spin current varies from layer to layer as it builds a spin accumulation. The average distance that an electron travels before flipping is known as the spin-diffusion-length, λ_{SDL}, and is proportional to the spin relaxation time [87]. A second important length scale to consider at this stage is the exchange length,

λ_J, which is normally much smaller than the spin diffusion length, and relates the transfer of angular momentum between the spin polarised electrons and the local magnetisation via an s-d interaction. These two length scales are particularly important transport properties when describing the behaviour of spin torque in a spin accumulation model. The spin accumulation can be broken down into two components; longitudinal (parallel to the local magnetisation direction) and transverse (orthogonal to the local magnetisation direction). The longitudinal component of the spin accumulation decays at the length scale of the spin-diffusion-length λ_{SDL}, while the transverse spin accumulation decays at the exchange length scale λ_J. This is definedly true by utilising a rotated basis as described in the following subsection mathematically. By intelligently choosing the rotated basis, the equation of motion for the longitudinal component of the magnetisation is independent of the exchange length λ_J. A smaller value of λ_{SDL} corresponds to a stronger correlation between the spin polarised electrons and the local magnetisation, as the longitudinal accumulation is able to respond to the magnetisation [81]. Within the range of λ_J, the transverse spin accumulation is able to interact with the local magnetisation, which can exert a torque from the spin polarised current due to the conservation of angular momentum. If the torque is large enough, this may then result in the switching of the ferromagnetic layer, on a timescale of around $10^{-9} - 10^{-10} s$, significantly slower than the time to form a steady state current due to the relaxation of the spin accumulation. The spin torque is only arising from the transverse component in this case, since the longitudinal component is parallel to the local magnetisation.

2.3.3 Calculating Torque from the Spin Accumulation

Since the behaviour of the spin accumulation occurs on a much faster time scale than the local magnetisation, it is possible to decouple the dynamics of the two. Chureemart et al. developed a self-consistent method for the calculation of the spin accumulation, which is then subsequently used to calculate the spin torque [81]. The effect of the spin torque on the local magnetisation is captured using the s-d exchange interaction relationship given by

$$\mathscr{H} = -J_{sd}\mathbf{m}\cdot\mathbf{M} \tag{2.43}$$

where J_{sd} is the s-d exchange interaction, $\mathbf{m}$ is the spin accumulation, and $\mathbf{M}$ is the local magnetisation. For this model, the equation of motion for the spin accumulation, $\mathbf{m}$, is a modified form to that of the ZLF model, with an extra term introduced by Petitjean et. al [88]. The extra term imparts additional transverse damping via a de-phasing effect, and is written in terms of the spin accumulation as $\frac{J}{\hbar}\frac{\ell_L}{\ell_\perp}\mathbf{M}\times(\mathbf{m}\times\mathbf{M})$, where ℓ_L is the Lamor spin precession length and $\ell_\perp$ is the spin coherence length. Additionally, the coefficient is

given as $\frac{J}{\hbar} = \frac{\ell_{sf}^2}{\ell_L \ell_* \tau_{sf}}$ where ℓ_* is the mean free path [89]. The equation of motion for the spin accumulation is then given by

$$\frac{d\mathbf{m}}{dt} + \frac{J_{sd}}{\hbar}\mathbf{m}\times\mathbf{M} + \frac{J}{\hbar}\frac{\ell_L}{\ell_\perp}\mathbf{M}\times(\mathbf{m}\times\mathbf{M}) = -\frac{\mathbf{m}}{\tau_{sf}} \tag{2.44}$$

where $\hbar$ is the reduced Planck constant, and τ_{sf} is the spin flip relaxation time for the conduction electrons. It is the spin-flip relaxation time, τ_{sf}, that allows the decoupling of the spin accumulation and the magnetisation, as it is much shorter than the local magnetisation time-scale. As a result, a stationary solution to $\mathbf{m}$ may now be found, which will be further simplified by separating $\mathbf{m}$ into longitudinal and transverse components. The spin current (sometimes referred to as the magnetisation current) may also be written in terms of the spin accumulation as

$$\mathbf{J}_m = \beta j_e \mathbf{M} - 2D_0\Big[\frac{\partial \mathbf{m}}{\partial x} - \beta\beta'\mathbf{M}\Big(\mathbf{M}\cdot\frac{\partial \mathbf{m}}{\partial x}\Big)\Big] \tag{2.45}$$

where β is the spin polarisation for the conductivity, β' is the spin polarisation for the diffusion, j_e is the electric current, D_0 is the diffusion constant, and x is the direction of the current flow. It is worth noting that the equations for the spin current and the electrical current differ in the works of Petitjean et. al. The spin current used in this thesis is that of the ZLF model, while only the additional damping term has been taken from Petitjean et. al. In the PSA-MRAM towers in this thesis, the current flow will be in the z direction, but as demonstrated below, it is easy to utilise a rotated basis such that the longitudinal spin accumulation and the materials magnetisation will align, so we leave Equation 2.45 as a function of x. The details of the spin parameters for the materials used in this thesis are outlined in chapter 4. Following the work of ZLF, it is beneficial to rewrite $\frac{d\mathbf{m}}{dt}$ in Equation 2.44 as $\frac{\partial \mathbf{m}}{\partial t} + \frac{\partial \mathbf{J}_m}{\partial x}$, thus

$$\frac{\partial \mathbf{m}}{\partial t} + \frac{\mathbf{J}_m}{\partial x} = -\frac{J_{sd}}{\hbar}\mathbf{m}\times\mathbf{M} - \frac{J}{\hbar}\frac{\ell_L}{\ell_\perp}\mathbf{M}\times(\mathbf{m}\times\mathbf{M}) - \frac{\mathbf{m}}{\tau_{sf}} \tag{2.46}$$

Differentiating Equation 2.45 with respect to x and subbing into Equation 2.46 produces

$$\frac{\partial \mathbf{m}}{\partial t} = 2D_0\Big[\frac{\partial^2 \mathbf{m}}{\partial x^2} - \beta\beta'\mathbf{M}\Big(\mathbf{M}\cdot\frac{\partial^2 \mathbf{m}}{\partial x^2}\Big)\Big] - \frac{J_{sd}}{\hbar}\mathbf{m}\times\mathbf{M} - \frac{J}{\hbar}\frac{\ell_L}{\ell_\perp}\mathbf{M}\times(\mathbf{m}\times\mathbf{M}) - \frac{\mathbf{m}}{\tau_{sf}} \tag{2.47}$$

By rearranging and collecting terms in Equation 2.47, a neater form is found as

$$\frac{1}{2D_0}\frac{\partial \mathbf{m}}{\partial t} = \frac{\partial^2 \mathbf{m}}{\partial x^2} - \beta\beta'\mathbf{M}\Big(\mathbf{M}\cdot\frac{\partial^2 \mathbf{m}}{\partial x^2}\Big) - \frac{\mathbf{m}}{\lambda_{sf}^2} - \frac{\mathbf{m}\times\mathbf{M}}{\lambda_j^2} - \frac{\mathbf{M}(\mathbf{m}\times\mathbf{M})}{\lambda_\phi^2} \tag{2.48}$$

where $\lambda_{sf} = \sqrt{2D_0\tau_{sf}}$ is the spin flip length, $\lambda_j = \sqrt{\frac{2\hbar D_0}{J_{sd}}}$ is the spin precession length, and $\lambda_\phi = \sqrt{2\hbar D_0 \frac{\ell_\perp}{J\ell_L}}$ is the spin dephasing length. It is seen in the work of Chureemart [89] that the spin dephasing length and the spin flip length may be combined into a single length scale, $\lambda_{SF}^{-2} = \lambda_{sf}^{-2} + \lambda_\phi^{-2}$, where the resulting merged term is the spin flip length accounting for the damping from the Bloch-like term of the ZLF model [78] and the transverse damping from Petitjean et. al [88]. From this point on in the thesis, λ_{SF} refers to this merged spin flip, to be consistent with literature published using STT, where the initial derivation from Equations 2.44 to 2.48 are normally emitted.

Since the local magnetisation can align in any direction, the solutions to Equation 2.48 should be in a rotated basis $\mathbf{b}_1$, $\mathbf{b}_2$ and $\mathbf{b}_3$. The purpose of this is to ensure the longitudinal component of the local magnetisation will align along $\mathbf{b}_1$, while $\mathbf{b}_2$ and $\mathbf{b}_3$ will align along the transverse plane of the local magnetisation. Thus, the spin accumulation is split into two transverse and one longitudinal component when finding a solution. The solutions to the spin accumulation in the rotated basis is then given by

$$\begin{aligned}
\mathbf{m}_\parallel &= \Big[\mathbf{m}_\parallel(\infty) + \Big[\mathbf{m}_\parallel(0) - \mathbf{m}_\parallel(\infty)\Big] e^{-x/\lambda_{sdl}}\Big]\hat{\mathbf{b}}_1, \\
\mathbf{m}_{\perp,2} &= 2e^{-k_1 x}\Big[u\cos(k_2 x) - v\sin(k_2 x)\Big]\hat{\mathbf{b}}_2, \\
\mathbf{m}_{\perp,3} &= 2e^{-k_1 x}\Big[u\sin(k_2 x) + v\cos(k_2 x)\Big]\hat{\mathbf{b}}_3
\end{aligned} \tag{2.49}$$

where $(k_1 \pm ik_2) = \sqrt{\lambda_{SF}^{-2} \pm i\lambda_j^{-2}}$, λ_{sdl} is the spin diffusion length and $\mathbf{m}_\parallel(\infty)$ is the equilibrium spin accumulation. The other constants, u, v and $\mathbf{m}_\parallel(0)$ are determined from the boundary condition of the continuity of the spin current $\mathbf{j}_m$, outlined in subsection 2.3.4. Once the transverse and longitudinal spin accumulation has been determined, the STT effect is introduced via Equation 2.43. In the rotated basis, the longitudinal spin accumulation $\mathbf{m}_\parallel$ is parallel to the local magnetisation and thus gives rise to zero torque. As a result, only the transverse components of the spin accumulation, $\mathbf{m}_{\perp,2}$ and $\mathbf{m}_{\perp,3}$, will contribute to the spin torque. The first two terms in Equation 2.43, $J_{sd}\mathbf{m}$, describe a magnetic field due to the s-d interaction arising from the spin accumulation, which is now written as $J_{sd}\mathbf{m}_\perp$ since it is only the transverse components. This field can be split into an adiabatic and non-adiabatic term, as shown in the works of ZLF [78], as

$$J_{sd}\mathbf{m}_\perp = a(\mathbf{M}\times\mathbf{M}_p) + b(\mathbf{M}\times\mathbf{M}_p)\times\mathbf{M} \tag{2.50}$$

where a and b are the adiabatic and non-adiabatic torque parameters respectively, and the field is a function of the magnetisation of the current layer $\mathbf{M}$, and the magnetisation of the

previous layer $\mathbf{M}_p$. The spin torque is then given by

$$\mathbf{ST} = a[\mathbf{M} \times (\mathbf{M} \times \mathbf{M}_p)] + b[\mathbf{M} \times \mathbf{M}_p] \tag{2.51}$$

where the first term is the adiabatic spin torque (AST) and the second is the non-adiabatic spin torque (NAST). The AST term can be compared to the "spin torque" introduced by Slonczewski in his seminal paper [21], while the NAST term is interpreted as a field-like term [78, 89]. In this model, the adiabatic and non-adiabatic torque parameters, a and b respectively, are given by

$$\begin{aligned} a &= \frac{J_{sd}\mathbf{b}_1 \cdot (\mathbf{m}_\perp \times \mathbf{M}_{\perp p})}{|\mathbf{M}_{\perp p}|^2} = \frac{J_{sd}|\mathbf{m}_\perp| \sin\theta}{|\mathbf{M}_{\perp p}|}, \\ b &= \frac{J_{sd}(\mathbf{m}_\perp \cdot \mathbf{M}_{\perp p})}{|\mathbf{M}_{\perp p}|^2} = \frac{J_{sd}|\mathbf{m}_\perp| \cos\theta}{|\mathbf{M}_{\perp p}|} \end{aligned} \tag{2.52}$$

where $\mathbf{M}_{\perp p}$ is the transverse magnetisation of the previous layer in consistent notation with previous equations, and θ is the angle between the current layer and the previous layer. This model then allows spatially varying spin torque, since the AST and NAST are not spatially constant, as they are in some models. Here, the AST and NAST are also calculated from the spin accumulation, rather than relying on phenomenological constants. This is critical to the study of STT-PSA-MRAM in chapter 4, whereby long range interaction (responsible for the shape anisotropy) and finite temperatures (significant thermal fluctuations) both contribute to spatially varying magnetisation.

Summarising the model, this approach allows the spin accumulation and spin current to be calculated at every point in the systems lattice if a macro-cell of mono-layer thickness is chosen, as it is in this thesis. The spin current entering a layer i from layer $i-1$ is required, so the starting spin current for the first layer is manually set. Additionally, the spin parameters β, β', λ_{sdl}, D_0, J_{sd} and $\mathbf{m}_{\|}(\infty)$ must be found for the materials simulated. The details of the spin parameters are outlined in chapter 4, as this is where they are used. The longitudinal and transverse spin accumulation is then calculated for the layer i, after calculating u, v and $\mathbf{m}_{\|}(0)$ as outlined in subsection 2.3.4. The spin current, $\mathbf{J}_m$, at a distance of $x = t_F$ (corresponding the thickness of one atomic layer for this thesis) is calculated using Equation 2.45 and is thus the spin current of the layer $i+1$. Once the spin accumulation (and spin current) for the whole system has been calculated, STT is calculated from Equation 2.43.

2.3.4 Determining Spin Accumulation Coefficients

Separating the spin accumulation into three components, as shown in Equation 2.49, presents three unknown variables, u, v and $\mathbf{m}_{\parallel}(0)$. The purpose of this section is to outline the process utilised to determine the unknown variables, which follows the derivation in the appendix of the works of Chureemart et. al [89]. The derivation starts with the spin current, found in Equation 2.45, for any arbitrary direction of the magnetisation, $\mathbf{M} = M_x\mathbf{e}_x + M_y\mathbf{e}_y + M_z\mathbf{e}_z$, expanded in terms of the global spatial components.

$$\begin{aligned}
J_{mx}(x) &= \beta j_e M_x - 2D_0\Big[\frac{\partial m_x}{\partial x} - \beta\beta' M_x\Big(M_x\frac{\partial m_x}{\partial x} + M_y\frac{\partial m_y}{\partial x} + M_z\frac{\partial m_z}{\partial x}\Big)\Big] \\
J_{my}(x) &= \beta j_e M_y - 2D_0\Big[\frac{\partial m_y}{\partial x} - \beta\beta' M_y\Big(M_x\frac{\partial m_x}{\partial x} + M_y\frac{\partial m_y}{\partial x} + M_z\frac{\partial m_z}{\partial x}\Big)\Big] \\
J_{mz}(x) &= \beta j_e M_z - 2D_0\Big[\frac{\partial m_z}{\partial x} - \beta\beta' M_z\Big(M_x\frac{\partial m_x}{\partial x} + M_y\frac{\partial m_y}{\partial x} + M_z\frac{\partial m_z}{\partial x}\Big)\Big]
\end{aligned} \tag{2.53}$$

Since, in this thesis, STT is modelled layer resolved, i.e. calculating the spin current and the spin accumulation layer by layer, Equation 2.53 can be rewritten between layers $(x = 0)$ as

$$\begin{aligned}
j_{mx}(0) - \beta j_e M_x &= 2D_0\Big(\beta\beta' M_x^2 - 1\Big)\frac{\partial m_x(0)}{\partial x} + 2D_0\beta\beta' M_x M_y \times \frac{\partial m_y(0)}{\partial x} \\
&\quad + 2D_0\beta\beta' M_x M_z\frac{\partial m_z(0)}{\partial x} \\
j_{my}(0) - \beta j_e M_y &= 2D_0\beta\beta' M_x M_y\frac{\partial m_x(0)}{\partial x} + 2D_0\Big(\beta\beta' M_y^2 - 1\Big) \times \frac{\partial m_y(0)}{\partial x} \\
&\quad + 2D_0\beta\beta' M_y M_z\frac{\partial m_z(0)}{\partial x} \\
j_{mz}(0) - \beta j_e M_z &= 2D_0\beta\beta' M_x M_z\frac{\partial m_x(0)}{\partial x} + 2D_0\beta\beta' M_y M_z \times \frac{\partial m_y(0)}{\partial x} \\
&\quad + 2D_0\Big(\beta\beta' M_z^2 - 1\Big)\frac{\partial m_z(0)}{\partial x}
\end{aligned} \tag{2.54}$$

This can then be rearranged and re-written in matrix form below, which is how it is calculated in VAMPIRE.

$$\begin{bmatrix} \frac{\partial \mathbf{m}_x(0)}{\partial x} \\ \frac{\partial \mathbf{m}_y(0)}{\partial x} \\ \frac{\partial \mathbf{m}_z(0)}{\partial x} \end{bmatrix} = [V]^{-1}\begin{bmatrix} J_{mx}(0) - \beta j_e\mathbf{M}_x \\ J_{my}(0) - \beta j_e\mathbf{M}_y \\ J_{mz}(0) - \beta j_e\mathbf{M}_z \end{bmatrix} \tag{2.55}$$

where

$$[V] = \begin{bmatrix} 2D_0(\beta\beta'\mathbf{M}_x^2 - 1) & 2D_0\beta\beta'\mathbf{M}_x\mathbf{M}_y & 2D_0\beta\beta'\mathbf{M}_x\mathbf{M}_z \\ 2D_0\beta\beta'\mathbf{M}_y\mathbf{M}_x & 2D_0(\beta\beta'\mathbf{M}_y^2 - 1) & 2D_0\beta\beta'\mathbf{M}_y\mathbf{M}_z \\ 2D_0\beta\beta'\mathbf{M}_z\mathbf{M}_x & 2D_0\beta\beta'\mathbf{M}_z\mathbf{M}_y & 2D_0(\beta\beta'\mathbf{M}_z^2 - 1) \end{bmatrix} \tag{2.56}$$

From Equation 2.55, the first derivative of the spin accumulation can be calculated from the spin current from the previous layer, along with some material parameters β, β' and D_0. This is why the initial spin current must be set by the user, without it, the first derivative of the spin accumulation is not calculated in this model and the rest of this derivation stops. For all subsequent layers, the spin current will be recalculated using Equation 2.45.
The second half of the derivation follows virtually the same steps as the first half, but for the spin accumulation now in place of the spin current. To determine the unknown constants from the first derivative of the spin accumulation, the derivation first writes the spin accumulation in its global spatial components, much like the first step with the spin current. This time, ensuring it is written with the rotated basis, the spin accumulation is written as

$$\begin{aligned} m_x(x) &= b_{1,x}m_{\parallel}(x) + b_{2,x}m_{\perp,2}(x) + b_{3,x}m_{\perp,3}(x) \\ m_y(x) &= b_{1,y}m_{\parallel}(x) + b_{2,y}m_{\perp,2}(x) + b_{3,y}m_{\perp,3}(x) \\ m_z(x) &= b_{1,z}m_{\parallel}(x) + b_{2,z}m_{\perp,2}(x) + b_{3,z}m_{\perp,3}(x) \end{aligned} \tag{2.57}$$

where the derivative of each component of the spin accumulation immediately follows as

$$\begin{aligned} \frac{\partial m_x(x)}{\partial x} &= b_{1,x}\frac{\partial m_{\parallel}(x)}{\partial x} + b_{2,x}\frac{\partial m_{\perp,2}(x)}{\partial x} + b_{3,x}\frac{\partial m_{\perp,3}(x)}{\partial x} \\ \frac{\partial m_y(x)}{\partial x} &= b_{1,y}\frac{\partial m_{\parallel}(x)}{\partial x} + b_{2,y}\frac{\partial m_{\perp,2}(x)}{\partial x} + b_{3,y}\frac{\partial m_{\perp,3}(x)}{\partial x} \\ \frac{\partial m_z(x)}{\partial x} &= b_{1,z}\frac{\partial m_{\parallel}(x)}{\partial x} + b_{2,z}\frac{\partial m_{\perp,2}(x)}{\partial x} + b_{3,z}\frac{\partial m_{\perp,3}(x)}{\partial x} \end{aligned} \tag{2.58}$$

Just like with the spin current, Equation 2.58 can be rewritten between layers $(x = 0)$ as

$$\begin{aligned} \frac{\partial m_{\parallel}(0)}{\partial x} &= \frac{-m_{\parallel}(0)}{\lambda_{sdl}} \\ \frac{\partial m_{\perp,2}(0)}{\partial x} &= -2k_1u - 2k_2v \\ \frac{\partial m_{\perp,3}(0)}{\partial x} &= 2k_2u - 2k_1v \end{aligned} \tag{2.59}$$

Once again, this can be re-written in matrix form by substituting Equation 2.59 into Equation 2.58. These matrices are then used in VAMPIRE, and are given by

$$\begin{bmatrix} \frac{\partial \mathbf{m}_x(0)}{\partial x} \\ \frac{\partial \mathbf{m}_y(0)}{\partial x} \\ \frac{\partial \mathbf{m}_z(0)}{\partial x} \end{bmatrix} = [T] \begin{bmatrix} \mathbf{m}_{\parallel}(0) \\ u \\ v \end{bmatrix} \tag{2.60}$$

where

$$[T] = \begin{bmatrix} \frac{b_{1x}}{\lambda_{sdl}} & (-2b_{2x}k_1 + 2b_{3x}k_2) & (-2b_{2x}k_2 - 2b_{3x}k_1) \\ \frac{b_{1y}}{\lambda_{sdl}} & (-2b_{2y}k_1 + 2b_{3y}k_2) & (-2b_{2y}k_2 - 2b_{3y}k_1) \\ \frac{b_{1z}}{} & (-2b_{2z}k_1 + 2b_{3z}k_2) & (-2b_{2z}k_2 - 2b_{3z}k_1)\lambda_{sdl} \end{bmatrix} \tag{2.61}$$

In Equation 2.60, the partial derivatives of the spin accumulation have been determined in Equation 2.55, and all components of matrix $[T]$ are known from the spin accumulation. This allows the unknown constants, u, v and $\mathbf{m}_{\parallel}(0)$ to be determined, thus completing the calculation of the longitudinal and transverse spin accumulation in Equation 2.49.

2.3.5 The Modified Simmons' Equation

The method outlined in the previous subsections describes how a current is modelled moving through magnetic materials. However, the MgO layer that separates the reference layer and the free layer is non-magnetic and is not explicitly included in the simulations. Clearly, the current must progress across the MgO layer to reach the free layer, which will impede the flow, reducing the torque on the free layer. It is essential to capture the effects of the MTJ as a key part of the physics. Since the interactions with the atomic sites are not explicitly calculated in non-magnetic materials, a simplified approach is taken for the tunneling current based on a modified Simmons' equation. The form of the modified Simmons' equation is given by

$$j_{tun} = J_0[J^{\uparrow} + J^{\downarrow}] \tag{2.62}$$

where J_0 is the tunneling current found in the original Simmons' equation and $J^{\uparrow(\downarrow)}$ are the spin up (down) current densities [90, 49]. In the Simmons' equation, the tunneling current is described in terms of several components not calculated thus far, such as the electric potential and the Fermi energy. However, a simpler form that captures the drop in torque as a function of MgO thickness is derived from a fitting of the tunneling current. The tunneling current that enters the free layer is calculated from this simplified form as

$$j_{tun} = j_e \frac{1}{2}[(1+\cos(\theta)) + \frac{1}{2}(1-\cos(\theta))]e^{\frac{t}{0.25\times10^{-9}}} \tag{2.63}$$

where j_e is the current that enters the MgO layer, t is the thickness of the MgO layer and θ is the relative angle between the reference layer and the free layer [91, 49]. Particularly important is the denominator within the exponential term, which contains the value 0.25×10^{-9}. This is a bespoke solution for an MgO layer of 1 nm thickness that was found via the fitting of the tunneling current by Chureemart following the work of this reference [89]. This is applicable to the tower structures studied in this thesis, but would need a more complicated

term for other MgO thickness in the future. The thickness of the MgO layer significantly influences the spin torque transformed across the barrier.

2.4 Parameterisation for an MRAM Tower

All subsequent chapters are the results of simulating a CoFeB/MgO magnetic tunnel junction, with a CoPt synthetic antiferromagnet to provide stability to the reference layer. This section outlines the main parameters used in all subsequent chapters to model these materials. Specifically, this includes the exchange constant, anisotropy, damping and atomic spin moment for these materials, as well as a generic tower structure. The STT parameters are used only in chapter 4, so those are detailed there rather than in this subsection. Additionally, in chapter 5, certain layers are constrained, so the differing details of those tower structures are described there. In this section, the properties of a CoFeB/MgO MTJ are outlined, followed by the supporting CoPt SAF. Finally, the central parameters and their sources are described.

2.4.1 The Properties of a CoFeB/MgO MTJ

For a reliable STT-MRAM device, the MTJ must simultaneously demonstrate a high tunnel magnetoresistance (TMR), a high thermal stability factor (Δ), and a low switching current [92–94]. Due to these requirements, this thesis uses a CoFeB/MgO MTJ, since this combination of materials is the most promising known choice. This subsection discusses how the CoFeB/MgO material properties fit the requirements for commercial STT-MRAM.

The high TMR is achieved due to the non-magnetic MgO spacer layer, which when compared to the previously conventional aluminium oxide (Al-O) of the late 90s - early 2000s, demonstrates significantly improved giant magnetoresistance [18, 17]. This is due to the Al-Os amorphous nature (thus no crystallographic symmetry), which causes multiple Bloch states in the first CoFeB layer to couple with the evanescent states [4] in the Al-O. This form of tunneling is described as incoherent tunneling, and results in a significantly reduced current entering the second CoFeB layer after tunneling, with a magnetoresistance ratio of less than 100% [95–97]. In contrast, growing an MgO layer on an amorphous CoFeB layer (assuming the MgO layer is more than four monoatomic layers thick), then annealing, will crystallise the MgO with a (001) texture. This also extends to the CoFeB layer, which crystallises to a bcc lattice with a (001) texture, using the MgO like a template [98]. In this case, the symmetry of the wave function is conserved during tunneling, described as coherent tunneling, which

[4] Quantum states that decay rapidly away from a boundary

results in magnetoresistance ratios up five times greater than that of Al-O [99, 95, 97].
The thermal stability factor, $\Delta = \frac{E_b}{k_B T}$, where E_b is the energy barrier separating the two stable magnetic states, is directly related to the total anisotropy of the system. The total anisotropy can be given as the contribution from the bulk of the material k_b, the contribution from the interfacial layer k_i and the contribution from the shape anisotropy $k_s = \frac{\mu_0 M_s^2}{2}$ as

$$k_{tot} = k_b + \frac{k_i}{t} + k_s \tag{2.64}$$

where t is the thickness. The bulk anisotropy, k_b, is negligible in CoFeB [100]. The interfacial anisotropy, k_i, arises from the hybridisation of the iron 3d orbital and oxygen 2p orbital at the CoFeB-Mgo interface [101, 100]. Initially, studies in MRAM involved in-plane structures (disc-like shapes) whereby the interfacial component becomes dominant if the free layer thickness is reduced to around $t_f < 1.5$ nm, as it acts perpendicular to the easy-axis for in-plane structures. By adding a second MgO layer, further interfacial anisotropy can be added to the system, which allowed the initial scaling of MTJs to around 20 nm, demonstrating the benefits of the CoFeB/MgO material choice. The third term in Equation 2.64 is the shape anisotropy, where the positive coefficient here is significant. For the in-plane MRAM, where the interfacial anisotropy can be dominant, the shape anisotropy would be negative in Equation 2.64, meaning it would oppose the interfacial direction. This is the reason those structures can't be scaled below around 20 nm, as the sources of anisotropy compete in perpendicular directions and the thermal stability drops below the industrial requirement. In this thesis, elongated tower structures are studied, inducing perpendicular shape anisotropy (PSA), so the shape anisotropy and the interfacial anisotropy are aligned. If the easy-axis is then also along the perpendicular direction, the free layer will have a boost in thermal stability [93].
The requirement of a low (and fast) switching current also makes the CoFeB/MgO combination appealing, though a low switching current and a high thermal stability will always be a compromise. A materials Gilbert damping parameter dictates the speed of the dynamic behaviour, since, as described in the description of Equation 2.37, it describes the dissipation of the atomic spins energy to a heat bath. In a CoFeB/MgO structure, the hybridisation of the Fe orbitals at the interface that causes the interfacial anisotropy also causes an increase in the Gilbert damping. The bulk of the CoFeB, however, has a lower damping, since the spin and lattice contributions towards damping are weak, and the interfacial anisotropy is not far reaching in a vertically elongated free layer [64]. This makes CoFeB a strong material candidate, since a lower damping results in greater stability (less fluctuations and energy loss). Additionally, low damping is best for STT [82], which is likely to drive the reversal

mechanism.
The unique properties of CoFeB/MgO MTJs is the closest known material choice to solve the trilemma of a high thermal stability, a high TMR, and a low writing current. Since the high thermal stability and the low writing current are tradeoffs, finding the right compromise is crucial for reliable and effective PSA-STT-MRAM.

2.4.2 The CoPt SAF

To achieve a switchable free layer with a fixed reference layer, the reference layer must have greater stability than the free layer. Consider first a simplified MTJ consisting of only a reference layer, MgO tunneling layer and a free layer. Increased reference layer stability is partially achieved by having a relatively thin reference layer (sub 1.3 nm thick). In this case, the stability of the reference layer is entirely due to the MgO induced interfacial anisotropy in the nearby CoFeB atoms. However, this alone is not sufficient to ensure stability of the reference layer at operational temperatures. Additionally, in this simple MTJ design, the free layer will experience a stray field emanating from the reference layer and vice versa. This will cause an anti-symmetry in the coercive field required to switch the free layer. The stray field from the reference layer will produce a preference for the free layer to become aligned. When in the anti-aligned state, the stray field from the free layer on the reference layer could cause a loss of stability, rendering the device useless of reading/writing if destabilised sufficiently [102].
Practically, the need for a stable reference layer is satisfied by creating a synthetic anti-ferromagnet (SAF) structure. The simplest method, would be to add a stable pinned layer below the reference layer, coupling these layers antiferromagnetically. The coupling is achieved by using a non-magnetic metallic Ir or Ru spacer layer, which mediates the Ruderman–Kittel–Kasuya–Yosida (RKKY) exchange (sometimes called the indirect exchange). The exchange coupling on either side of the Ir (or Ru) layer forces a preferred magnetic moment in the conduction electrons of the spacer layer. Depending on the thickness of the spacer layer, this can perpetuate an antiferromagnetic coupling between the two layers separated by Ir. By tuning the thickness of the pinned layer, the stray field from the reference layer can be reduced to a negligible magnitude [103–105]. However, since the reference layer is very thin, the pinned layer in this basic design is also very thin, and requires prohibitively high (atomistic) precision to manufacture. This simple addition of a thin pinned layer is therefore impractical. A more reasonable method, is to enlarge the reference and pinned layer from this simple design, and couple that anti-ferromagnetically to a third layer. Typically, the enlarged reference and pinned layer are then made of CoPt, rather than CoFeB, since the enhanced anisotropy stabilising CoFeB is only significant for 1.3 nm thick layers. The

third layer is then a material with a high anisotropy and exchange, such as IrMn or PtMn. By tuning the thickness of these two additional layers, it is possible to provide stability to the reference layer, while minimising the stray field to the free layer. The increased thickness of these two additional layers is much more reasonable to create experimentally [45].
In this thesis, the impact of the SAF is important, but a simplification can be made to model the structure outlined above, since the precise dynamic behaviours of these layers are unimportant. This is necessary as VAMPIRE does not capture the RKKY exchange, and is able to deal with antiferromagnetic coupling naturally via the exchange constant between the materials. For $J_{ij} > 0$ the spins i and j are ferromagnetic, while if $J_{ij} < 0$, the spins i and j are antiferromagnetic. The overall purpose of the SAF is to provide a stray field that provides additional stability to the reference layer, while having minimal impact on the free layer. If the SAF satisfies these requirements, the impact of the SAF has been captured. In this thesis, the reference layer is 1 nm of CoFeB, which is anti-ferromagnetically coupled to CoPt, which is anti-ferromagnetically coupled to more CoPt. The first layer of CoPt is relatively thin, and on its own would cancel out the stray field from the reference layer on the free layer. The second CoPt layer is thicker than the first, and is tuned to provide the unconditional stability to the reference layer without producing a significant stray field into the free layer. The details of the CoPt and CoFeB material parameters are outlined in the next section, along with the dimensions of a standard MRAM tower.

2.4.3 The Parameters

The atomistic structure of the CoFeB/MgO MTJ with a CoPt SAF is demonstrated in Figure 2.2, where the tower is built along the z-direction, thus the easy axis is along the z-direction. For this model, the tower structure is an idealised case, where all the interfacial perpendicular anisotropy discussed in subsection 2.4.1 is provided by a single enhanced monolayer in contact with the MgO. These two monolayers (one for the reference layer and one for the free layer) have a larger value for the uniaxial anisotropy, exchange constant and Gilbert damping. The bulk of the reference layer and free layer have a reduced exchange constant, a very small Gilbert damping, and zero uniaxial anistropy. A second simplification of this model, is that each atomic site of the CoFeB material is treated as an averaged magnetic moment, rather than individually treated them as Co, Fe and B. This simplification is also used for CoPt, rather than treating the Co and the Pt individually. The two CoPt layers shown in Figure 2.2 are parameterised identically, with the only difference being the magnetisation direction they are initialised along. The top CoPt layer is along the positive z-axis, aligning with the reference layer, while the bottom CoPt layer is aligned along the negative z-axis. They are thus anti-ferromagnetically coupled. Throughout this thesis, the

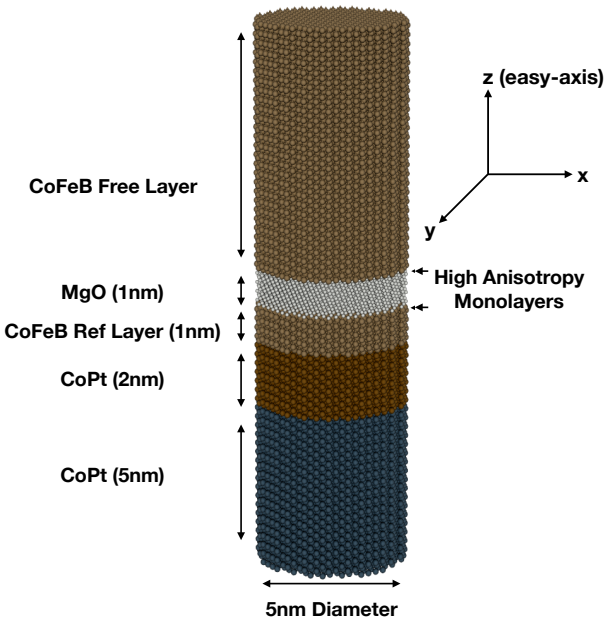

Fig. 2.2 A schematic of the general PSA-MRAM tower structure being studied in this thesis. It consists of two anti-ferromagnetically coupled CoPt layers, followed by the MTJ, with two enhanced high anisotropy CoFeB mono-layers on either side of the MgO barrier. The reference layer is 1 nm and the free layer is studied with a thickness of 8 nm, 18 nm, 28 nm, 38 nm and 48 nm. Finally, the easy axis for our structure is along the positive z-direction.

tower is modelled as a bcc structure with an atomic spacing of 0.2866 nm. The tower has a diameter of 5 nm, and only the free layer changes in thickness, while the other layers remain identical throughout. Such a small diameter is required for computational efficiency, allowing growing free layer thicknesses to be explored within realistic computation time. The total thickness of the reference layer is 1 nm including the enhanced monolayer, and similarly the thickness of the free layer whenever given in this thesis will include the enhanced monolayer. The non-magnetic MgO barrier is not included explicitly in the simulation, but the impact of its presence is captured using the enhanced monolayers.
The exchange energy constant is calculated from the mean-field approximation

$$J_{ij} = \frac{3k_B T_C}{\varepsilon z} \tag{2.65}$$

where k_B is the Boltzmann constant, T_C is the Curie temperature for the material, z is the number of nearest neighbours and ε is the correction factor due to spin wave excitation's ($\varepsilon = 0.766$ for bcc structures) [106, 30]. The Curie temperature for thin-film CoFeB was obtained by Sato et. al, though in this model the exchange constant for CoFeB is calculated

twice, for the monolayer and the bulk [107]. For the bulk of the free layer and reference layer, the number of nearest neighbours $z = 8$, while for the monolayers $z = 4$ due to reduced coordination. The Curie temperature for CoPt is taken from Crisan et. al's investigation into CoPt, while the values of $z = 8$ and $\varepsilon = 0.766$ are used as it is still treated as a bcc lattice [108].

The atomistic anistropy constant is derived from the macroscropic anisotropy energy density via the equation

$$k_u = \frac{K_u a^3}{n} \tag{2.66}$$

where K_u is the macroscopic anisotropy energy density in Jm^{-3}, a is the lattice spacing, and n is the number of atoms in a unit cell ($n = 2$ for a bcc lattice) [30]. The anisotropy of bulk CoFeB is known to be negligibly small, so is approximated to zero in this study [100]. The enhanced anisotropy at the CoFeB monolayers is calculated using Equation 2.66, following the experimental measurements of the temperature dependence for the macroscopic anisotropy energy density from Sato et. al [107]. Similarly the energy density for the CoPt layers are found at near room temperature in the works of McCurrie et. al, then the uniaxial anisotropy is found using the lattice spacing and the number of neighbours in a bcc lattice [109].

The atomic moment used for the CoFeB in this thesis is different for the reference layer and the free layer, due to to the significantly different nominal thicknesses. The relationship to calculate the atomic moment is the same form as that of anisotropy in Equation 2.66, only related to the saturation magnetisation.

$$\mu_s = \frac{M_s a^3}{n} \tag{2.67}$$

For the reference layer (RL), an atomic moment of $\mu_s = 1.6\mu_B$ is used, corresponding to an $M_s \approx 1.3 MAm^{-1}$ found by Ikeda et. al [100]. This value of the atomic moment has typically been used for both the free layer and the reference layer in previous studies of CoFeB MTJs [82, 107, 61, 77, 49, 110]. However, the M_s measured is significantly less than that found experimentally or via ab-initio for bulk CoFeB [111–113]. The free layer (FL) for this thesis therefore has a larger atomic moment of $\mu_s = 2.5\mu_B$, corresponding to a larger saturation magnetisation found in bulk CoFeB, $M_s \approx 2 MAm^{-1}$. The atomic moment of the two CoPt layers can also be calculated using Equation 2.67, with $M_s \approx 0.7 MAm^{-1}$ [114], the atomic moment would be $\mu_s \approx 0.9$. Since the CoPt is only in place to provide for stability for the reference layer, the atomic moment in this thesis is just rounded to $\mu_s = 1$ for the CoPt layers.

Finally, the Gilbert damping term is a vital inclusion as it has been shown that the Gilbert

damping has a thickness dependence in CoFeB/MgO MTJs [92]. The monolayer has an enhanced Gilbert damping, due to hybridisation of the orbitals at the boundary between CoFeB and MgO, found to be $\alpha = 0.11$. The bulk of the CoFeB has a lower Gilbert damping, $\alpha = 0.001$, due to the weak spin-orbit coupling that motivates this material choice (see subsection 2.4.1) [115, 64]. The CoPt Gilbert damping is left at $\alpha = 1$ for this thesis, which corresponds to a rapid relaxation. Similar to the atomic moment, the motivation for simplifying CoPt is due to its use as a stabiliser to the reference layer, rather than a material that will be explored in this thesis.
These central parameters are found in Table 2.1, where the additional parameters required for STT are found in chapter 4, and the additional layers that are constrained in the calculation of the energy barrier are described in chapter 5.

	Bulk	Interface	CoPt
J_{ij} (J/link)	7.735×10^{-21}	1.547×10^{-20}	4.88×10^{-21}
k_u (J/atom)	0	1.35×10^{-22}	3.33×10^{-23}
μ_s (J/T)	$1.6^{(RL)}, 2.5^{(FL)}$	$1.6^{(RL)}, 2.5^{FL}$	1.0
α	0.001	0.11	1.0

Table 2.1 Here we see the key parameters for modeling CoFeB/MgO MTJs with a CoPt SAF. These parameters are essential for the Hamiltonian/LLG equation, so are the same for all subsequent chapters of this thesis.

2.5 Summary

This chapter has introduced the key equations, which describe the atomistic model used throughout the subsequent chapters. The Hamiltonian for the exchange energy, anisotropy, external field and dipole interaction were all outlined. The two flavours of the Monte Carlo method and the LLG equation were then described as central integration techniques used throughout this thesis. There are several approaches to modelling spin transfer torque, so the calculation of the spin torque from the spin accumulation, introducing the key parameters for the methodology, was introduced. The details of these parameters are found in chapter 4. Finally, the parameters for the spin model that are used in all subsequent chapters to model CoFeB and CoPt were outlined.

3

Thermodynamic Properties and Switching Mechanisms of PSA-MRAM

The properties and behaviours of nanoscale ferromagnetic materials are strongly size, shape and temperature dependent. Before we model MRAM reversal via a spin polarised current in a future chapter, we first explore the effects of thermal fluctuations on the magnetisation of the free layer for our PSA-MRAM tower structures. Tower structures with such small diameters as modelled in this study have received very limited experimental or computational study at the time of writing. This chapter therefore explores the effects of thermal fluctuations on the reversal mechanism and the coercive field of PSA-MRAM towers of different free layer thicknesses. The details of the towers studied in this chapter are outlined in subsection 2.4.3, since this chapter only involves changing the free layer thickness. The work on the thermodynamic properties and switching dynamics of PSA-MRAM was published in the Journal of Condensed Matter Physics [116].

3.1 Magnetic Susceptibility

Firstly, we explore the static equilibrium properties, namely the isotropic longitudinal susceptibility, using the Monte Carlo method outlined in subsection 2.2.1. The magnetic susceptibility describes the relative ability of a materials atomic sites to align along a given magnetisation direction, thus may also be used to indicate how strongly a material responds to an external magnetic field. Physically it is the ratio between the material magnetisation and the applied field. For a ferromagnetic material, the susceptibility curve should follow a characteristic shape with a distinct peak, described by the Curie-Weiss law. The Curie-Weiss law is given by

$$\chi = \frac{C}{T - T_c} \tag{3.1}$$

where χ is the susceptibility, C is the material dependent Curie constant, T is the temperature and T_c is the Curie temperature. The Curie-Weiss law thus describes the characteristic peak found around the materials Curie temperature, T_c, with a singularity at this point. The Curie temperature acts as a threshold for a ferromagnet, since the Curie temperature is the point in which a material transition from ferromagnetic to paramagnetic behaviour. Since temperature is included via the thermal fluctuations of each atomic site, and the susceptibility is related to the magnetisation spin which is directly related to the temperature, averaging the atomic spins to find a mean susceptibility is a sensible approach. The mean magnetic susceptibility is given by

$$\chi_\alpha = \frac{\sum_i \mu_i}{k_B T}(\langle m_\alpha^2 \rangle) - \langle m_\alpha \rangle^2) \tag{3.2}$$

where $\alpha = x, y, z, m$, which describes the directional components of the magnetisation (x, y, z), in addition to the isotropic longitudinal susceptibility $\alpha = m$, in units of Tesla^{-1}. Since different layers in an MRAM stack can be made of different materials which have different Curie temperatures (which in our model impacts the exchange constant), there are four components of the mean magnetic susceptibility for each individual material. As a result, it is easy to plot the free layers behaviour in isolation from other layers. In this section, plots of χ_m, the longitudinal susceptibility, are used to compare the behaviours of different free layer thicknesses in Figure 3.1 and Figure 3.3.

To obtain these results, the PSA-MRAM tower is fist equilibrated for $10,000$ Monte Carlo steps at a temperature T, during which no statistics are taken. Then, a time-series programme allows the system to evolve for $20,000,000$ further Monte Carlo steps at the same temperature T. The averaged value of all atomic sites in a material for the longitudinal susceptibility, χ_m, after the final step then serves as the data point for that temperature T. This is then repeated for all temperatures in the range $0 < T < 1300$ to obtain the plots in this section. The large number of Monte Carlo steps was required as the tallest towers showed a lot of thermal noise at higher temperatures if the number of Monte Carlo steps was reduced too far. The temperature range had to be large enough to include the characteristic peak around the Curie temperature, which is known to be around $T_C \approx 1100K$ for CoFeB [107].

First, we plot the mean isotropic longitudinal susceptibility for the whole free layer for five different free layer thicknesses in Figure 3.1. The tallest tower's peak in Figure 3.1 was an order of magnitude larger than the smallest tower, making it difficult to compare them all on one graph. The susceptibility was therefore divided by the tower's free layer thickness to normalise them on the same graph for comparison, hence the change of units to mT^{-1}nm^{-1}. We see that as the free layer thickness increases the characteristic peak gets taller, noisier and wider, suggesting more correlated spins with reduced free layer volume. This is explained as a consequence of inadvertently mixing the longitudinal and transverse susceptibility in

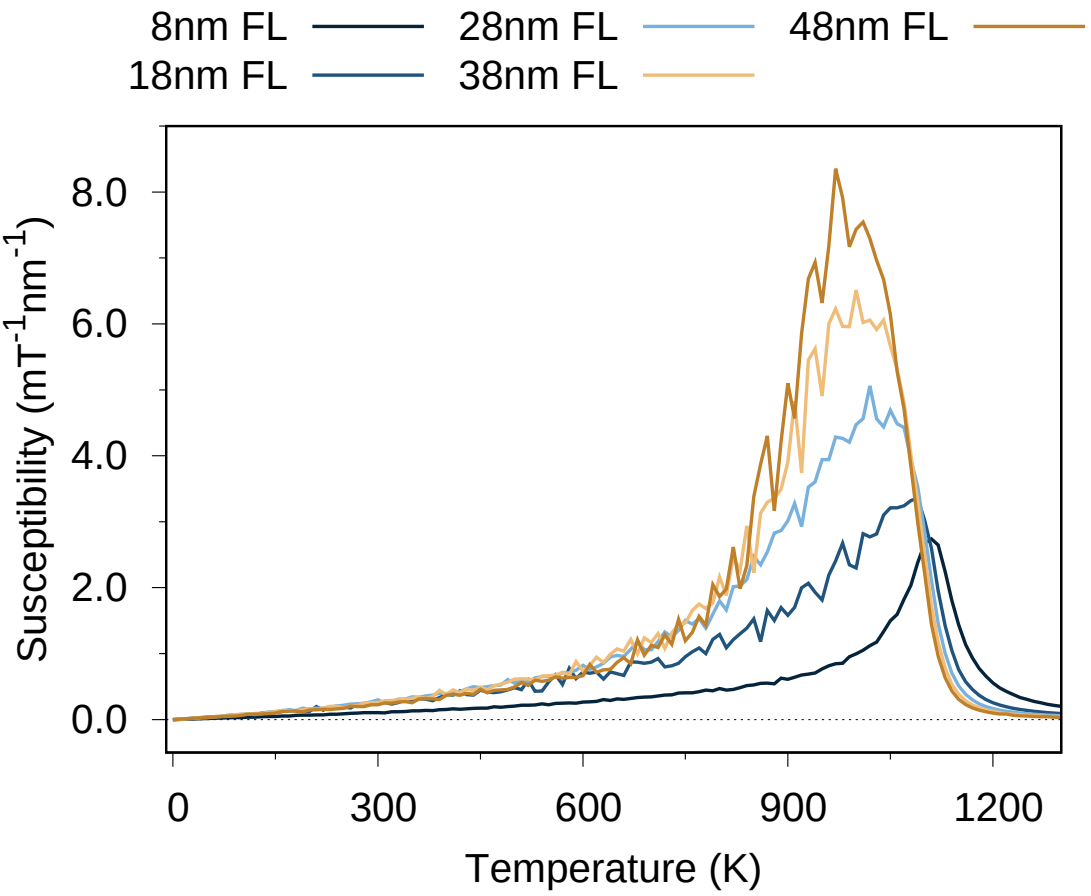

Fig. 3.1 Susceptibility against temperature for the free layer of each height tower. As the thickness decreases the curves are smoother and the peak is lower. This suggests more correlated spins as the free layer volume decreases, which may predict a trend towards coherent rotation.

the taller towers, since we are simply plotting an averaged susceptibility of the entire free layer as shown in Equation 3.2. The longitudinal susceptibility should describe fluctuations in exchange length, and will be present in all height towers. This will increase as temperature is increased, with a large peak at the material's Curie temperature. However, there is also transverse susceptibility, which stems from fluctuations in the magnetisation direction perpendicular to that of the magnetisation orientations (the z direction). The fluctuations in the magnetisation of each atomic site is due to thermal fluctuations, as outlined in the chapter 2. With greater thermal fluctuations, the spin direction may fluctuate by larger amounts. Thermal effects are able to excite long wavelength spin waves. This introduces transverse components to the susceptibility if the free layer is thick enough. A simple diagram is shown in Figure 3.2, where in part a) the spins are all aligned in one direction, but may fluctuate in length (longitudinal), while in b) they fluctuate in both length and direction over

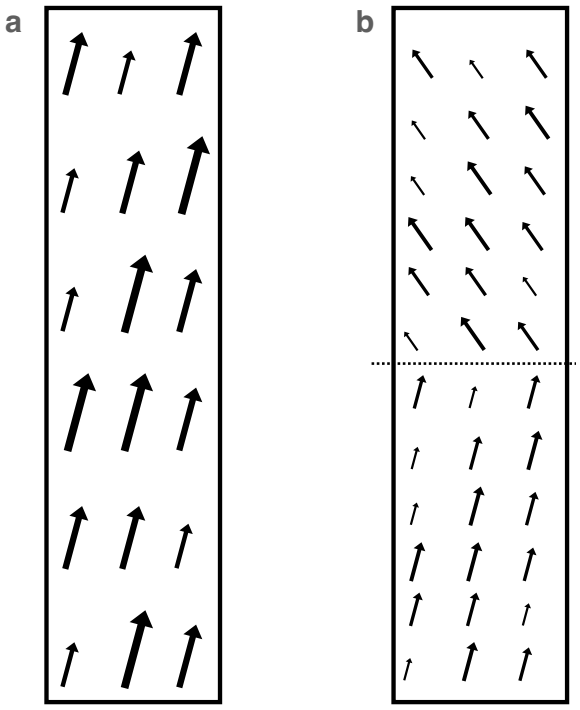

Fig. 3.2 A simple demonstration of a) longitudinal susceptibility only, whereby the exchange length may fluctuate but the direction is consistent, and b) longitudinal and transverse susceptibility, whereby neighbouring spins fluctuate on exchange length, but distant spins may also fluctuate slightly in direction too.

enough volume.

Based on this description, it is therefore expected that the smallest tower is predominantly longitudinal susceptibility, since any fluctuations in magnetisation direction are negligible due to the exchange interaction and equation 3.2 would predominantly give us longitudinal susceptibility. Conversely, in taller towers, an undesired consequence of increasing the thickness is that it inadvertently adds transverse susceptibility too, since fluctuations in magnetisation direction at the bottom of the free layer versus the top of the free layer may be much less correlated, presenting much larger peaks. The peak shifting to the left with increased free layer thickness is therefore a product of coherency. The peak of a small free layer is caused only by thermal fluctuations, while taller towers additionally suffer from a loss of coherency. This causes a lower Curie temperature, along with a taller peak.

To prove that this is the case, the tallest tower from Figure 3.1, which had a 48 nm free layer, is divided into 10 nm sections (with one 8 nm section to make 48 nm). The new 10 nm sections have the same material parameters (exchange constant, damping etc.) as when it was one continuous 48 nm free layer, the only difference is that we can now obtain the

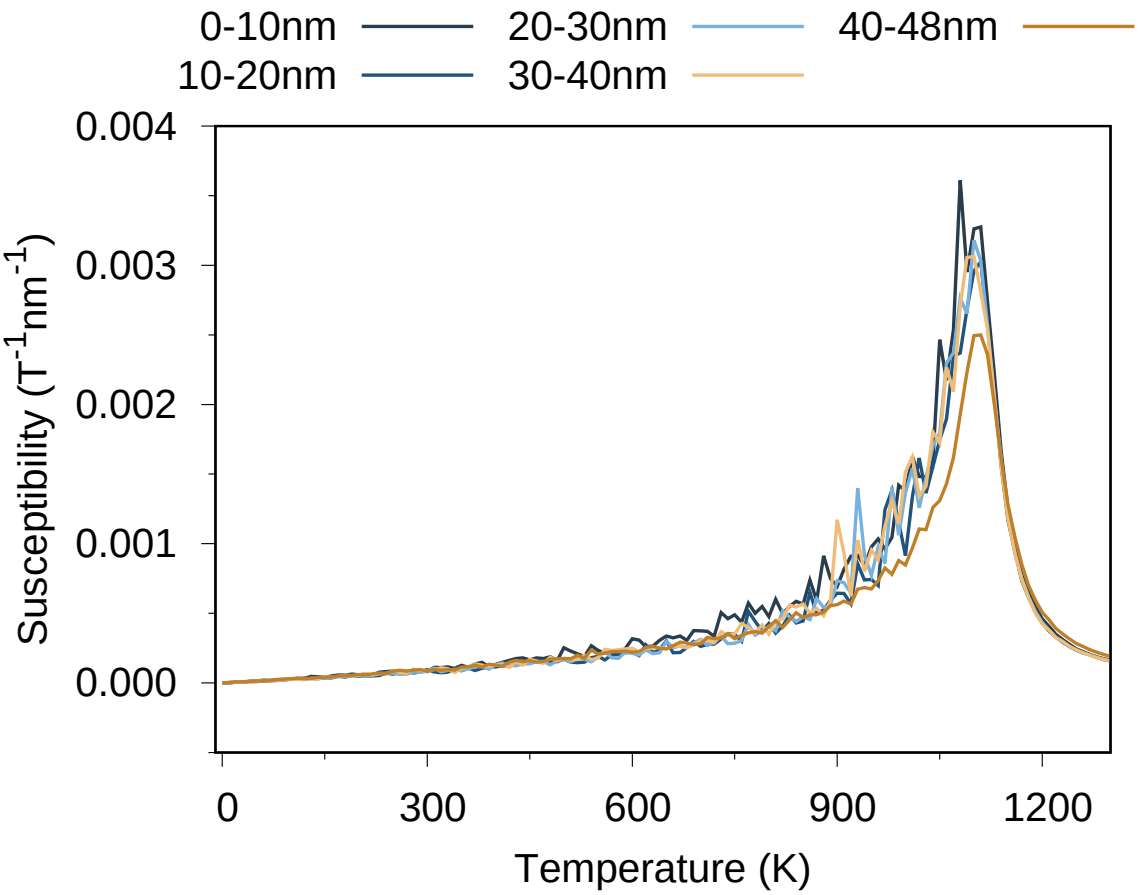

Fig. 3.3 Susceptibility against temperature for the free layer of the 48nm free layer divided into local 10nm regions. The localised curves are the same height and width (with the slightly smaller 8nm thickness having a slightly reduced peak). This demonstrates that locally, the spins are correlated, so any noise in fig. 3.1 is a consequence of variation in spin direction or non-uniform excited modes.

mean susceptibility for 10 nm sections, rather than the whole free layer. In Figure 3.3 the susceptibility of these smaller 10 nm sections are plotted against the temperature, where the susceptibility is again normalised by the free layer height to keep the units the same as Figure 3.1, for easier comparison. This confirms that, within local 10 nm sections of the tallest tower, the susceptibility is actually behaving the same as the 8 nm case in Fig. 3.1, with the peak reaching the same magnitude. This suggests that the taller towers must have non-uniform magnetisation modes throughout the stack, since there is increased transverse susceptibility in taller free layers. This may be used to predict that the reversal mechanism for taller towers will be incoherent, whereas the smallest tower would be expected to be closer to coherent rotation, as it is closer to uniform magnetisation.

3.2 Hysteresis

In this section, the dynamic properties of the free layer are examined from hysteresis loops and modelled using the LLG equation outlined in subsection 2.2.3. In all the hysteresis loops in this section, the PSA-MRAM tower is first equilibrated for $10,000$ time steps ($\Delta t = 1.0fs$), meaning the spins are left to equilibrate towards a ground state in the absence of any field. Once equilibrated, an external magnetic field of $1T$ was applied along the easy axis (along the positive z-axis). This is then reduced to $-1T$, then returned back to $1T$, in steps of $0.01T$. At each field increment, $100,000$ time-steps at $1.0fs$ each occur, since the materials magnetisation does not equilibrate with the external field immediately. As a result, a complete hysteresis cycle takes around $40ns$ in total. The speed of the equilibration at each field increment is directly related to the Gilbert damping, which is $\alpha = 0.001$ for the bulk of the free layer and $\alpha = 0.11$ for the enhanced monolayer, as discussed in subsection 2.4.3. For this section, however, the Gilbert damping is changed to $\alpha = 1$ for all layers, referred to as critical damping, to allow a more rapid relaxation than would occur normally. This reduces the number of time-steps required to equilibrate at each field increment without impacting the magnetic behaviours being explored. Failure to equilibrate leads to a larger coercivity on the hysteresis loops, so the field sweep rate cannot be too high. However, too large a number of time-steps at every field increment would become prohibitively computationally expensive. It is worth noting, therefore, that doing $100,000$ time steps at every field increment is a compromise, minimising the error of a fast sweep rate while remaining computationally viable.

3.2.1 Thermal Averaging

One important feature of atomistic models is the ability to capture thermal effects as outlined in subsection 2.2.4. The thermal fluctuations for every spin in the system, at every time-step throughout a simulation, depends on a sequence of random numbers. Running a simulation with the same starting seed number will produce the same sequence of random numbers, thus allowing for reproducibility in the results. However, altering the starting seed number will create a different sequence of random numbers, which results in a unique evolution of the thermal fluctuations. As the temperature increases, the width of the Gaussian increases, representing stronger thermal fluctuations for each spin in the system. This exaggerates the discrepancy in the final spin states between different starting seeds, compared to lower temperatures, where the difference will be minimised as the spins response to small thermal fluctuations will be small. Towards operational temperatures for most devices (room

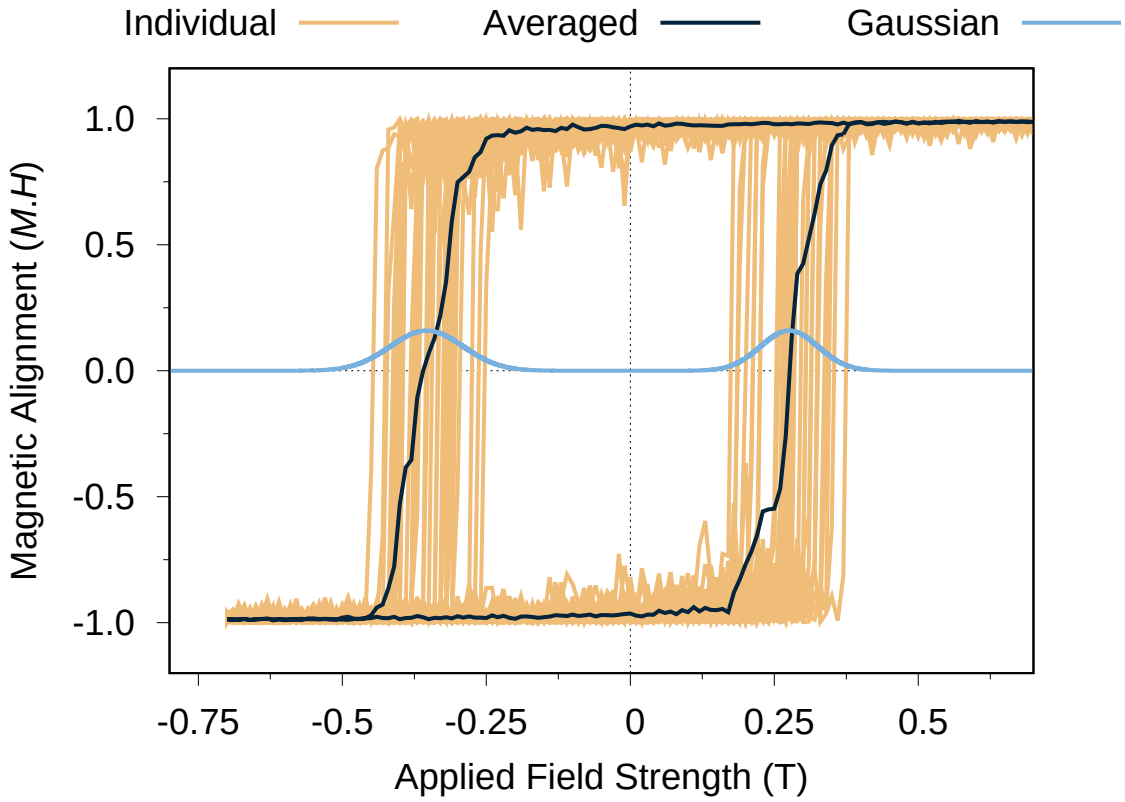

Fig. 3.4 Forty individual hysteresis loops each with different integration seeds, and the averaged loop, at 300 Kelvin. We see the randomness of thermal fluctuations changes the precise point the system switches, so the averaged loop has a curved shape representing a switching field distribution (SFD). All subsequent hysteresis loops in this chapter are averaged in this way.

temperature) switching may become partially thermally driven, and the exact coercivity for a material may be unknown. This reflects the stochastic nature of thermal fluctuations in reality, but must be accounted for when using hysteresis plots to determine magnetic properties.

For the CoFeB modelled in this thesis, $300K$ provides large enough thermal fluctuations to demonstrate this point, as seen in Figure 3.4. Each individual run produces a square loop, representing a precise coercivity. Rerunning the same starting seed would produce an identical square loop. This is not realistic, since thermal fluctuations in reality are random, leading to some uncertainty in the exact coercivity. Forty individual runs, with a different starting seed each, are plotted in Figure 3.4 to demonstrate the difference between them.

Across 40 independent loops, a normal distribution of switching fields appears. The range of switching fields is referred to as the switching field distribution (SFD) and represents an uncertainty in the precise switching field of the free layer. Averaging all of the individual square loops produces a curved loop, which is also shown in Figure 3.4. The curvature of the

averaged hysteresis loop represents the SFD, corresponding to the small expected uncertainty in the systems switching field. In other words, the SFD is the difference between the leftmost and rightmost square curve for eaching switching event.
To produce curved loops that capture the correct width of the SFD, a sufficient number of square loops need to be averaged. Thermal fluctuations follow a Guassian distribution, so the criteria for an appropriate number of square loops is that the range of square loops should also be a Gaussian distribution. In subsection 3.2.3 of this chapter, the SFD and coercivity for the curved averaged loop is extracted by fitting the data to an error function. The details of this process are found in that section, but using the SFD and coercivity for the averaged curve shown in Figure 3.4, two Gaussian distributions can be produced, one for each reversal direction. These two Guassian's are also found on Figure 3.4. This demonstrates that, for forty independent square loops, the majority fall within the peak of a Gaussian distribution, with some standard deviations either side of the peak. This concludes that forty loops are sufficient for the averaging process, which is in agreement with previous atomistic studies of MRAM [82].
To summarise, after around 30 unique runs, the graphs had a clear switching range. Going beyond forty independent square loops does not produce a wider range, shown with a Gaussian distribution. As an example, there is a clear SFD of around $0.2T$ across the 40 individual plots for both the parallel and anti-parallel switch in Figure 3.4. Simply adding all the output files together and dividing by 40 produces an average plot of the 40 individuals, where the hysteresis loop is now curved. The curvature of the loop therefore shows the SFD at that particular temperature, which represents the uncertainty in the precise switching that is expected in reality. All subsequent hysteresis plots in this chapter are thus averaged in this way.

3.2.2 Results

A systematic approach was taken to explore the effect of temperature and free layer thickness on the hysteresis curves. As a starting point, hysteresis curves of five different equally spaced thicknesses of free layer (8 nm, 18 nm, 28 nm, 38 nm, and 48 nm) at three different temperatures are plotted and discussed in this section. The first temperature is the idealised 0 K, and the last temperature is room temperature (300 K), since this is operational temperature for many devices. A central temperature of 150 K is included to begin to explore the trends.
Firstly, in Figure 3.5, the idealised case of 0 K is seen for the five thickness free layers. This is a useful inclusion, since without any thermal fluctuations, this represents the difference in the shape anisotropy of the free layer, as a consequence of its thickness. This allows us to explore the size effects first. The thermal averaging discussed in subsection 3.2.1 is not

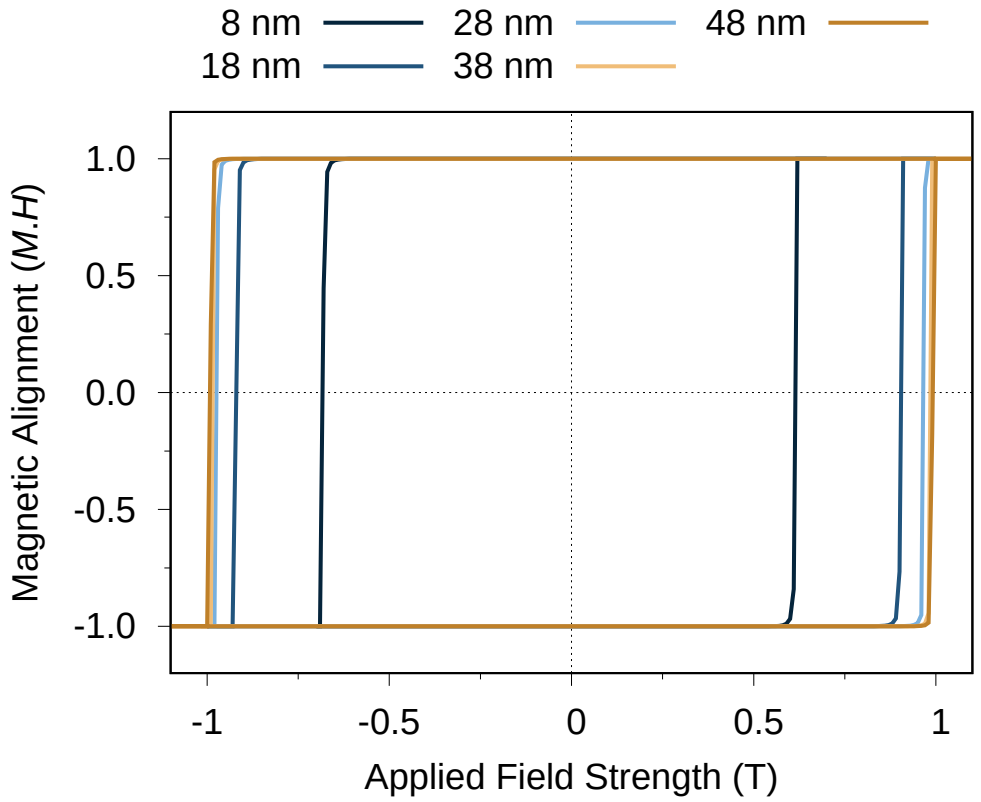

Fig. 3.5 The hysteresis curves for five different free layer thicknesses at 0 K. The thicker free layers have reached an asymptotic maximum for the coercivity, with a small reduction when decreased to 18 nm and a significant reduction when reduced further to 8 nm.

required for the 0 Kelvin case, since in the absence of thermal fluctuations there is no need for the random numbers. At 0 K, the hysteresis loops would be perfectly square theoretically, however a very small curvature is observed in these plots due to the ballistic effect caused by a finite step size during simulation. There is also a very small amount of curvature because the free layer at $0K$ is initialised 1° off the easy axis for a minimum torque. This curvature is therefore fictitious and not representative of a thermal switching field distribution.

The three tallest towers appear to have reached an asymptotic maximum, while the 18 nm thick free layer shows a small reduction in coercivity, and the 8 nm shows a significantly reduced coercivity. The tallest three towers appear to be approaching an asymptotic maximum value for the coercivity, with the 18 nm free layer slightly reduced followed by a comparatively large reduction for the 8 nm free layer. This is understandable, as the coercivity is related to the anisotropy of the system, and the shape anisotropy does not increase linearly. The asymptotic limit observed for the taller free layers is therefore a consequence of reaching maximum shape anisotropy for cylinders of this diameter. When the thickness of the towers is

reduced to below 30 nm, the rapid reduction of stability as the free layer thickness is reduced could pose significant limitations on the usage for these 5 nm diameter MRAM designs. Since the diameter of the studied MRAM towers is only 5 nm wide, an 8 nm thick free layer is approaching its width, which explains the significant loss of shape anisotropy and resulting drop in coercivity. Since increasing the thickness beyond ≈ 30 nm does not seem to increase the coercivity, these results also suggest that nothing would be gained by creating thicker free layers than this threshold for cylindrical MRAM devices of 5 nm diameter. It also suggests that an 18 nm thick free layer only has a slightly reduced coercivity from this maximum threshold, so may still be viable dimensions for reliable MRAM. However, further study on the energy barrier of the free layer for these shapes and dimensions is required to confirm or deny if this is the case.

To support the statement that the 8 nm thick free layer has significantly reduced shape anistropy, the demagnetisation factors were output by VAMPIRE during these simulations and are shown in Table 3.1. Here, we see the diagonal components of Equation 2.22, since the off-diagonal components are near zero. Clearly, the tallest three towers have significantly larger demagnetisation factors in the x-y plane ($N_{xx} = N_{yy}$) than along the easy axis (N_{zz}), resulting in a strong preference for the spins to align along the easy axis. This is responsible for the tallest three towers larger coercivity at 0 K. The 18 nm tower suffers from a larger z-component for the demagnetisation factor, but it is still roughly $4\times$ greater in the x-y plane, resulting in almost as much shape anisotropy as the taller towers, though slightly reduced. The 8 nm tower is much closer between the x-y plane and the easy axis, representing significantly reduced shape anisotropy compared to the taller tower, hence the significant drop in coercivity at 0 K.

While the demagnetisation factors calculated are exact and will be used throughout this thesis, it is still useful to compare to an analytical approach. General formulas for the determination of the demagnetising factors of general ellipsoids were found by Osborn [117]. The ellipsoid semi-axes are labelled a, b, c and the general formulas are derived under the assumption $a \geq b \geq c \geq 0$. For this work, the diameter of the towers in the x-y plane is 5 nm and the height of the tower is always larger, at a minimum of 8 nm. The appropriate formulas from Osborn's paper are that of a prolate spheroid ($b = c$), reproduced below.

$$\begin{aligned} \frac{N_{zz}}{4\pi} &= \frac{1}{m^2-1}\left[\frac{m}{2\sqrt{m^2-1}} \times \ln\left(\frac{m+\sqrt{m^2-1}}{m-\sqrt{m^2-1}}\right) - 1\right] \\ \frac{N_{xx}}{4\pi} &= \frac{N_{yy}}{4\pi} = \frac{m}{2(m^2-1)}\left[m - \frac{1}{2\sqrt{m^2-1}} \times \ln\left(\frac{m+\sqrt{m^2-1}}{m-\sqrt{m^2-1}}\right)\right] \end{aligned} \tag{3.3}$$

Where $m = \frac{a}{c}$. These analytical results are added to Table 3.1 in columns four and five for comparison with those obtained in VAMPIRE.

	$N_{xx} = N_{yy}$	N_{zz}	$N_{xx} = N_{yy}$ (Osborn)	N_{zz} (Osborn)
8 nm	0.389689	0.220621	0.390643	0.218713
18 nm	0.443401	0.113199	0.456761	0.086477
28 nm	0.461259	0.077482	0.476166	0.047667
38 nm	0.470135	0.059726	0.484666	0.030668
48 nm	0.475376	0.0492476	0.489204	0.021592

Table 3.1 Demagnetisation factors for the different free layer dimensions, showing the loss of a dominant direction with reduction in volume. This loss of shape anisotropy significantly reduces the coercivity and stability factor for the 8 nm tower and represents a limitation in scalability. The final two columns are the analytical demagnetisation factors for a prolate spheroid for comparison.

The numerical demag factors and those calculated from Osborn are in reasonable agreement. The numbers differ because the Osborn formula is for a prolate spheroid whereas the towers built in VAMPIRE for this thesis are cylindrical. However, the ratio between the x-y components and the z-component are seen to be in agreement, predicting identical trends as a function of free layer volume.

Another important observation in Figure 3.5 is a very small bias between the right hand and left hand branch, which is due to the long range demagnetisation field stemming from the CoPt SAF and reference layer [45]. As discussed in subsection 2.4.2, the thickness of the bottom CoPt layer was adjusted to minimise the stray field present in the free layer. It is very challenging to completely remove the stray field, as discussed in that section of this thesis. Similarly, it is not possible to create perfect structures experimentally, thus the real PSA-MRAM systems that are being emulated will have stray fields too. For this reason, a small stray field in the free layer is acceptable, which results in the very small bias. The free layer therefore has a very small preference for being aligned with with the reference layer. In other words, a very slightly stronger field is required to switch from aligned to anti-aligned compared to the reverse. It is worth considering an alternative possible contribution towards a bias. It could also originate from distortions of the magnetisation at the MgO/CoFeB interfacial layer in anti-parallel alignment (often referred to as a flower state [118]). However, in Figure 3.5, there is no evidence of a significant flower state in any of the studied structures. Therefore, the magnetisation can be considered essentially uniform across the x-y plane for such small lateral sizes. In reality, there is likely to be very small distortions, but due to the exchange constant being very large for so few atoms, the distortions are insignificant.

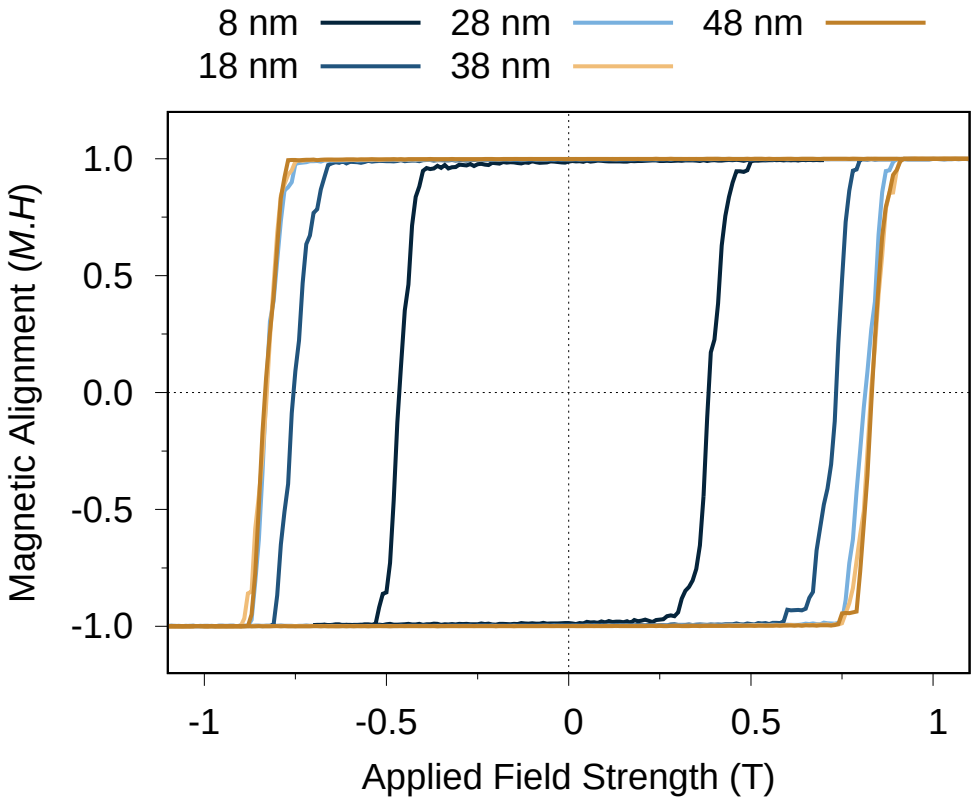

Fig. 3.6 The hysteresis curves for five different free layer thicknesses at 150 K. The trend in the reduction of coercivity with free layer thickness is the same as at 0 K, but now there is additional curvature in each loop as the switching becomes partially thermally driven.

This contribution to the bias is therefore ignored for the rest of this thesis, with the long range demagnetisation field the sole contribution to the bias. It was worth considering this alternative, as this effect is expected to become more dominant in towers of greater diameter. Secondly, in Figure 3.6, the hysteresis plots for the same five free layers are plot, but at 150 K. While this temperature is below the reasonable operational temperatures of most MRAM devices (a range from around -55^oC for military extremes, to 400^oC for automotive extremes [113]) it is nonetheless useful to see the trends present. Comparing the 0 K hysteresis loops to the 150 K hysteresis loops, it is clear that all five towers have a reduced coercivity with thermal fluctuations added. The inclusion of thermal fluctuations causes random noise in the precession of the atomic spins which is not present in the idealised 0 K case. This thermal noise naturally captures a reduction in the materials anisotropy and magnetisation, and is responsible for the reduction of the materials coercivity. The 40 hysteresis loops at 150 K produce a switching field distribution, as shown and discussed for Figure 3.4. As a result, the hysteresis plots are now curved, rather than square loops, representing a small uncertainty

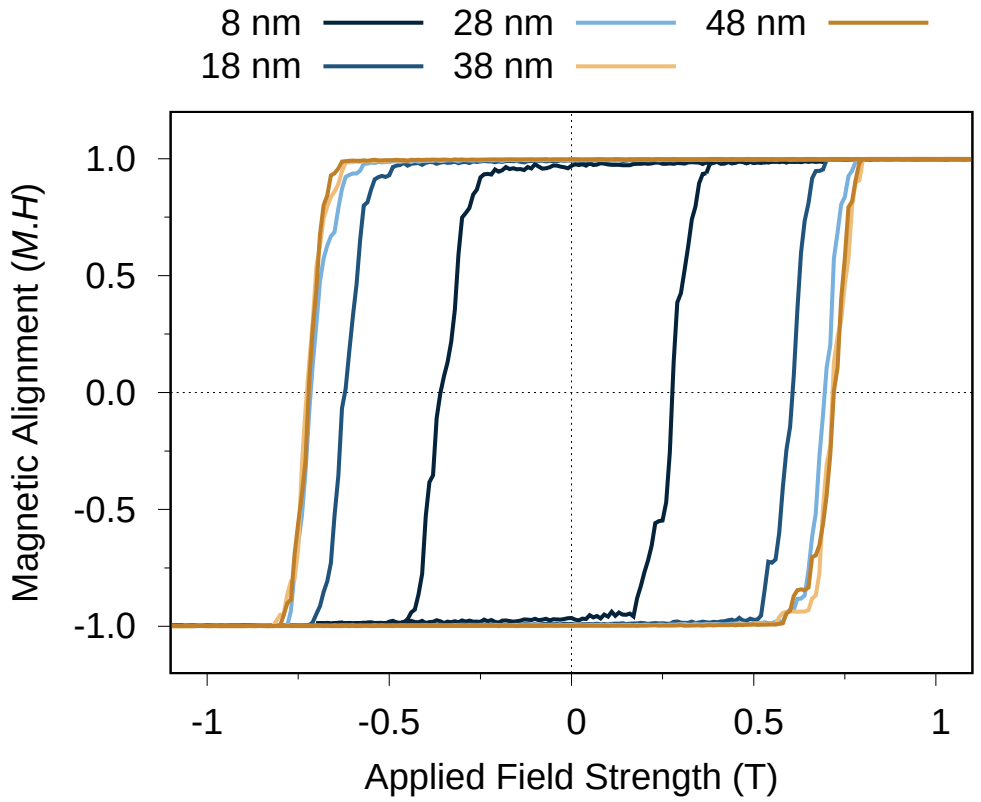

Fig. 3.7 The the hysteresis curves for five different free layer thicknesses at 300 K. The coercivities have reduced when compared to 150 K and 0 K, with increased curvature due to an increase in the switching field distribution.

in the precise switching field for the material. The curvature of each branch is relatively shallow, as the thermal fluctuations are small at such a low temperature. Interestingly, the tallest three towers are still at an asymptotic maximum, in other words, they have the same reduction in coercivity for this temperature increase. Once again the 18 nm thick free layer has a slightly reduced coercivity compared to the asymptotic maximum the tallest three towers demonstrate. However, in the 0 K case, the 18 nm free layer was only slightly reduced compared to the tallest towers, whereas the the difference in coercivity at 150 K is grown slightly. Ditto, the separation in the coercivity between the 18 nm and the 8 nm thick free layers has grown slightly for the 150 K case compared to the 0 K case.

Finally, in Figure 3.7, the hysteresis plots are shown at 300 K. In addition to adding to the trend of increasing temperature, 300 K is around operational temperature for the majority of potential MRAM devices. Again, all thickness free layers see a reduction in coercivity compared to the 150 K hysteresis plots. Larger thermal fluctuations results in a greater switching field distribution, since it provides a greater chance of the switching being partially

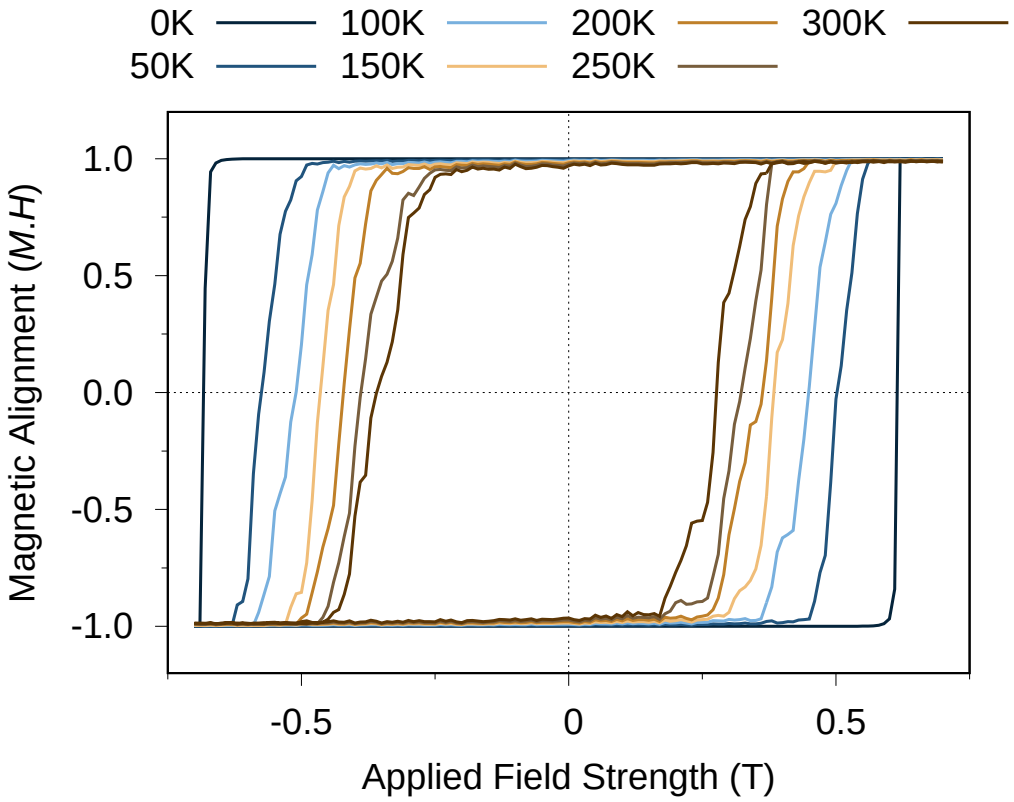

Fig. 3.8 Hysteresis curves with increasing temperatures for the 8 nm thick free layer. The curved shape of the loop becomes more exaggerated with temperature representing an increased switching field distribution. This suggests that thermal effects are driving the switching mechanism.

thermally driven. As a result, when the 40 loops are averaged to produce these hysteresis plots, the width of the curve from one orientation to the other is wider when compared to the 150 K case. Therefore, the switching mechanism is increasingly thermally driven towards operational temperatures, demonstrating the importance of including thermal effects in models of MRAM. Physically, it means that the uncertainty in the precise field required for free layer switching grows as temperature increases, with a significant loss of thermal stability for the 8 nm tower at operational temperatures.

The bias between the left and right hand branch, discussed for Figure 3.5, is also present at finite temperature in Figure 3.6 and Figure 3.7. The bias between the right hand and the left hand coercivity for all heights at all temperatures is 0.09T to two decimal places. This is worth noticing, because the bias in the free layer stems from the stray field emanating from all other layers. Since this does not change to two decimal places at increased temperature, the reference layer/ SAF layers must not deviate significantly from their vertical magnetisation

from the equilibration phase. Noticing this result is therefore a recognition of the stability of the reference layer, which was the purpose of the CoPt layers. Beyond two decimal places, there is a very slight decrease in the bias as temperature increases, of around 0.001T between 0 K and 300 K. This is because, at finite T, the lower layers will always deviate a small amount from the idealised vertical magnetisation due to thermal fluctuations. As a result, a slightly smaller stray field is present in the free layer compared to 0 K.
To further see the trend in temperature, Figure 3.8 plots the hysteresis loops for the 8 nm free layer, but with more temperatures. The trend is a clear decrease in the coercivity for every 50 K increase in temperature, with a slowly wider switching field distribution at each temperature.

3.2.3 Coercivity Extraction

There are two main interests in the hysteresis plots in the previous subsection, the coercivity and the switching field distribution (SFD). The coercivity is the field point at which the hysteresis plot crosses 0.0 magnetic alignment during switching. But above 0 Kelvin, all hysteresis plots show curvature, whereby the loop begins to switch before the coercivity point is reached (and continues this curvature after the coercivity point). This curvature is due to the range of coercivities capable of switching the free layer, in other words the SFD (see subsection 3.2.1). For analysis, it is therefore useful to be able to extract a value for the coercivity, but also the switching field distribution, in all of the hysteresis loops presented so far. A low coercivity and high SFD present challenges for stability and recording quality of MRAM devices.
To extract the coercivity and the SFD, every branch of every hysteresis plot is fitted to an error function, which takes the form

$$\mathrm{erf}(x) = \frac{2}{\sqrt{\pi}} \int_0^x \exp\left(-t^2\right) dt \tag{3.4}$$

where, because the curves are not centered on $x = 0$, x is given by

$$t = \frac{x - x_0}{\sigma}. \tag{3.5}$$

x_0 is then the shift from $x = 0$, so provides the coercivity, while σ is the standard deviation. The error function is the integral of the normalised Gaussian function, thus provides the cumulative distribution of a Gaussian. This is how the two Gaussian functions were plotted on Figure 3.4 in subsection 3.2.1, using $\frac{1}{2\pi} e^{-\frac{(x-x_0)^2}{\sigma^2}}$ and the extracted value of x_0 and σ for that curve.

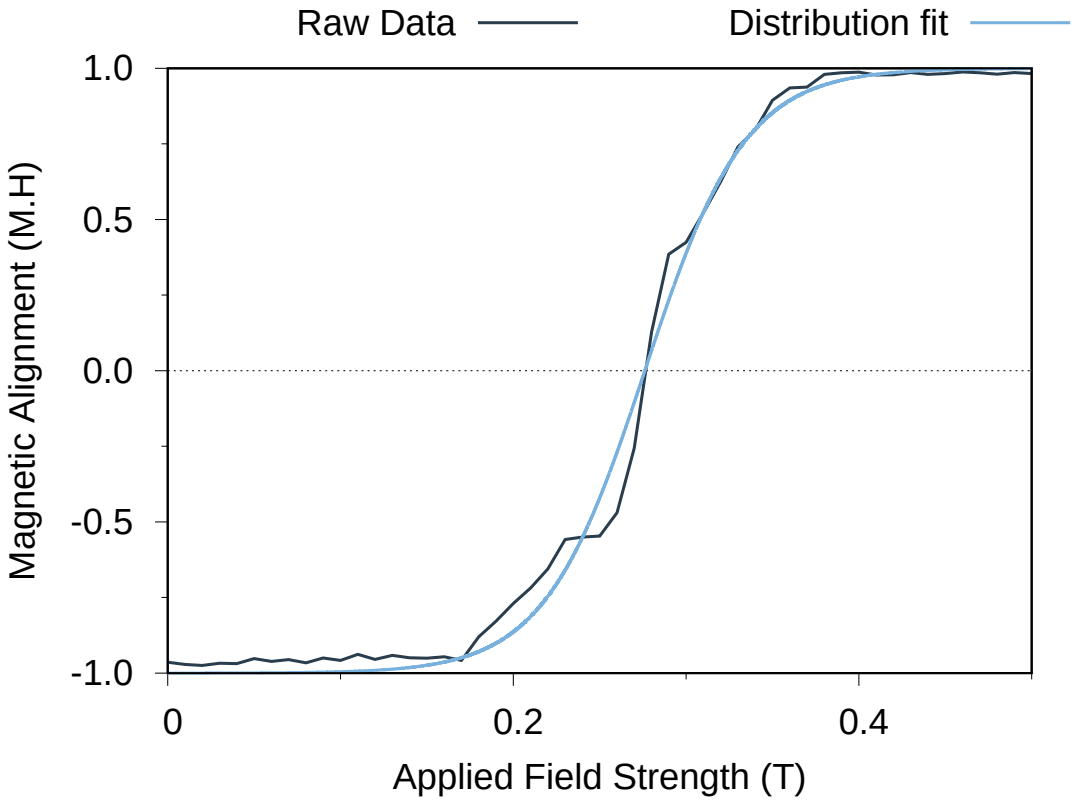

Fig. 3.9 The right hand branch of the hysteresis curve for the 8 nm thick free layer at 300 Kelvin with its fit curve from equation 3.4. Here we observe the fit is reasonable for crossing the axis at the right point and we extract a coercivity of 0.28 T and a standard deviation of 0.10 T to 2 significant figures.

For clarity, an example is included in Figure 3.9, where the right hand branch of the 8 nm free layer at 300 K is chosen, due to its clear curvature. By fitting Equation 3.4-Equation 3.5 to the raw data using Gnuplot, a coercivity $x_0 = 0.28T$ is extracted, with a SFD $\sigma = 0.10T$. For this example, the extraction of this data means that for the 8 nm free layer at 300 K, an external field of $0.28 \pm 0.10T$ is required to switch the free layer from the anti-aligned to the aligned state. The extraction of the coercivity and the SFD therefore provides context that the hysteresis plots alone do not capture, since in this example, the uncertainty in the precise switching field (SFD) is significant compared to the approximate field (coercivity). This process can be applied to every branch of every hysteresis plot to provide an alternative way to compare and explore the trends for the impact of temperature and free layer thickness on stability.

This fitting has been applied to the right hand branch of every hysteresis plot, so a plot of the coercivity as a function of temperature is shown in Figure 3.10. The crosses are the values for x_0 obtained from each fit, while the solid line is the Sharrock fit which is discussed

in section 3.3. The SFD represents an inherent uncertainty in the precise coercivity, and thus is represented as error bars at each point in the figure. The focus in this section is the crosses and error bars, ignoring the lines. As previously discussed, the small curvature of the hystersis loop at $0K$ is due to the ballistic effect, not an SFD, and therefore those data points do not have error bars.

Of course, the same trends are visible in this representation as they were in the hysteresis plots. A fairly linear drop in the coercivity with every $50K$ increase in the temperature is seen for all free layer thicknesses. The tallest two towers are clearly approaching some asymptotic maximum, while the third tower actually appears to have a slightly reduced coercivity. The 18 nm free layer then has a much more clearly noticeable drop in the coercivity, followed by a significant drop in coercivity for the 8 nm free layer at all temperatures. This was all noticed and discussed in the hysteresis plots in the previous subsection. The key difference in this representation of the data lies in the error bars, meaning the SFD can now be compared in a way that was not easily possible in the standard hysteresis loops.

Firstly, while the reduction of the coercivity as the temperature increases was already observed in Figure 3.5, 3.6 and 3.7, it can now further be seen that the trend is virtually identical regardless of the free layer thickness. This is an interesting observation, since it suggests the temperature dependence of the coercivity is independent of the trends in free layer volume. As a result, this is not something that may be engineered away with volume changes in the MRAM stack. It is challenging to observe this feature in the previous hysteresis plots, supporting the decision to express the coercivity in this way.

Secondly, the overlap of the SFDs between the different height towers is now more obvious in Figure 3.10. The error bars that drop below the extracted coercivity represent a reduced field, be- low the coercivity, that could begin to switch the free layer due to the thermal fluctuations driving the switching process. There is therefore an uncertainty in the precise field required to switch the free layer, since it could theoretically happen at any field point within the error bar. The new observation, therefore, is that the three tallest free layers in Figure 3.10 have overlapping SFDs for all finite temperatures, implying they could all be switched at the same field. This is in contrast to the exact coercivity (the precise field strength in a square hysteresis loop) which demonstrates the importance of including thermal effects. The overlap for these tallest towers also adds context to the asymptotic maximum observed in the previous hysteresis loops, since it is now clear that the tallest towers have significant overlap when including a SFD. It also demonstrates how significantly the coercivity drops as the free layer is further reduced to 18 nm and 8 nm thick. We see that the 18 nm thick free layer has a coercivity that is lower than the taller three towers even accounting for the SFD, confirming that the free layers are beginning to lose stability at these dimensions. The

extreme drop in coercivity for the 8 nm free layer is also more obviously compared to the other height towers in this expression of the data, compared to the hystersis loops. For example, the lowest field capable of switching the 18 nm free layer at 300 K (the bottom of the error bar) is still larger than the idealised 0 K field for the 8 nm. This means the best possible case for the 8 nm is still worse than the 18 nm free layer at room temperature. This is not at all obvious from the hysteresis loops.

The final observation that is not found in the hysteresis loops directly, is that the switching field distribution grows larger as the temperature increases. This is expected, since larger thermal fluctuations cause larger fluctuations in the saturation magnetisation and begin to drive the switching process. For all five free layer thicknesses, the increase in the width of the SFD with each 50 K temperature increase is between 0.008T and 0.016T, with the largest increases at the sub-150 K data points.

3.3 Sharrock Model Comparison

It is interesting to compare the obtained coercivity data to that predicted from the Sharrock law, which is an expression for the thermal dependence of the coercivity that comes from the Arrhenius-Neel law. The Sharrock equation takes the form

$$H_c(\tau) = H_a \left[1 - \sqrt{\frac{k_B T}{KV} \ln (f_0 \tau)} \right] \tag{3.6}$$

Most terms represent the standard parameters, where T is the temperature, k_B is the Boltzman constant, K is the anisotropy constant, V is the volume of the switchable layer, τ is the relaxation time and f_0 is the frequency [119, 120]. Slightly less obvious, H_a is described as the anisotropy field ($\frac{2K}{M_s}$), corresponding to the precise field that reduces the energy barrier to zero, while H_c is the coercivity. At 0 K, $H_c = H_a$, but in reality H_c is reduced as thermal fluctuations increase, in addition to being dependent on the anisotropy, shape (volume) and the relaxation time. Thermal fluctuations are particularly important as they partially contribute to transitions over the energy barrier at reduced H_c. The distinction between H_c and H_a is important, because exploiting the fact that $H_a = H_c$ at 0 K will provide a comparison between our temperature dependence for the coercivity with that predicted of Sharrock.

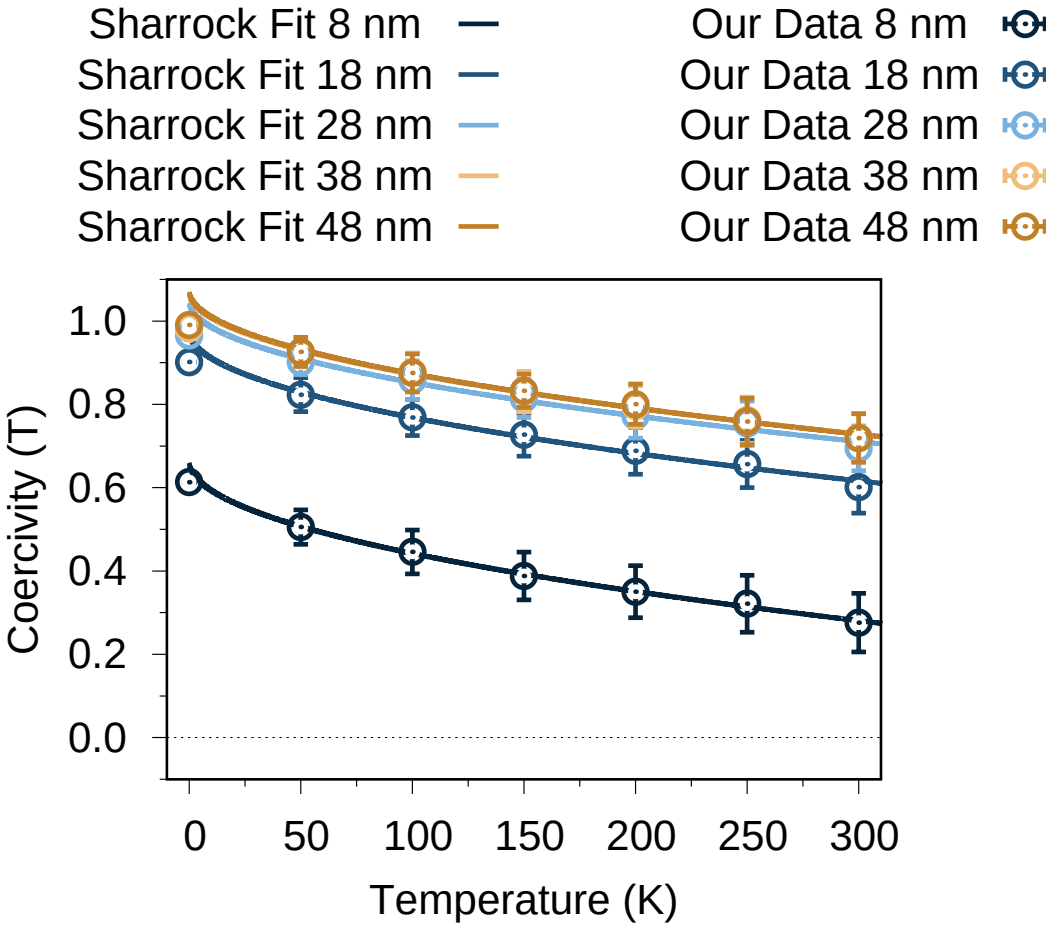

Fig. 3.10 The extracted coercivity with switching field distribution error bars for the right hand switch at each temperature simulation for the free layers. We see the coercivity decrease with temperature and the switching field distribution increases in width. This demonstrates the significant loss of shape anisotropy for the 8 nm free layer, which does not overlap any other free layer thickness.

3.3.1 Fitting Data to the Sharrock Equation

Equation 3.6 describes the temperature dependence of the coercivity, thus it is appropriate to compare this model with the temperature dependence in our model. The temperature dependence of the coercivity from our model was demonstrated in Figure 3.10 for the different thickness free layers. The temperature dependence of the coercivity in the Sharrock model in Equation 3.6 is of the form

$$H_c = A(1 - B\sqrt{T}) \tag{3.7}$$

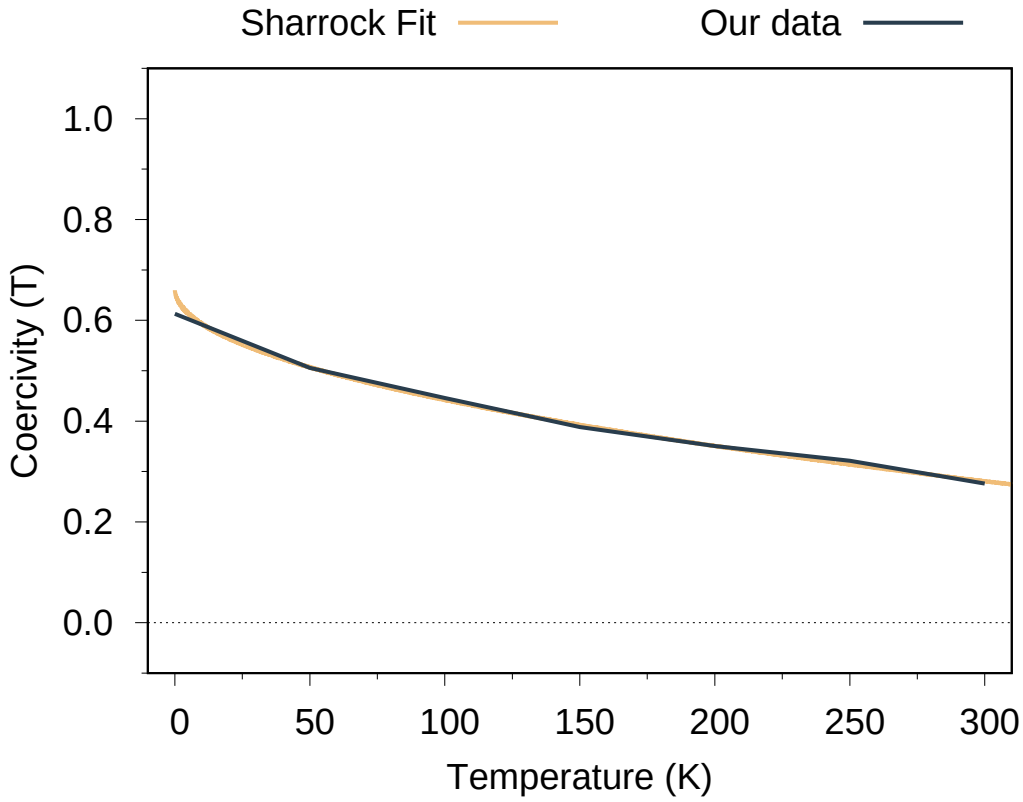

Fig. 3.11 Here, an equation of the form of the Sharrock equation, $H_c = A(1 - B\sqrt{T})$, is fit to the coercivities extracted for the coherent 8 nm free layer in Figure 3.10 at finite temperature. The fit then extracts an estimate for H_a, the coercivity at 0 K. In this fit, $A = 0.66276$ and $B = 0.033278$. The value of A is the anisotropy field H_a and the value of B is used in our approximation of the energy barrier.

Clearly, $A = H_a$ and $B = -\sqrt{\frac{k_B}{KV} ln(f_0 \tau)}$. Fitting Equation 3.7 to the data points in Figure 3.10, excluding the 0 K data point, obtains an optimised value for A and B. These fits are added to Figure 3.10 as lines for comparison between the Sharrock model and the obtained data points. The obtained value for A is then the prediction for H_a from the Sharrock model, which can then be compared to the obtained value for coercivity at 0 K. The value of B will be discussed in the following section on thermal stability.

An isolated example from Figure 3.10 is shown in Figure 3.11 for the right hand branch of the 8 nm free layer. To be clear, the 0 K data point was omitted from the Sharrock fitting, but is included in the figure for comparison purposes. Since the trends are the same for all other height towers in Figure 3.10, the isolated graph in Figure 3.11 is to aid discussion. The values found via fitting Equation 3.7 in the 8 nm example shown in Figure 3.11 are $A = 0.663$ and $B = 0.0333$. The predicted value of H_a from the Sharrock model is therefore slightly higher than that predicted from our model ($H_a = 0.612$). At finite temperature, the

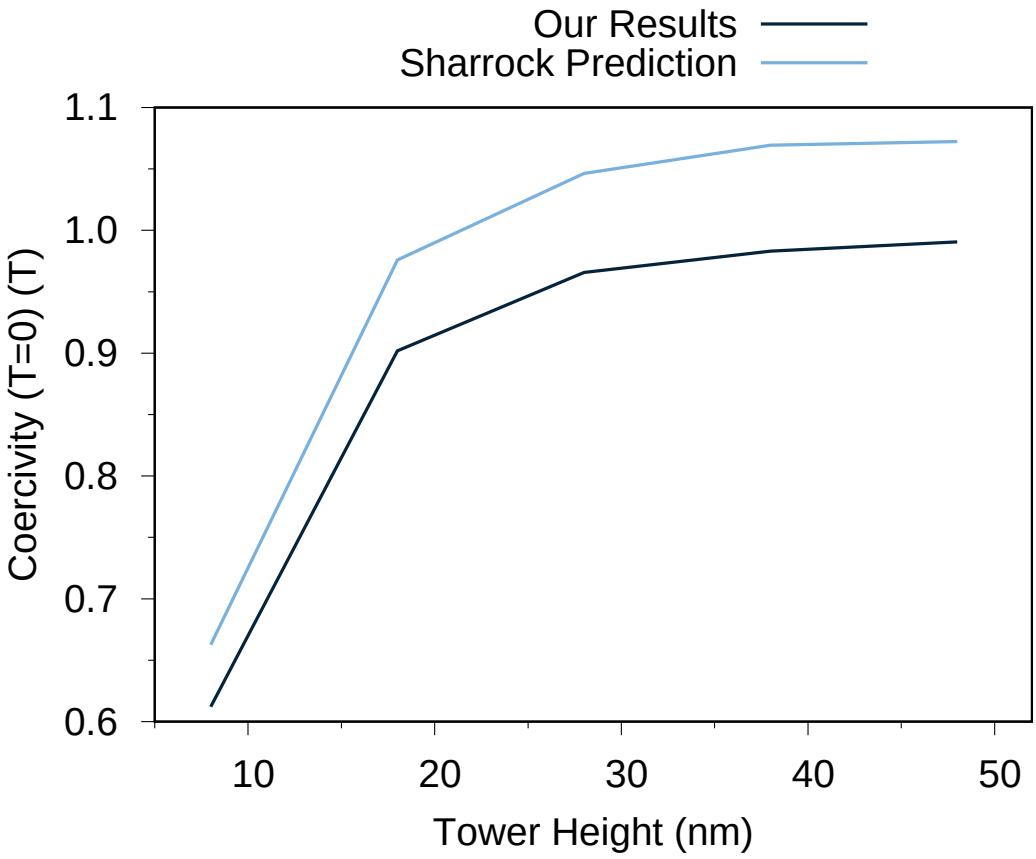

Fig. 3.12 Here we compare the extracted coercivities from the 0 Kelvin hysteresis loops to the Sharrock approximation. We see the trend is similar for the two lines but the extracted coercivities are lower for all height towers. The 8nm free layer is closest to the Sharrock approximation likely due to coherent rotation.

Sharrock fit aligns very strongly with the obtained data. There are very small fluctuations between the two models, but this is likely due to the simplicity of the Sharrock model, which assumes perfectly coherent rotation. The most significant deviation between the two models is the extracted value at 0 K, which is an obvious discrepancy in Figure 3.11. The uptick in H_c values at low temperature is due to H_c approaching H_a, leading to a small energy barrier (at the switching point) and the breakdown of the high energy barrier approximation used by Sharrock. This trend is identical for the other height towers in Figure 3.10.

This process is then repeated for the other free layer thicknesses from Figure 3.10 so the prediction for H_a from our model can be compared with that obtained from the Sharrock law. The results are shown in Figure 3.12.

There is good agreement in the trend between obtained results and the Sharrock model. For all free layer thicknesses, the Sharrock model predicts a slightly higher value for H_a than

is obtained from the atomistic calculations. This discrepancy is likely due to the simplified coherent rotation assumed in the Sharrock model. This suggestion is supported, as the 8 nm free layer displays coherent behaviour and has the closest agreement with the Sharrock model ($\Delta H_a^{8nm} = 0.05T$). All the thicker free layers display incoherent switching behaviour and have larger discrepancy, with the 18 nm having slightly larger ($\Delta H_a^{18nm} = 0.07T$) and the three thicker free layer having a greater discrepancy ($\Delta H_a^{28nm} = \Delta H_a^{38nm} = \Delta H_a^{48nm} = 0.08T$). While the 8 nm free layer displays coherent behaviour, it's small discrepancy with the Sharrock model is still expected. This is because the atomistic model includes edge effects and random thermal fluctuations which add complexity that is not captured by the Sharrock model. As a result of these features, even the coherent rotation is not as perfectly coherent, as individual spins may have slight resistance and fluctuation. This is unlike the Sharrock model, which assumes a perfect rotation of all spins during switching.

3.3.2 Approximating the Thermal Stability

The thermal stability factor, Δ, is a particularly important parameter in the design of reliable PSA-MRAM. It dictates the read/write error rate and the long term data retention rate, and is therefore of uttermost importance when describing switching performance. It is given by $\Delta = \frac{KV}{k_B T}$, where KV is the energy barrier, which is explored in more detail in chapter 5. For this section, however, an attempt to approximate the thermal stability factor is made. The expression for the thermal stability $\frac{KV}{k_B T}$, can be approximated using the Sharrock model using the so far unused parameter B. Additional attempts to calculate the thermal stability factor analytically are also added for comparison with the Sharrock model.

The first approach involves approximating $\frac{KV}{k_B T}$ using the Sharrock equation. From fitting Equation 3.7 to the atomistic data, a value for B was obtained, where $B = -\sqrt{\frac{k_B}{KV} ln(\tau f_0)}$. This can be rearranged to $\frac{KV}{k_B} = \frac{ln(\tau f_0)}{B^2}$. The thermal stability factor can therefore be re-written as

$$\Delta = \frac{ln(\tau f_0)}{B^2 T} \tag{3.8}$$

where B is obtained from the fit, T is the temperature, and an estimate must be found for the value of $ln(\tau f_0)$, as follows.

Since the estimation for $ln(\tau f_0)$ will be found using the Sharrock model, which assumes coherent rotation, the best estimate will come from the fit to the 8 nm free layer, since it is also coherent. Firstly, by differentiating Equation 3.6 with respect to $\sqrt{T}$, gets

$$\frac{dH_c}{d\sqrt{T}} = -H_a \sqrt{\frac{k_B}{KV} ln(\tau f_0)} = G \tag{3.9}$$

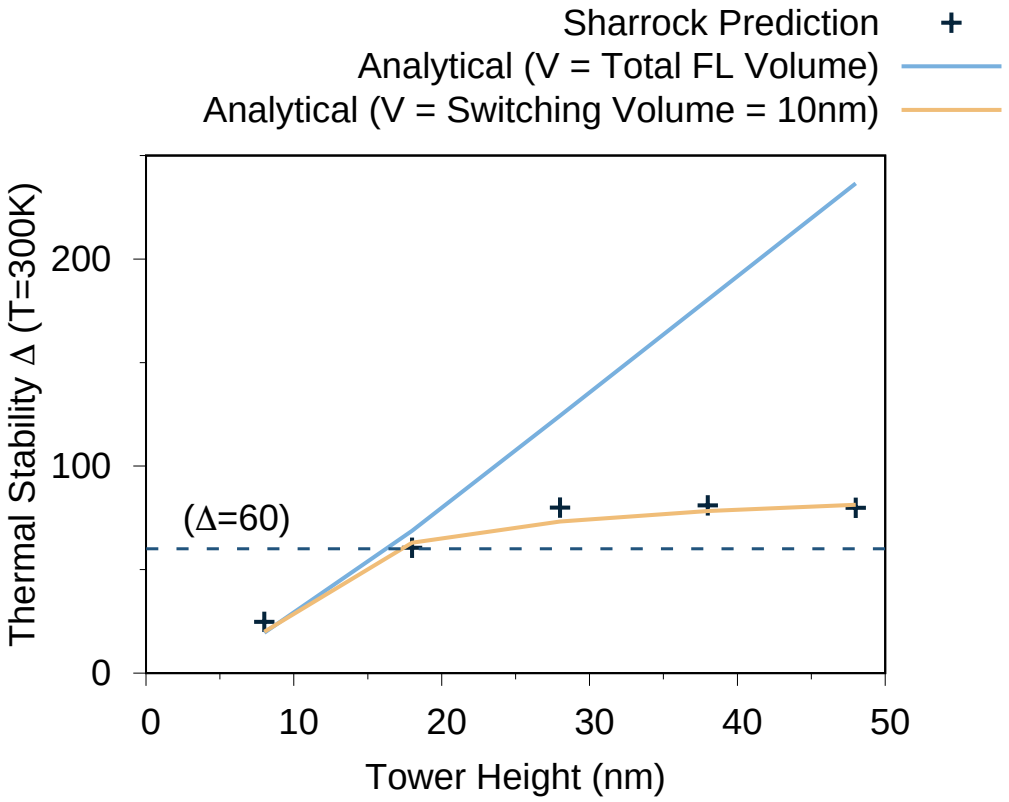

Fig. 3.13 Approximation of the thermal stability factor using the Sharrock model and an analytical approach for the different free layer thicknesses at 300 K. The expected decrease in stability as the thickness is decreased towards 8 nm due to the loss of shape anisotropy is observed, with the stability plateauing beyond 28 nm. This suggests nothing is gained in terms of stability for increased towers and represents a limit for towers of 5 nm diameter.

Where the term $G = \frac{dH_c}{d\sqrt{T}}$ has been introduced for easier notation. Replacing the macroscopic anisotropy $K = \frac{H_a M_s}{2}$ and rearranging Equation 3.9 produces an equation to estimate $ln(\tau f_0)$

$$ln(\tau f_0) = \frac{G^2}{H_a}\frac{M_s V}{2k_B} \tag{3.10}$$

The first fraction is known from the fit of Equation 3.7, as it is straightforward to show that $G = AB$ and $H_a = A$. The second fraction contains known constants in our model, $M_s = \frac{\mu_s n}{a^3} = 1.97 \times 10^6 A/m$, V is the volume of the free layer and k_B is the Boltzmann constant. From the fit to the coherent 8 nm free layer, which is the lowest fit in Figure 3.10, an estimate of $ln(\tau f_0) = 8.2251$ is obtained. With this value, an estimate for the thermal stability for the 8 nm free layer at 300 K can be found using Equation 3.8, which yields $\Delta = 24.7567$. The other height towers can then also be found using this estimate for $ln(\tau f_0))$ and is compared in Figure 3.13.

To compare with the Sharrock model, an analytical approach using $\Delta = \frac{KV}{k_B T}$ is also applied. The volume and the temperature are known, but K, the anisotropy energy, must be calculated separately. One approach is to use an expression for the shape anisotropy given in [50]

$$K = \frac{\mu_0 M_s^2}{2}(N_{xx} - N_{zz}) \tag{3.11}$$

Where $\mu_0 = 4\pi \times 10^{-7}$ is the permeability of free space, $M_s = 1.97 \times 10^6 A/m$, and $N_{xx/zz}$ are the demagnetisation factors shown in Table 3.1 of subsection 3.2.2. Using Equation 3.11, the value for K will plateau at around 30 nm as was seen for Table 3.1, and the values of k_B and $T(=300)$ are constant. For completeness, two interpretations for the volume, V are added to Figure 3.13 when calculating the thermal stability factor. One is the volume of the whole free layer, which grows linearly, resulting in an almost linear relationship (once the shape anisotropy has plateaued the volume is the only parameter changing). This is labelled as '$V =$ Total FL Volume'. This yields a very high thermal stability compared to the Sharrock prediction. However, this large discrepancy in the prediction is easily accounted for, as the analytical approach also assumes coherent rotation of the whole free layer. In actuality, the free layer reversal is is via nucleation and propagation which means that only the top of the free layer has to be switched. Comparing the thermal stability of the 48 nm free layer with the Sharrock estimate ($\Delta \approx 80$) gives an estimate of the height associated with the switching volume of $\frac{80}{240} \times 48 \approx 16$ nm. This is consistent with the rest of the results in this chapter that find that the switching becomes increasingly non-uniform for free layer thickness of between 8 nm -18 nm. A third comparison can therefore be added to Figure 3.13, using $\Delta = \frac{K_u V}{k_B T}$, but with a constant volume of $V = 16$ nm. This volume represents the volume associated with switching and shows strong agreement with the prediction of the Sharrock model.

The results in Figure 3.13 suggest that the 8 nm free layer would not satisfy the requirement for a thermal stability of $\Delta = 60$. The lack of shape anisotropy for such a small tower at these dimensions results in a loss of data retention due to thermal fluctuations. The 18 nm free layer is found to have a thermal stability $\Delta = 63.1$, just above the industry required threshold, while the taller towers are all similar at $\Delta \approx 80$. However, our approximation for $ln(f_0\tau)$ reflects the fast field sweep rate, which means that thermal effects are only observable in large fields around the coercivity. Long term stability requires zero-field simulations of the energy barrier, which are beyond the scope of this chapter, but the main purpose of chapter 5. For this reason, only the trends predicted in Figure 3.13 are discussed below.

The thermal stability is seen to plateau at around a 30 nm free layer thickness, suggesting that any growth above that in the z direction will not gain further stability and represents the maximum for towers of 5 nm diameter. The reduction in the thermal stability factor is

in agreement with the previous data of this chapter, suggesting a significant and non-linear reduction of shape anisotropy as the tower free layer thickness is reduced. The loss of shape anisotropy begins as the free layer is reduced to thickness below 30 nm, with a greater reduction as the thickness approaches the width. This is expected, since a free layer of 8 nm is only marginally above the 5 nm width. Previous studies have already shown that below this threshold, when the width becomes greater than the thickness, the shape anisotropy acts perpendicular to the interfacial anisotropy direction and MRAM ceases to be viable.

3.3.3 Approximation for the Frequency Factor f0

To estimate the thermal stability in the previous section, an estimate for $ln(\tau f_0) = 8.2251$ from the 8 nm free layer was obtained. It is sensible to calculate what this estimation yields for the value of f_0, given by $f_0 = \tau^{-1} e^{8.2251}$. This is complicated by the fact that the magnetisation is calculated in the atomistic model using a sweep rate process. Due to the rapid variation of the relaxation τ near to the coercive field, the effective time may be used, outlined by Chantrell et. al [121]. The effective time is given by

$$t_{eff} = \left(R\frac{KV}{k_B T}\right)^{-1} = \left(R\frac{H_a M_s V}{2k_B T}\right) \tag{3.12}$$

where R is the sweep rate, H_a is the anisotropy field extracted from our fit, M_s is the saturation magnetisation, and V is the volume of the free layer. For the hysteresis performed in this chapter, the sweep rate $R = 1 \times 10^8 T s^{-1}$ and $M_s = 1.97 \times 10^6 A m^{-1}$. With these values for t_{err}, Equation 3.10 is used to evaluate an estimate of f_0. The calculated values for f_0 for the free layer thicknesses are given in Table 3.2, along with the corresponding values for V and H_a. The values of f_0 are physically reasonable and also increase with tower height which is consistent with the expectation of the increase in f_0 with anisotropy predicted by the Brown relaxation time [122]. It should be noted that the estimate of the energy barrier from the Sharrock law can only give guidance. However, the plateau in the stability factor is most likely physically realistic on the basis that reversal begins with the nucleation of a small reversed region of magnetisation which is apparently at most weakly dependent on the tower height for values greater than 30 nm. A calculation of the exact energy barrier and its size and temperature dependence for the atomistic model is indicated, however this can only be done using the constrained Monte Carlo (CMC) method. This is the purpose of chapter 5 and is not a focus of this chapter, where only an approximation is made.

	Volume (m^3)	H_a (T)	f_0 (s^{-1})
8 nm	1.57×10^{-25}	0.663	9.24×10^{12}
18 nm	3.53×10^{-25}	0.976	3.06×10^{13}
28 nm	5.50×10^{-25}	1.046	5.11×10^{13}
38 nm	7.46×10^{-25}	1.069	7.09×10^{13}
48 nm	9.42×10^{-25}	1.073	8.97×10^{13}

Table 3.2 This table shows the calculated values for f_0.

3.4 Snapshots of Reversal

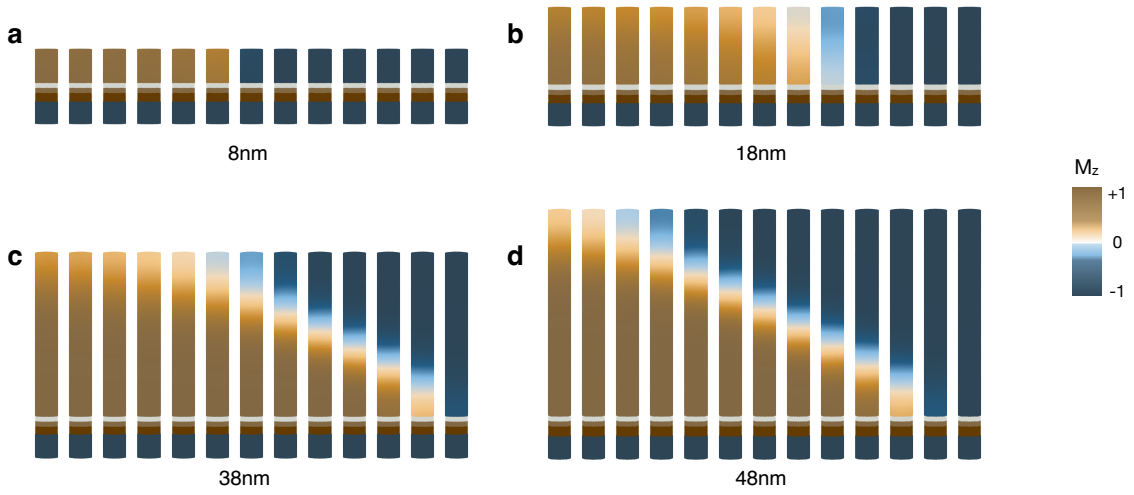

Fig. 3.14 Snapshots every $0.0001T$ of the switching mechanism at 0 Kelvin for different free layer thickness. We observe the smallest tower switching coherently, while all other towers demonstrate an incoherent mechanism, with an observable propagated domain wall motion.

While several results in this chapter have demonstrated behaviours suggestive of a change of reversal mechanism, it is useful to confirm with visual analysis. VAMPIRE can output snapshots containing the spin direction of each atomic site, which are then processed using POV-Ray [123]. Figure 3.14 and Figure 3.15 contain the snapshots of the reversal from aligned to anti-aligned at 0 K and 300 K respectively. The program was set to output snapshot at every field point, where the field increment for these images was $\Delta\mathbf{B} = 0.0001T$. Since the field increment is an order of magnitude smaller than the field increment used for the hysteresis loops, the number of time-steps at each increment is reduced by a factor 10. This means each snapshot in Figure 3.14 and Figure 3.15 represents a step in time of $10ps$.
Firstly, in Figure 3.14, the free layer is switched at 0 K. The smallest free layer is coherent, in

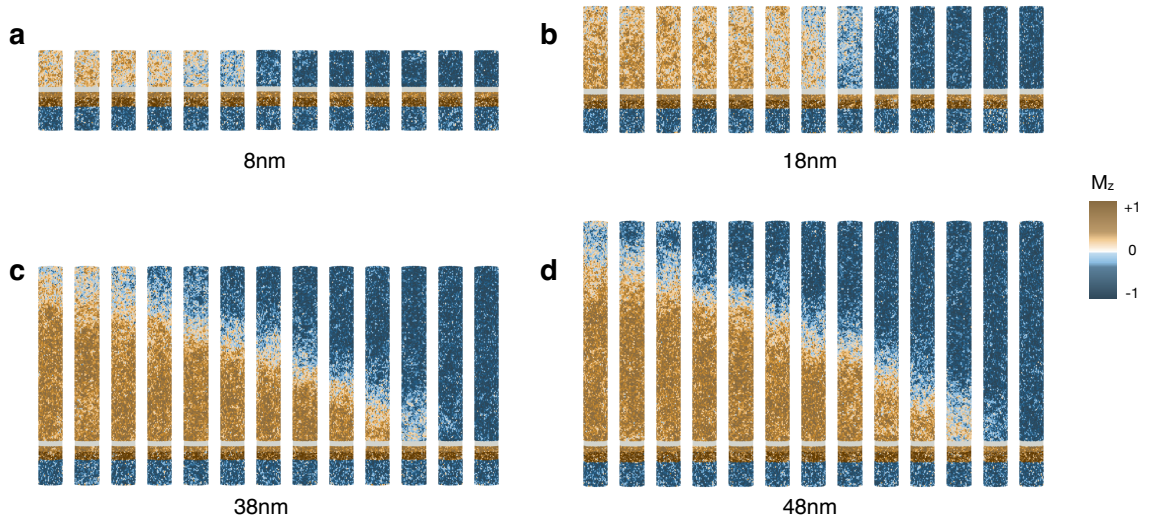

Fig. 3.15 Snapshots every 0.0001T of the switching mechanism at 300 Kelvin for different free layer thickness. We observe the coherrent and incoherrent mechanisms seen in fig. 3.14, but with thermal fluctuations throughout the stack. We see a partially thermally driven propogated domain wall for the taller towers.

agreement with the previous results in this chapter. All taller towers demonstrate incoherent rotation, switching via a propagated domain wall. A benefit of performing these snapshots at 0 K is the absence of thermal fluctuations provides a clear domain wall propagation. The 28 nm free layer was only omitted to keep the figure symmetric and easy to view, as it provided no further discussion. In an externally applied field such as this setup, the propagation starts at the top of the stack, moving downwards. This is because the bottom of the stack is subjected to the enhanced exchange constant and anisotropy, arising from the contact with the MgO. As a result, the bottom of the free layer is slightly more stable than the top of the free layer. This is the opposite way around to the usual STT setup, whereby the current crosses the MgO into the bottom of the free layer, thus rotation starts at the bottom. However, this difference does not invalidate the conclusion that a change of switching mechanism occurs when the free layer is reduced to sub 10 nm thickness. Expecting a propagated domain wall in taller free layers is useful in the further studies conducted in chapter 4 and chapter 5.
Secondly, in Figure 3.15, the free layer is switched at 300 K. The change in switching mechanism observed in Figure 3.14 is still easy to see at 300 K. Unlike Figure 3.14 however, the propagated domain wall appears to be partially thermally driven at 300 K. Since each snapshot in both figures is separated by the same field increment (or time increment) a direct comparison between demonstrates the thermally driven initial steps. The free layers are partially in transition (deviating from the dark brown colour) for more field increments than

in the 0 K case. This comparison is useful for two reasons. Firstly, it is not necessarily obvious that the 8 nm free layer would maintain coherent rotation at room temperature. While the rotation of the 8 nm free layer appears to take longer, since it is thermally driven initially, there is no evidence of a domain wall movement. Secondly, the importance of the thermal driving of the switching mechanism is highlighted for future studies.

3.5 Summary

In this chapter, a systematic investigation of the effects of temperature and free layer volume on the switching mechanism of 5 nm diameter PSA-MRAM. Since this was an atomistic spin model, thermal fluctuations and the long range dipole field are included to capture these effects. It was found that the taller free layers contain non-uniform exchange modes throughout the stack, leading to non-coherent rotation. Only the smallest free layer in this study, at 8 nm tall, showed coherent behaviour. This was supported by snapshots of the reversal mechanism both with and without thermal fluctuations. Particularly important for future studies, is the significant thermal nucleation of the switching mechanism in such thin tower structures. The incoherrent rotation with partially thermally driven reversal results in a lower coercivity, so future design must account for this. The dipole field emerging from other layers in the stack also causes a small shift of the free layer hysteresis loop. As a result, there is a small bias towards being aligned with the reference layer that should be considered in future work. Finally, a comparison with the Sharrock model showed good agreement, particularly for the coherent free layer. This led to an approximation of the thermal stability as a function of free layer thickness. Futher study using the constrained Monte Carlo may provide an improved estimate for the values of the thermal stability, but this chapter demonstrated the expected trend. Most interestingly, the taller free layer had reached an asymptotic maximum, meaning nothing is gained from engineering even taller free layers. This is particularly useful for future PSA-MRAM design, as it imposes a limitation. As the free layer is reduced below around 30 nm, the thermal stability rapidly decreases, where our estimated numbers suggest that below around 18 nm, the thermal stability drops below the industry required minimum.

4

Dynamics of STT-PSA-MRAM

PSA-MRAM devices will use a spin transfer torque (STT) mechanism to switch the free layer. The electron spins of a spin-polarised current entering the free layer will transfer torque to the atomic sites in the free layer, causing reversal. The switching properties of the free layer subjected to this reversal mechanism will therefore depend on the mechanics of the free electron spins through the stack. It is essential to the development of STT-PSA-MRAM that these behaviours are understood, both for more efficient design and for long term reliability to consumers. Independent of the STT electrons, in chapter 3, it is also clear that the the switching properties of the free layer depend on the finite temperature and the shape of the stack. The actual behaviours displayed in a nanoscale free layer undergoing STT reversal at room temperature is therefore an intricate and currently unknown phenomena [124]. Much of the previous study into STT-MRAM has been using micromagnetic models, but these approaches have limited applicability here. Due to the discretising nature, they do not capture the continuous motion of the STT electron spins, the finite temperature effects or the effects of the dipole field from the shape and dimensions of PSA-MRAM system. To understand the intricate properties and behaviours of STT-PSA-MRAM, an atomistic approach is required. At present, there have been few atomistic studies on STT-MRAM to capture these effects, and the inclusion of STT into the VAMPIRE software package was relatively recent ($\approx$ 2018). So far, the previous atomistic studies on STT-MRAM have not involved the PSA present in the tall cylindrical towers of this thesis. As these PSA-MRAM structures are a strong candidate for competing density MRAM, an atomistic study involving the STT mechanism is beneficial. This chapter focuses on the switching dynamics of PSA-MRAM using an STT mechanism to drive reversal.

4.1 STT Parameters

The formalism for modelling the STT mechanism in VAMPIRE was outlined in chapter 2 and requires several material dependent parameters. Parameterising a CoFeB-MgO-CoFeB stack is straightforward since previous studies have already found the required values. The parameters for the CoPt layers are less documented and had to be estimated. It is worth noting that the magnetic parameters outlined in Table 2.1 are still present for all simulations in this chapter, since STT is implemented and solved independently to the magnetisation evolution in the code.

The STT parameters used for the CoFeB-MgO-CoFeB MTJ are shown in Table 4.1 and are the same as those used in other VAMPIRE studies [49, 125, 76, 77, 82]. There are three important length scales to consider when parameterising a material in this STT model, the spin diffusion length λ_{SDL}, the spin flip length λ_{SF} and the spin precession length λ_J.

The spin flip length is the characteristic length scale over which the conduction electron spins relax and is given by $\lambda_{SF} = \sqrt{2D_0\tau_{SF}}$. The diffusion constant of a typical metal is $D_0 = 10^{-3}$, while the spin flip relaxation time of the conduction electron spins for ferromagnetic materials is $\tau_{SF} = 1$ ps [78].

The spin precession length is the length scale over which the spin-polarised electrons may interact with the local spin moments of the lattice and is given by $\lambda_J = \sqrt{2\bar{h}D_0/J_{SD}}$. The exchange coupling J_{SD} between the spin-polarised electrons and the local magnetisation is between $0.1 - 0.4eV$ and can be obtained from conduction electron resonance [126]. A J_{SD} of $0.1eV$ is used for CoFeB, and the spin precession length is $\approx 3nm$ [125].

The spin diffusion length can be obtained directly from analysing FMR spectra and is found to be $12nm$ for CoFeB [127]. The spin diffusion length is also given by $\lambda_{SDL} = \sqrt{1-\beta\beta'}\lambda_{SF}$. Both of the parameters β and β' as well as the equilibrium spin accumulation m_∞ can then be obtained from density of states calculations [128].

STT parameters	CoFeB	MgO	Units
λ_{SDL}	12.0	12.0	nm
D_0	0.001	0.001	m^2s^{-1}
β	0.56	0.56	
β'	0.72	0.72	
m_∞	2.62×10^8	2.62×10^8	Cm^{-3}
J_{SD}	1.6×10^{-20}	1.6×10^{-20}	J

Table 4.1 The parameters required to simulate the STT mechanism through CoFeB and MgO materials in VAMPIRE.

4.1.1 The CoPt Layers

Since these STT parameters are material dependent, values had to be found for CoPt alloys. These values are presented in Table 4.2. The spin diffusion length was found from spin pumping experiments to be $\approx= 14nm$, where Platinum alone is found to be much smaller at $\approx= 3nm - 7nm$ and Cobalt alone is found to be much higher at $\approx 60nm$ [129, 130]. The diffusion constant, D_0, was found to be smaller than that of CoFeB, with a value of $D_0 = 2 \times 10^{-4} m^2 s^{-1}$ [131]. The s-d exchange interaction is found to be the same at that for CoFeB, so the J_{SD} constant is the same, representing 1 eV [126].
The value for β was found experimentally for CoPt alloys to be 0.48 and for simplicity this study has taken $\beta = \beta'$. This is not perfect, as generally $\beta \neq \beta'$ when the DOS for spin-up is not equal to spin-down, however, these values do not affect the results significantly. The spin accumulation and subsequent impact on reversal and incubation times were completely unaffected by changing the value of β' for the CoPt layers by $\pm 20\%$. Given the difficulty of finding relevant studies on CoPt alloys this approximation has stuck. For context, the vast majority of studies on the relevant parameters consider a Co layer in contact with a Pt layer, and not a CoPt alloy.
Finally, the equilibrium value of the spin accumulation, m_∞, is found from the majority and minority spin populations from DOS calculations ($\propto N^\uparrow - N^\downarrow$). The density of states can be found from first principle density functional theory calculations [132, 133]. The equilibrium value is then be given at the Fermi energy by $m_\infty = \frac{[DOS\uparrow(E_F) - DOS\downarrow(E_F)]k_B Te}{V}$ where k_B is the Boltzmann constant, T is the temperature, e is the charge of an electron and V is the lattice volume [134].

STT parameters	CoPt	Units
λ_{SDL}	14.0	nm
D_0	0.0002	$m^2 s^{-1}$
β	0.48	
β'	0.48	
m_∞	1.0×10^8	Cm^{-3}
J_{SD}	1.6×10^{-20}	J

Table 4.2 The parameters required to simulate the STT mechanism through the CoPt layers.

4.2 Switching Dynamics At 0 Kelvin

In this section, reversal using a STT mechanism at 0 K is documented. Thermal fluctuations add additional complexity to the magnetic behaviours, which will be addressed in the next section. It is useful, therefore, to use the 0 K simulations as a benchmark to observe the impact of current density and free layer volume on the switching characteristic of PSA-MRAM. It is worth appreciating at this stage how reversal under a STT mechanism differs from that seen in chapter 3, which used an external field. The external field was applied uniformly to the entire stack, so the nucleation point for reversal is determined by the anisotropy profile. The bottom of the free layer, which is in contact with the MgO, has enhanced anisotropy and exchange, as outlined in subsection 2.4.3. It is also subjected to a small stray field emanating from the lower layers of the stack. For this reason, the point of nucleation was found to be from the top of the stack, with a propagated domain wall if the free layer was large enough. In contrast, the point of nucleation for STT driven reversal will be from the bottom of the stack, since the injected current will tunnel across the MgO into the bottom of the stack. The current will exert torque on the lower layers of the free layer as the electron spins cross the MgO barrier. If the current density is large enough, the nucleation will therefore be from the bottom. This section will systematically explore the impact of a range of current densities and free layer thickness on the performance of PSA-STT-MRAM.

4.2.1 Switching and Incubation Time

One of the most important parameters to determine for functional STT-MRAM is the switching time. As a performance characteristic, the switching time could be defined as the total time from the moment the spin polarised current is inbound to the moment the free layer has completed rotation. However, this definition includes two distinct considerations for design, the incubation time and the reversal time. The incubation time occurs first and is the time before any rotation of the free layer occurs. This is the time required to initialise the switching, while a spin accumulation is built, and will intuitively depend on the applied current. This will additionally depend on the efficiency of the reference layer to create a polarised current. The reversal time is thus the time after initialisation, whereby the rotation of the free layer is underway. The reversal time is therefore characterised by the shape anisotropy, the intrinsic damping and the temperature of the free layer in addition to the current density. Dividing the total switching time into these two components is beneficial for two main reasons. Firstly, it allows comparison of the results to other studies that have made similar decisions. Comparison of the incubation and reversal time are key to outlining

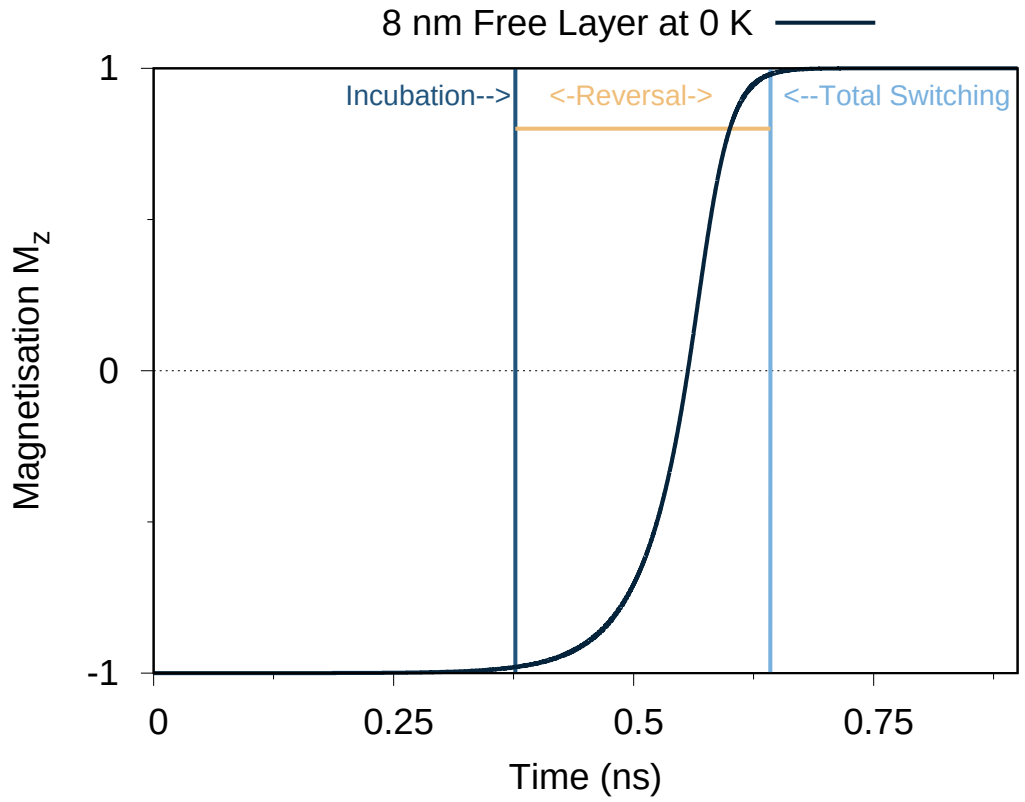

Fig. 4.1 This figure demonstrates the two components of the total switching time. During the incubation time, no rotation of the free layer has occurred, but the current is building a spin accumulation. The reversal time is when the magnetisation of the free layer is rotating. The total switching time is the sum of the two.

the validty of the PSA-MRAM design compared to other MRAM designs. Secondly, it provides a more complete and in depth discussion of the physical behaviours emergent in the STT-PSA-MRAM designs, which are currently lacking in literature. A graphic description of the incubation, reversal and total switching time is shown in Figure 4.1, for clarity.

There were two candidate approaches to the extraction of the switching and incubation times from the STT data. The first approach is the most simple, and utilises a simple python script to find the part of the graph where the z-component of the magnetisation begins and ends switching. The second approach involved fitting a function to the data, which is a similar approach to that used for extracting the coercivity and switching field distribution in subsection 3.2.3. Both of these methods are now discussed.

Firstly, outlining the simple python script approach. To find the incubation time, the point where the z-component of the magnetisation decreases by more than 2% is found using a trivially simple python script. Similarly, to find the end of the reversal time, the point where 98% of the z-component of the magnetisation has reversed is found in the same python script.

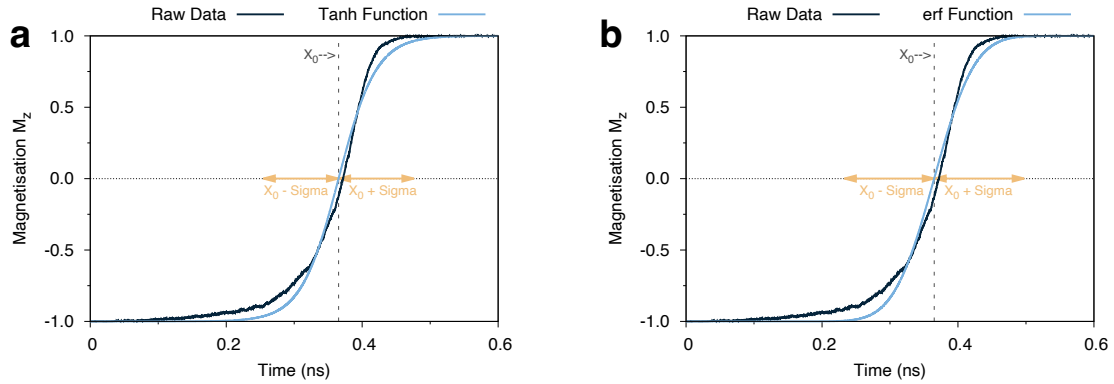

Fig. 4.2 This figure shows the fitting of the a) Tanh function and b) error function to the STT curve of the 8 nm free layer subjected to $1 \times 10^{12} A/m^2$ at 0 Kelvin. In this case, σ was assumed symmetrical. The plot is a poor fit, with a significant difference between the extracted X_0 and the actual crossing point of the raw data. The curvature of the raw data is also not a very good fit, suggesting the estimation for σ is also inadequate.

This method was used to place the vertical lines, indicating incubation and total switching time, on Figure 4.1. During the incubation time, while a spin accumulation is developing, very small fluctuations occur in the free layer due to stray fields. For this reason, the 2% change was employed. This is also good practice for the inclusion of temperature, where thermal fluctuations will cause small variation from a perfectly saturated free layer before reversal occurs. The total switching time is then the time when 98% of the z-component is reversed, which is the second time extracted by the python script, for the same reason. The reversal time is then the total switching time minus the incubation time. This approach requires minimal user input and is simple to implement. However, this approach will only provide a number for the incubation, reversal and total switching times, with no insight offered to what may be occurring during the reversal process. This is a potential drawback from the second method discussed below, which provides some insight into the symmetry of the reversal mechanism. Additionally, fluctuations in the magnetisation of much larger than 2% were soon found, even in the absence of temperature. Once these fluctuations become around 10% or even larger, this simpler method becomes completely invalid, since it will always find the first instance that the magnetisation reaches 10%.

Much like the hysteresis curves presented in chapter 3 from an applied field, the reversal of the magnetisation from a STT mechanism follows a characteristic curved shape. It is possible, therefore, to fit a graph of the same characteristic shape. This is the idea for the second approach to extraction. Two such functions are trialed, one with the form of an error function and one with a tanh form. In both these cases, the function must be translated to the right by some amount X_0 and stretched by some scale factor σ. The trial functions are

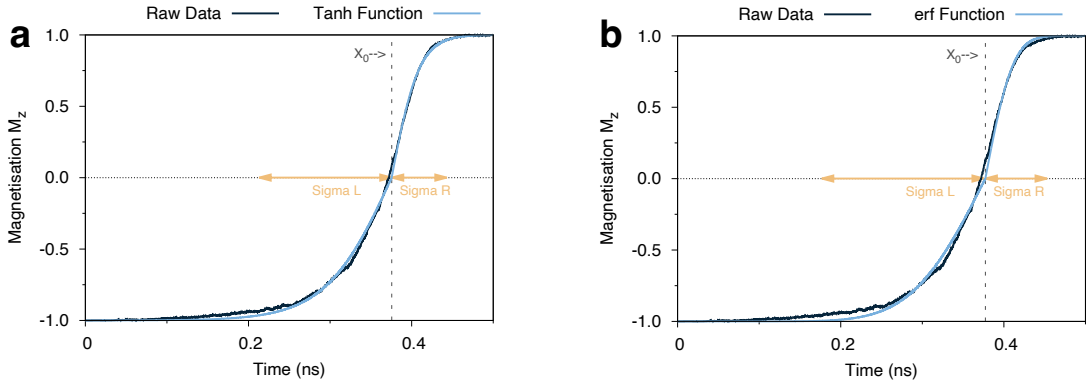

Fig. 4.3 This figure shows the fitting of the a) Tanh function and b) error function to the STT curve of the 8 nm free layer subjected to $1 \times 10^{12} A/m^2$ at 0 Kelvin. Unlike Figure 4.2, sigma is not assumed to be symmetric about X_0, presenting a much better fitting to the raw data. The tanh function appears closest to extracting X_0, with both functions plotting the latter half of the graph well.

therefore

$$\begin{aligned} &erf(\frac{x-X_0}{\sigma}), \\ &tanh(\frac{x-X_0}{\sigma}) \end{aligned} \tag{4.1}$$

where X_0 and σ are found via optimisation of fitting. With this fitting technique, the extracted value of X_0 would be where the graph crosses the x-axis and the value of σ would be the width of the curve from the extreme magnetisation ($M_z = \pm 1$) to neutral ($M_z = 0$) during the switching process. Initially, both of the functions are fit to the whole data set with a rough estimate for X_0 and σ obtained by eye as the initial input, and then optimised in gnuplot. This assumes the switching time from $M_z = -1$ to $M_z = 0$ is symmetric with the time from $M_z = 0$ to $M_z = 1$, since only one value for σ is obtained.

The results are shown in Figure 4.2 for the STT curve of the 8 nm free layer subjected to a current density of $1 \times 10^{12} A/m^2$ at 0 K. The discussion of the results are found in the next section and this graph is only meant for demonstration purposes. Clearly, the assumption that σ is symmetrical leads to a very poor fitting for both the tanh and the error function. In both cases, the extracted value for X_0 is noticeably differed from that of the raw data. Furthermore, the curvature as the magnetisation reaches saturation ($M_z = \pm 1$) is significantly different between the raw data and the function fitting. Neither the tanh nor the error function significantly outperform the other, both are inadequate.

The natural improvement to this problem, is to have anti-symmetric values for σ for the

left and right of X_0. This is shown in Figure 4.3 for both functions for the same conditions as Figure 4.1 (8 nm FL and a current density of 1×10^{12} Am^{-2} at 0 Kelvin). First, a full fitting to the curve will obtain a value for X_0 (along with the symmetric value for σ that is rejected). Once X_0 is determined, two more independent fitting optimisations are performed. First for the range $0 \leq t \leq X_0$ to obtain a left side σ_L, then separately for $t \geq X_0$ to get the right side σ_R. This produces a much improved fit when compared to Figure 4.1, where tanh consistently provides a slightly better fit. The difference in the incubation, reversal and total switching time extracted from the tanh function compared to the error function is $\Delta t < 10^{-3}s$ across all current densities and temperatures. Since this is lower than thermal noise, it largely didn't matter which function was chosen, as long as the anti-symmetric method is used. tanh is utilised for the rest of this chapter when extracting relevant times.
Once a value for σ_L, σ_R and X_0 have been found, obtaining the values for incubation, reversal and total switching time follows the same process as the simple python script. The incubation time is defined up until the magnetisation has increased to -0.98, and the reversal time is from that moment until the magnetisation reaches 0.98. These points can be obtained exactly from the tanh functions, and unlike the simple python script are unaffected by fluctuations in the raw data, since the fitted tanh is a smooth plot. When the magnetisation reaches -0.98, the time will be given by $x = \sigma_L \times \tanh^{-1}(-0.98) + X_0$. Similarly, the total switching time occurs when the magnetisation reaches 0.98 which is a time of $x = \sigma_R \times \tanh^{-1}(0.98) + X_0$. The reversal time is then the difference between these values.

4.2.2 Results

Initially, the trends and properties of spin transfer torque is studied in the absence of thermal fluctuations. In this case, the free layers initial magnetisation direction is tilted at an angle of 1° from the easy axis to allow for a minimum torque. The free layer is initialised with its magnetisation direction along the -z direction, the opposite direction to the reference layer. Each time-step in these simulations is 1×10^{-16} s using the LLG equation outlined in chapter 2. Each run consists of $50,000,000$ total time steps, so represents 5 ns of real time. This length of time was a compromise on a reasonable amount of comparable data for the tallest tower and appropriate computation resources. Using the University of York's HPC facilities, the tallest free layer in this study takes just under two days to complete a model of 5 ns STT switching. Longer timescales were possible by utilising the longer queue times available on the HPC cluster, however this is not appropriate due to how many independent simulations were required to span a reasonable range of current densities.
The evolution of the free layers magnetisation components against time present an initial insight into the behaviours of the free layer during STT driven reversal. To uncover trends, a

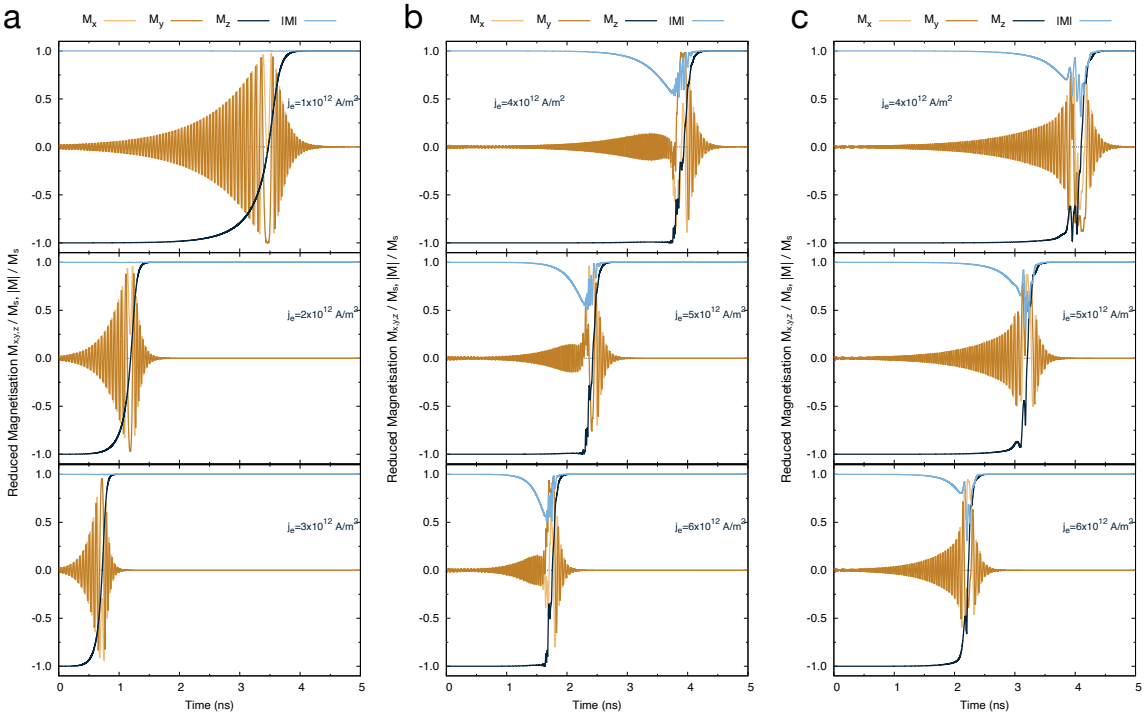

Fig. 4.4 The magnetisation of the free layer against time for a) the 8 nm free layer at $1(2)(3) \times 10^{12}$ Am^{-2}, b) the 18 nm free layer at $4(5)(6) \times 10^{12}$ Am^{-2}, and c) the 48 nm free layer at $4(5)(6) \times 10^{12}$ Am^{-2}.

range of current densities and free layer thicknesses were compiled together in Figure 4.4. This consists of nine graphs in three columns, where column (a) is the smallest free layer (8 nm thick), column (b) is the second smallest free layer (18 nm) and column (c) is the tallest free layer (48 nm). Proceeding down each column, the current density increases in steps of 1×10^{12} Am^{-2} as labeled on each plot. These free layer dimensions were chosen as they present three unique reversal behaviours that will continue to be explored in this section. The free layer thicknesses that are omitted at this stage (28 nm and 38 nm thick free layer) display the same characteristics as the 48 nm free layer.

Firstly, column (a) of Figure 4.4 shows the evolution of the magnetisation for the 8 nm free layer at $1(2)(3) \times 10^{12}$ Am^{-2}. The lowest current density capable of initiating reversal in under 5 ns at 0 K at these dimensions was 1×10^{12} Am^{-12}. This is the reason for this choice of lower current density. Spanning a small range of current densities is to observe trends, at the lower end of current densities, where the increasing magnitude has the most effect on the reversal times.

The magnetisation length, $|M|$, does not fluctuate at any of the presented current densities,

suggesting a coherent rotation of the free layer. This is in agreement with the results presented in chapter 3 studying the reversal mechanisms in a field [116]. It is still a worthwhile result, however, to compare the STT reversal mechanism to the external field. At increasing current densities, it is worth noting that the reversal mechanism is unchanged in the coherent case. Similarly, the magnetisation $M_{x,y,z}$ follows the expected characteristic shape of coherent rotation even at increased current densities, suggesting the STT doesn't force an alternate reversal mechanism in the 8 nm free layer.

Specifically, the M_z curve does not fluctuate during reversal, instead presenting a smooth transition. This indicates coherent reversal only in tandem with the $|M|$ plot, as a linearly propagated domain wall would also produce a smooth curve M_z. The out of plane components, M_x and M_y, show a growing precession of the spins leading up to reversal, before rapidly damping following reversal. As the increasing spin accumulation exerts torque on the atomic spins, they will begin to precess, eventually inducing precession over the energy barrier. This explain the anti-symmetry in precession either side of the reversal process.

Additionally, it is beneficial to see the speedup in the reversal as the current density is increased. By eye, the total reversal when subjected to a current density of 1×10^{12} Am^{-2} takes ≈ 4 ns. Doubling the current density to 2×10^{12} Am^{-2} reduces the total reversal time to ≈ 1.5 ns. To explore this further, switching times and reversal times are discussed in subsequent plots. However, this preliminary insight suggests that once a sufficient current density has been achieved, a small increase may yield significant improvement in performance. This is essential for functioning PSA-MRAM, whereby a compromise of fast reversal and low energy requirements are essential.

The next tallest tower in this study has an 18 nm thick free layer and the evolution of the magnetisation is presented at current densities of $4(5)(6) \times 10^{12}$ Am^{-2} in Figure 4.4 (b). The current densities in this figure are larger than those just discussed in Figure 4.4 (a). The reason for this, is that a minimum current density of 3.5×10^{12} Am^{-2} was required to initiate reversal in under 5 ns. In addition, this tower displays evidence of incoherent reversal, so a direct comparison between this and the 48 nm free layer is useful. The 48 nm free layer requires a minimum current density of 4×10^{12} Am^{-2}, only slightly above the 18 nm, so it is appropriate to use the same range.

The most significant difference between the 18 nm free layer and the 8 nm free layer is the reduction and recovery in the magnetisation length $|M|$ around reversal times. This suggests a shift from a coherent rotation and served as the motivation for this towers inclusion. However, this precession is relatively small, reaching only as low as around $|M|/M_s = 0.75$ at the largest current density. It is not clear from this data alone what the reversal mechanism may look like, which provides motivation for snapshots of the reversal process presented

in subsequent figures of this section. This is, however, evidence that a more complicated reversal mechanism is present that is distinctly not coherent.

Further, the M_z component is noticeably not a smooth curve, unlike the 8 nm free layer in Figure 4.4 (a), with rapid fluctuations during the initial reversal. If the reversal in the 18 nm free layer was a simple domain wall propagating through the stack, the M_z of the whole free layer would smoothly transition as the domain wall moves through the stack. These rapid fluctuations in M_z are therefore evidence of precession in the magnetisation of atomic sites independent of a domain wall motion. This also highlights the importance of a section simulated in the absence of thermal fluctuations. With the inclusion of thermal noise, fluctuations in M_z are expected, and this result may not arouse suspicion. In contrast, observing these precessions at 0 K suggests that the STT mechanism is responsible for these behaviours and merits further exploration. The reversal mechanism is not a simple propagated domain wall.

Finally, Figure 4.4 (c) shows the evolution of the magnetisation from the 48 nm free layer at $4(5)(6) \times 10^{12}$ Am^{-2}. These dimension also suggest incoherent reversal, but are noticeably different to the 18 nm so are worth presenting. Firstly it is worth reiterating, that the precession in the magnetisation length, $|M|$, is initial evidence of incoherent rotation. Comparison to the 18 nm free layer in Figure 4.4 (b) shows the precession in $|M|$ is much larger at each current density. Though it still does not reach $|M|/M_s = 0$, it suggests that this free layer is much closer to a simple propagated domain wall, and the complicated precessional motion present in the 18 nm free layer are at least reduced at greater dimensions. Again, it is not obvious from these figures what the complications in the reversal mechanism may be and snapshots of the reversal process are required.

A second interesting change between the plots in Figure 4.4 (c) and Figure 4.4 (b) is the nature of the precession in M_z at the start of the reversal. In the case of a 48 nm free layer, these precessions are much larger in magnitude and there are fewer of them, before reversal. As the current density increases, these begin to vanish, with only one small flick in the M_z at a current density of 6×10^{12} Am^{-2}. In contrast, the 18 nm free layer had rapid precessional motion and many of them, but smaller in magnitude. They do also begin to vanish as the current density increases, but are still present at 6×10^{12} Am^{-2}. Since these results are at the same temperature and current density, this reversal behaviour would seem to be dependent on the shape anisotropy of the free layer. This behaviour has less of an impact at greater shape anisotropy. It is an indication that while the taller towers are all incoherent reversal, there is a transition in precise reversal behaviours. The 28 nm and 38 nm free layers show the same large discontinuities as the 48 nm free layer at 0 K.

These results are potentially important considerations for design of STT-PSA-MRAM. It

is already an industry consideration that the current density used in MRAM devices must be a compromise of energy usage and performance. Too large a current can cause damage, as well as negating the benefits of a non-volatile technology. Too small a current and the performance will be unsatisfactory. These results show that, in addition to these well known considerations, the current density directly impacts the reversal mechanism and subsequently performance. As the current density is increased, something closer to a propagated domain wall motion is observed, while complications occur at lower current density.

While the evolution of the magnetisation in time is useful for initial insight into the dynamics for the STT mechanism, an analysis of the switching times will provide insight into the performance characteristics. The effect of spin currently density on the switching times for different free layer thicknesses was therefore systematically studied at 0 K. The total switching time is split into the incubation time and the reversal time as discussed in subsection 4.2.1 for improved insight into the trends and underlying physics. It is worth reiterating that due to computational constraints, the results presented are only for free layers reversal in under 5 ns total switching time. Thus, if the current density is not sufficient to switch a given free layer in under 5 ns it is omitted.

First, the incubation time as a function of current density is presented in Figure 4.5 for the different free layer thicknesses. During the incubation time, the spin polarised current from the reference layer will tunnel across the MgO and a spin accumulation is built up in the free layer. These initial dynamics will be slow due to a low torque before the spin accumulation has had time to build up. Eventually, this spin accumulation will be sufficient to initiate reversal in the free layer, which is the end of the incubation time. An initial observation in Figure 4.5 is that the lowest current density capable of initiating reversal decreases as the free layer thickness decreases. The 8 nm free layer requires a minimum current density of 1×10^{12} Am^{-2} to initiate reversal, while the 18 nm free layer requires 3.5×10^{12} Am^{-2}, the 28 nm requires 4×10^{12} Am^{-2} and the tallest two towers both require 4.5×10^{12} Am^{-2}. This is a consequence of the shape anisotropy of the free layer. A higher current density will produce an increased spin accumulation at a faster rate, and this must provide a sufficient torque to overcome the shape anisotropy. Since the taller free layers have greater shape anisotropy, they will require a larger spin accumulation, and therefore a larger spin current density, to initiate reversal.

A second observation, is that all height towers follow the same trend after the initial reversal. This trend is characterised with a rapid initial reduction in incubation time with increasing current density, eventually beginning to flatten out as a minimum incubation time is approached. It was already clear in column a) of Figure 4.4 that the initial reduction in incubation time for the 8 nm free layer is roughly halved when the current density doubles

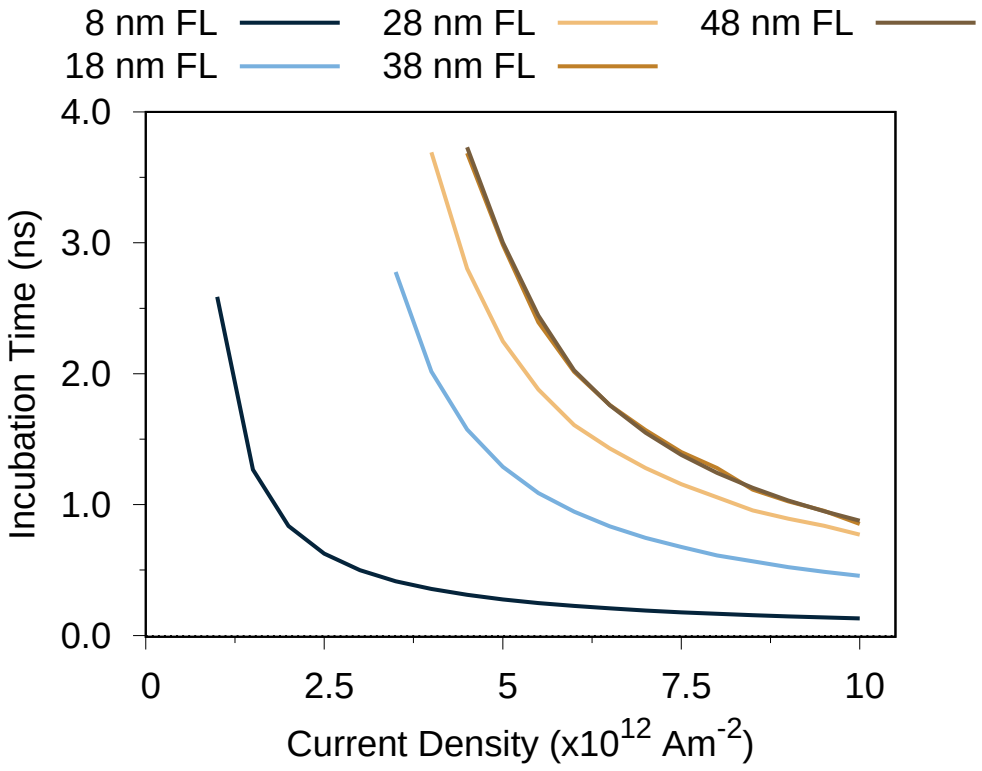

Fig. 4.5 Incubation times as a function of the current density for the different free layer thicknesses. As the free layer thickness is increased a larger current density is required to initialise and the incubation times are longer. This is due to the increased shape anisotropy, which plateaus for the tallest towers. Increasing current density reduces incubation time towards a minimum for the given shape anisotropy.

from 1×10^{12} Am^{-2} to 2×10^{12} Am^{-2}. It is useful to plot the full range of current densities in Figure 4.5 as it further shows that at a current density of around 3.5×10^{12} Am^{-2}, the subsequent decrease in incubation time is $< 10\%$ for each increase of 0.5×10^{12} Am^{-2}. The other free layers follow similar trends, where increasing the current density provides a significant boost to the incubation time initially. Subsequently, when the current density has increased by around 3×10^{12} Am^{-2} from it's minimum current density, the subsequent gains in incubation time fall to $< 10\%$.

Finally, at any current density larger than 4.5×10^{12} Am^{-2}, all of the free layers studied here are able to switch. This allows direct comparison of the thickness of the free layer as a function of current density. At all subsequent current densities, the increase in free layer thickness leads to an increase in incubation time, up to the tallest two which are almost perfectly overlapping. This is also explained with the increasing shape anisotropy, since a larger spin accumulation is required to overcome the larger shape anisotropy of the taller free

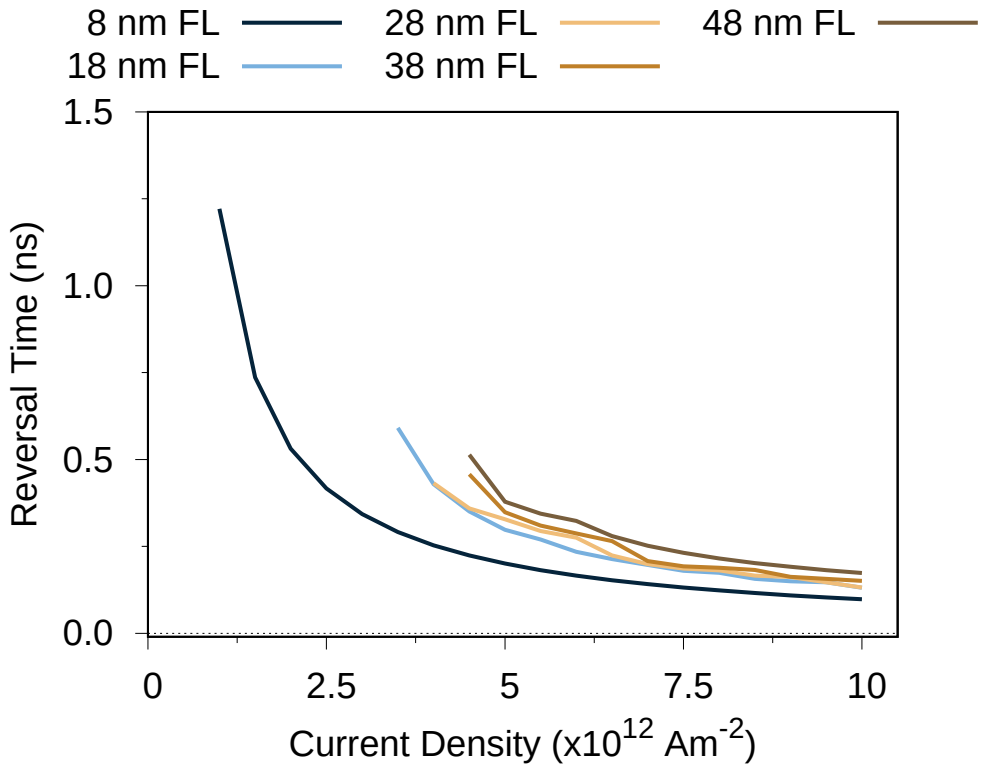

Fig. 4.6 Reversal times as a function of the current density for the different free layer thicknesses. As the current density increases the reversal time decreases. The smallest tower is fastest since it is coherent, while the taller towers are slower and display evidence of incoherent rotation.

layers. At any given spin current density, it will therefore take longer to build the appropriate spin accumulation. This is in good agreement with the trends found in chapter 3 where the tallest two free layers were shown to have reached an asymptotic maximum while the 28 nm free layer is only slightly behind.

The second component of the total switching time is the reversal time, which is shown as a function of current density in Figure 4.6. The reversal time is the time taken from the start of the M_z reversal until the whole free layer has rotated. Once a sufficient spin accumulation has been built during the incubation time, the reversal time is mostly dominated by the reversal mechanism present. Comparison with Figure 4.5 shows that for all current densities and free layer dimensions the reversal time is much faster than the incubation time. The general trend of the reversal time with current density is seen to be the same as the incubation time. An increase in the current density initially produces a significant speedup in the reversal time before plateauing at higher current densities. This is an important observation, since this suggests the current density directly impacts the reversal mechanism, since it has the ability

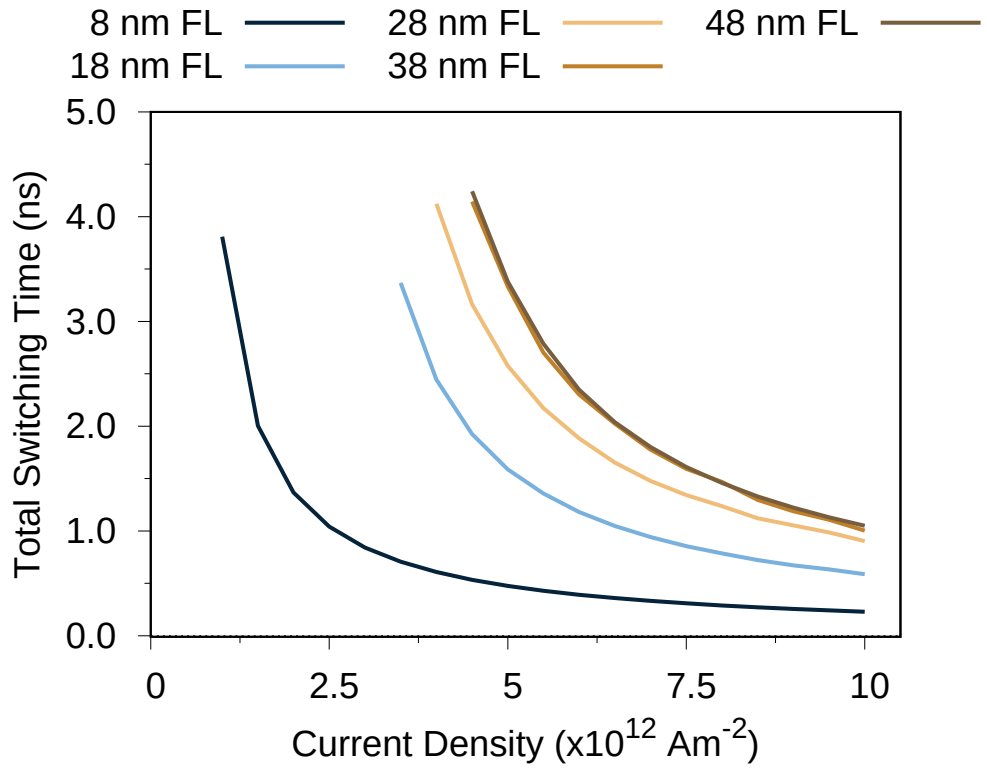

Fig. 4.7 Total switching times as a function of the current density for the different free layer thicknesses. The 8 nm free layer is significantly faster than the rest at any given current density in addition to the ability to be switched a significantly reduced current density. This is further evidence for a change of reversal mechanism between 8 nm and 18 nm. The incoherent towers then converge as the free layer is increased further beyond 38 nm.

to cause faster magnetisation reversal. This is also outlines the importance of modelling in the absence of thermal fluctuations, since thermal noise will also impact the reversal mechanism. The smaller 8 nm free layer is again seen to be the fastest at all current densities, which is due its coherent reversal mechanism. The taller towers all show evidence of incoherent rotation and thus are expected to have slower reversal times as the wall must propagate through the free layer. These incoherent towers follow the expected trend, with slightly slower reversal times as the free layer grows larger, due to the domain wall having to travel further. However, beyond 18 nm these plots are less smooth at lower current density, and become smoother at larger current density. This may suggest a reversal that is more complicated than a simple propagated domain wall at lower current densities. This further motivates the need for snapshots of the reversal process from earlier results, as is not clear in this figure alone.

For completeness, Figure 4.7 shows the total switching time, which is the sum of the incubation time and the reversal time, as a function of current density. The reversal time

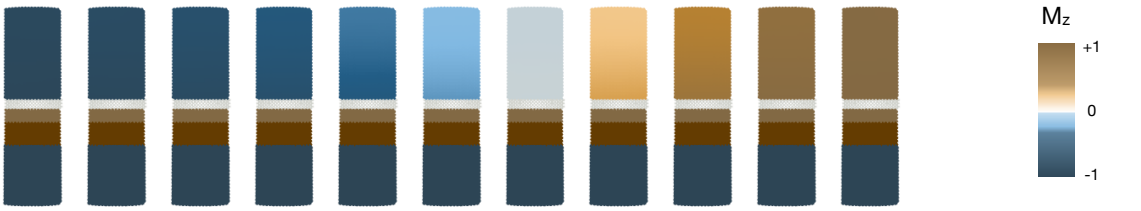

Fig. 4.8 Snapshots every 50 ps of the 8 nm free layer subjected to a current density of 5×10^{12} Am^{-2} at 0 K. The reversal is clearly seen to be coherent rotation as the free layer rotates uniformly.

is significantly smaller than the incubation time but follows the same trend. It is therefore no surprise that the total switching time is very similar to that of the the incubation time in Figure 4.5. Nevertheless the observations from Figure 4.7 are outlined here. The 8 nm free layer stands out as significantly different from the others. It requires a much smaller current density for reversal (with total switching time < 5 ns) compared with all the other towers. This would suggest that a coherent rotation would be ideal for designing the fastest or the most energy efficient PSA-MRAM when reversed via an STT mechanism. The significant gap between the 8 nm and and 18 nm is thus explained by a transition to an incoherent reversal that will be explored further in subsequent results. Increasing the free layer thickness further then reaches an asymptotic maximum, placing an upper cap on free layer thickness in design of future PSA-MRAM of these dimensions.

Given the results so far, it is essential to understand the reversal process as the free layer is increasing. To address this, snapshots of the reversal mechanism were created using POV-Ray for the 8 nm, 18 nm and 48 nm free layers. The first is expected to be coherent, while the latter two are incoherent. However, complications seem to be evident for the taller towers with a further transition between the 18 nm and the 48 nm free layer. Since the STT mechanism is significantly different to an applied field, it is well worth supporting these observations with snapshots for confirmation. For all imaging presented, the snapshots were produced every 1 ps for the full simulation, producing thousands of images. These images were then converted into GIF format to see if any unexpected behaviours occurred. The relevant separation of images were then selected to ensure the reader does not miss any detail. Figure 4.8 shows snapshots of the 8 nm free layer subjected to a current density of 5×10^{12} Am^{-2} at 0 K. The snapshots are separated by 50 ps. The reversal mechanism is seen to be coherent, with no noticeable or significant fluctuation. This supports the observations made in the previous graphs of this section, whereby the magnetisation length $|M|$ did not fluctuate

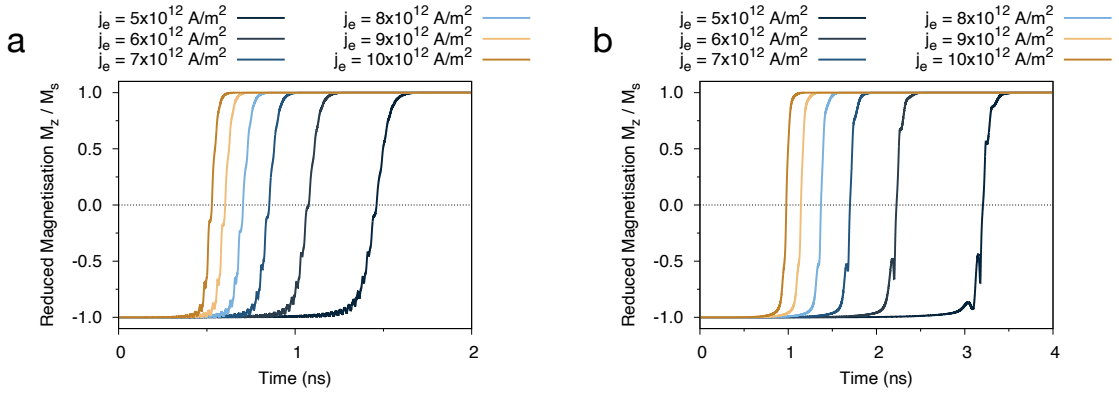

Fig. 4.9 The z-component of the reduced magnetisation for the a) 18 nm free layer and b) 48 nm free layer at increasing current densities. The small flick in the graph disappears as the current density reaches 8×10^{12} Am^{-2} for the 48 nm free layer, while these small fluctuations are present at all current density for the 18 nm free layer.

and the incubation and reversal times were smooth plots significantly faster than the taller towers. The reversal time for the 8 nm free layer at this current density can be roughly seen by eye in Figure 4.6 to be ≈ 0.2 ns which is consistent with the snapshots where it takes around four snapshots to reverse the magnetisation direction.

All of the free layers with a thickness greater than 8 nm have displayed evidence of non-coherent reversal. Further, this reversal often appears more complicated than just a propagated domain wall, which served as major motivation for snapshots of taller free layers. To demonstrate, the z-component of the reduced magnetisation (M_z/M_s) against time for the 18 nm and the 48 nm free layer is plot in Figure 4.9 (a) and (b) respectively for increasing current densities. Again, these towers are chosen as the reversal mechanism appears to transition above 18 nm. The small oscillations in the M_z component at 18 nm, and the larger oscillations in the M_z component at 48 nm were highlighted as suspicious in the discussion of Figure 4.4. These fluctuations are due to the precession in the M_z component and are suggestive of complications to the reversal mechanism, since a simple propagated domain wall would produce a smooth transition curve. The range of current densities displayed in Figure 4.9 is larger, increasing to the maximum current density in this study (10×10^{12} Am^{-2}). This is because, in the absence of thermal fluctuations, these behaviours must be a consequence of the current density and thus worth exploring the trend as this is increased.

Interestingly, the 18 nm free layer shown in Figure 4.9 a) displays non-smooth curvature even at increased current densities. This suggests that even at high current densities, free layers of this dimension follow a non-linear incoherent reversal mechanism. In contrast, the 48 nm free layer in Figure 4.9 b) shows that this oscillation disappears when the current density is increased to around 8×10^{12} Am^{-2}. At current densities greater than this, the reversal

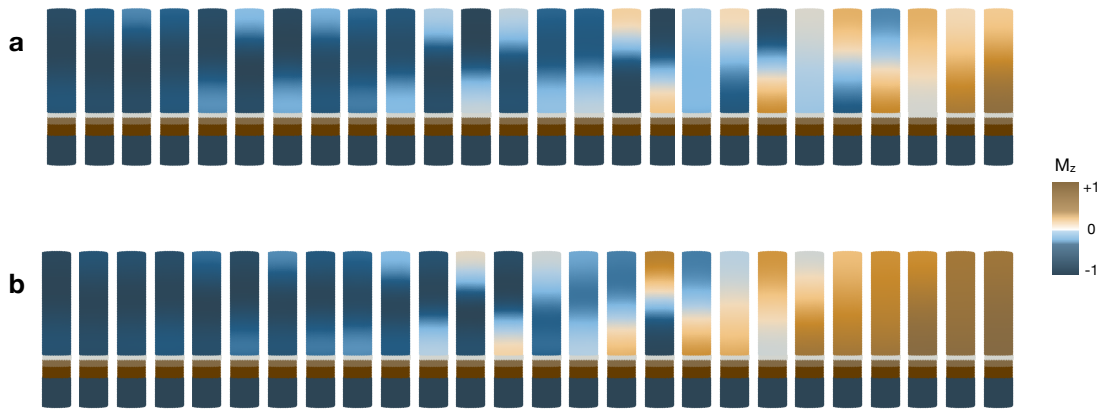

Fig. 4.10 Snapshots of the reversal mechanism for the 18 nm free layer at 0 K subjected to a current density of a) 5×10^{12} Am^{-2} and b) 8×10^{12} Am^{-2}. The fluctuations at the top of the free layer are still present even at high current density.

process appears smooth, suggesting the current density has overcome some complication in reversal and transitioned to a simpler propagated domain wall.

To explore what this unusual behaviour consists of, snapshots of the reversal for both the 18 nm and 48 nm free layer are produced. These snapshots show the reversal under a smaller current density of 5×10^{12} Am^{-2} and a larger current density of 8×10^{12} Am^{-2}. The lower current density is the lowest plot shown in Figure 4.9 while the higher current density was chosen to be the first current density whereby the oscillation in M_z has disappeared for the 48 nm free layer. As with the 8 nm snapshots presented in Figure 4.8 a few thousands snapshots were first compiled into GIF format to ensure the reader doesn't miss any details.

Firstly, Figure 4.10 shows the reversal of the 18 nm free layer at (a) the lower current density and (b) the higher current density. The snapshots are separated by 10 ps as the oscillations between the top of the free layer and the bottom are easily visible on this time-scale. Interestingly, there is a reversal attempt oscillating from the top and then the bottom of the free layer before eventually reversing from the bottom of the free layer. The reversal at the top of the free layer is able to hinder the progress of the domain wall from the bottom of the free layer. This explains the rapidly fluctuating M_z in Figure 4.9 and explains why it continues to oscillate between the top and the bottom until the spin accumulation is sufficient to drive a domain wall the whole free layer.

The domain wall is eventually driven from the bottom of the free layer as this is where

the largest spin accumulation is built up from the MgO. However, as some of the spin accumulation continues through the free layer during the incubation period a smaller spin accumulation is built up at the top of the free layer too. The top of the free layer has a loss of exchange (on the surface) and additionally lacks any uniaxial anisotropy (unlike the bottom monolayer of the free layer). Due to these shortcomings, the smaller spin accumulation built at the top of the free layer is sufficient to initiate a small amount of reversal. However, it is not quite enough to propagate a domain wall from the top down.

Comparing Figure 4.10 (a) and (b) it is interesting to note that the same behaviour is present at higher current densities. The reversal is clearly faster, as it takes less snapshots for the reversal to complete. The larger spin current density is able to build a sufficiently large spin accumulation at the base of the free layer faster.

In contrast, the reversal of the taller 48 nm free layer at the same lower and higher current densities are shown in Figure 4.11. Particularly, the M_z fluctuates with larger oscillations, rather than the rapid oscillations as seen in Figure 4.9. The reversal behaviour is different, where the reversal at the top and the bottom of the free layer do not oscillate, instead occurring in tandem initially. For this reason, the snapshots are separated by 50 ps to make it easier to see with no detail lost.

At the lower current density of 5×10^{12} Am^{-2} seen in Figure 4.11 (a) the initial partial reversal at the top of the free layer is still present. However, the central region of the free layer does not reverse, which is due to the increased shape anisotropy of this taller tower. The reversal from the top of the free layer travels only $\approx 20\%$ into the free layer, compared to the 18 nm case whereby it travels a much larger relative proportion. As a consequence, the reversal from the bottom of the free layer does not suffer significantly from this interference and begins the expected propagated domain wall in tandem. In other words, the reversal at the top of the free layer does not cause significant hindrance to the domain wall from the bottom until a propagating domain wall is well under way.

In Figure 4.11 (b) the current density is larger at 8×10^{12} Am^{-2}. The oscillations in the M_z had disappeared in Figure 4.9 and indeed the fluctuation at the top of the stack is now negligible. The reversal mechanism is now a propagated domain wall, thus the M_z curves become smoother for greater current densities. This is because at higher current densities the spin accumulation is large enough at the bottom of the free layer to produce a domain wall before any significant incubation has built at the top of the free layer.

To further probe this unexpected reversal behaviours in the taller free layers it is useful to explore what is happening to the spin accumulation as it progresses through the free layer. Starting at the base of the free layer, the spin accumulation as a function of depth in to the free layer are presented in Figure 4.12. The spin accumulation is layer resolved and is output at

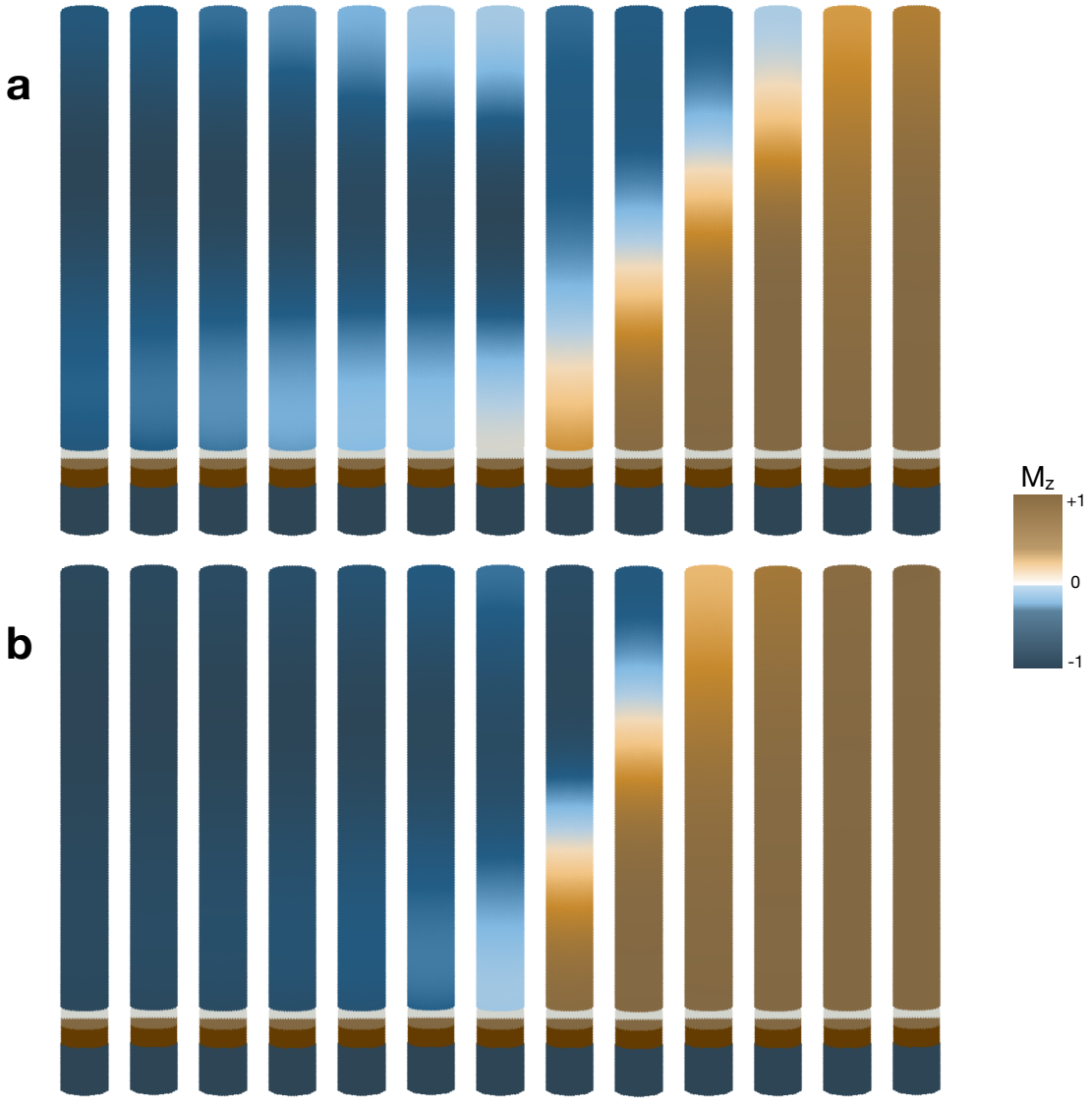

Fig. 4.11 Snapshots of the reversal mechanism for the 48 nm free layer at 0 K subjected to a current density of a) 5×10^{12} Am^{-2} and b) 8×10^{12} Am^{-2}. At the lower current density in a), there is clear rotation of the magnetisation at the top of the free layer that is not present at higher current density.

each time step in the same way as the snapshots (every 1 ps). This allows direct comparison between the snapshots in Figure 4.11 and the spin accumulation in Figure 4.12. Figure 4.12 (a) is the spin accumulation of the 48 nm free layer at a current density of 5×10^{12} Am^{-2}, and (b) is at a current density of 8×10^{12} Am^{-2}, as with Figure 4.11. To avoid an unclear and untidy graph, the spin accumulation is plot every 100 ps rather than the 50 ps output rate used for the snapshots. The start and end of switching, as labelled on Figure 4.12 correspond

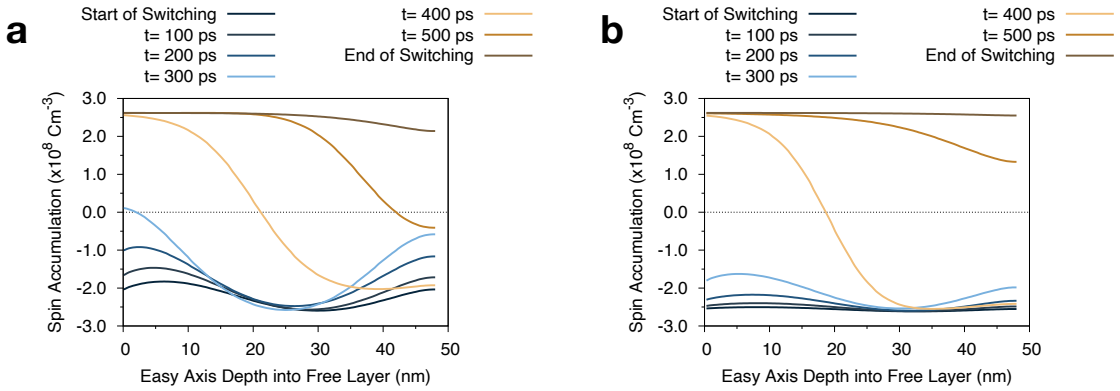

Fig. 4.12 Spin accumulation through the depth of the free layer for the 48 nm free layer at a current density of a) 5×10^{12} Am^{-2} and b) 8×10^{12} Am^{-2}. The start and end of switching correspond to the first and last snapshot in Figure 4.11, every $t = 100$ ps is thus every other snapshot.

to the first an final snapshot in Figure 4.11 for a given current density. Every 100 ps therefore corresponds to every other snapshot.

Focusing first on the lower current density, Figure 4.12 a), it is clear how the spin accumulation corresponds to the snapshots. At the base of the free layer (an easy axis depth of 0 nm) the spin accumulation grows with every 100 ps. At around t=300 ps the spin accumulation becomes positive, meaning more spin up than spin down electrons are present at the base of the free layer. At this point a domain wall rapidly propagates through the stack, thus at t=400 ps the positive spin accumulation reaches nearly halfway into the free layer ≈ 23 nm. Interestingly, the spin accumulation is almost symmetrical in magnitude from the base of the free layer to the top for the first 300 ps. The spin accumulation at the top of the free layer in this time does not build up into the positive regime, thus is not able to drive its own propagated domain wall. This does explain the significant fluctuation in the magnetisation at the top of the stack observed in Figure 4.11 however.

Focusing now on Figure 4.12 b), the free layer is subjected to a much larger current density and the spin accumulation follows a different pattern. There is still some symmetry in the spin accumulation for the first 300 ps, however at this stage the spin accumulation is not large enough to initiate any noticeable reversal. At such large current densities, the spin accumulation at the base of the free layer is large enough to initiate reversal before it reaches the top of the free layer. This is why a simple propagated domain wall is observed without any fluctuation at the top of the free layer.

4.3 Switching Dynamics With Finite Temperature

From chapter 3, the inclusion of finite temperature effects was shown to be vital for continued study of PSA-MRAM. Thermal fluctuations were found to partially drive the reversal mechanism in an applied field. While this chapter induces reversal via STT rather than an external field, a significant impact from thermal fluctuations on the reversal mechanism is still expected. This section therefore details the results of STT reversal at finite temperature. Firstly, the process of averaging with different starting seeds is outlined, as it is necessarily different to the averaging outlined in subsection 3.2.1. Then the systematic trends at finite temperature are presented and discussed. Finally, these are related to the behaviours and trends observed in the absence of temperature in the previous section.

4.3.1 Averaging

Much like the hysteresis results presented in subsection 3.2.1, the random nature of thermal fluctuations results in a range of possible switching pathways. To reiterate what was discussed in chapter 3, to emulate a stochastic thermal field VAMPIRE uses a sequence of pseudo-random numbers with a Gaussian distribution. By changing the starting seed, a unique sequence of numbers is produced, resulting in an independent evolution of the magnetic spins due to thermal fluctuations. For all of the results presented in this section, they are an average of forty independent simulations with different starting seeds. Since there are forty runs at every current density and every free layer thickness, this section presents results at 150 K, 300 K and 450 K. This number of data points is sufficient to see general trends across the functional temperature range of PSA-MRAM without being computationally unreasonable. For clarity, thermal averaging is demonstrated in Figure 4.13 for the 8 nm free layer at 300 K subjected to a current density of 1×10^{12} Am^{-2}. Clearly, a unique evolution of thermal fluctuations results in a completely independent reversal suggesting reversal is partially driven by temperature as expected. This also supports the requirement for the previous section of results in the absence of thermal fluctuations, as it would be difficult to discern thermal effects from spin torque effects without separate presentation. Much like the previous section, it is beneficial to extract an incubation time and a reversal time at finite temperature. This is achieved by fitting the tanh function as outlined in subsection 4.2.1 to each of the forty runs to find an incubation time and reversal time for that individual run. These times are then summed and averaged, and the averaged values will constitute the data points for that given current density, free layer thickness, and temperature. An averaged tanh plot is added to Figure 4.13 using the average value of σ and X_0 from all forty runs.

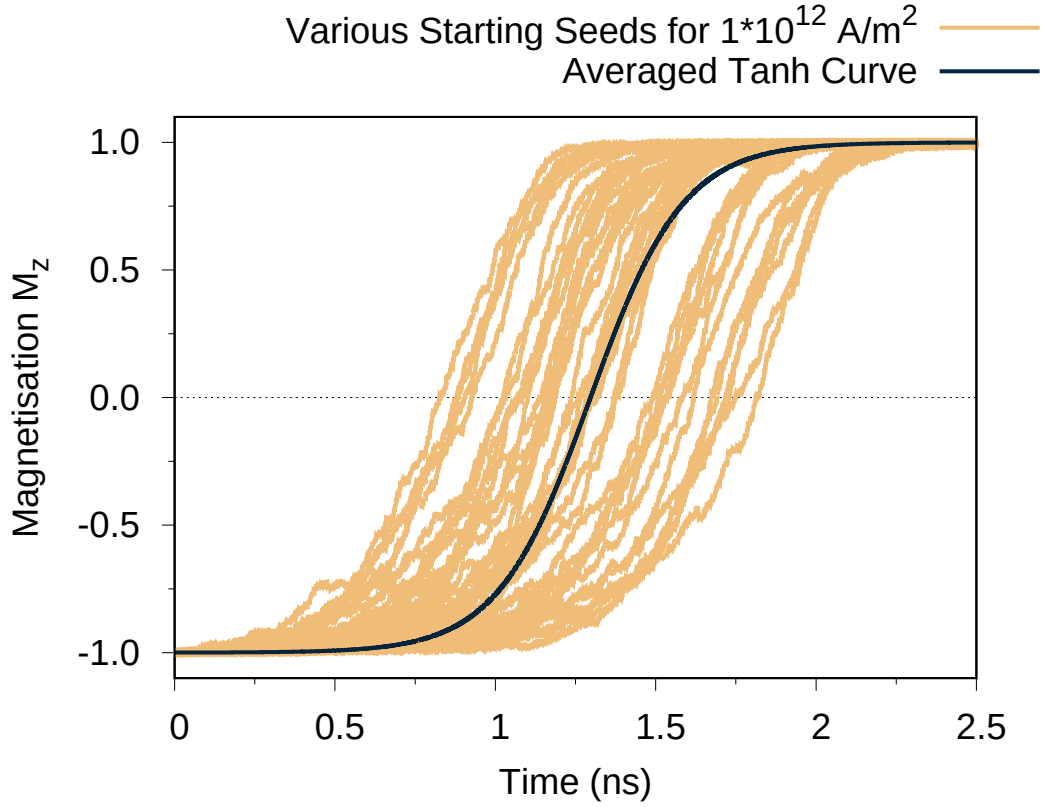

Fig. 4.13 Forty independent runs of the 8 nm free layer at 300 K subjected to a current density of 1×10^{12} Am^{-2}. Overlaying these is an averaged tanh function after fitting $\tanh \frac{x-X_0}{\sigma}$ to each of the forty curves.

This process is repeated at every current density, free layer thickness and temperature increment to systematically present the results of this section. As with the 0 K results, the current density will increase in steps of 0.5×10^{12} Am^{-2} over the range $0.5 \times 10^{12} \leq j_e \leq 10 \times 10^{12}$ Am^{-2}, with the free layer thicknesses of 8 nm, 18 nm, 28 nm, 38 nm, 48 nm. With forty simulations at each data point, and three temperature values modelled, this results in $12,000$ runs and took a significant amount of computational resources and time.

4.3.2 Results

For ease and clarity, the results at finite temperature are presented in two stages, since there are two variables (current density and temperature). Firstly, fixing the temperature, the trends as the current density is increased are explored, as in subsection 4.2.2. This is systematically repeated for 150 K, 300 K and 450 K. Secondly, fixing some current densities, the trends with temperature are explored. Plotting these independently and presenting separate discussion was found to provide greater clarity and insight. Since finite temperature requires forty

independent simulations at each temperature and each current density data point, this section required significant computing time on the HPC. This is why only three temperatures were modelled, where ideally smaller temperature increments would provide smoother data to better see trends. As with subsection 4.2.2, up to 5 ns of time are modelled, since any longer timescales would require prohibitively large computation time. All runs start with all atomic sites anti-aligned with the reference layer along the $-M_z$ direction. There are then $10,000$ equilibration steps, during which no statistics are taken and the spin current is not applied.
To start with, the incubation and reversal time as a function of current density are presented in Figure 4.14 while temperature is fixed at 150 K, 300 K and 450 K. This approach allows further exploration of the effects of current density as the thickness of the free layer decreases following subsection 4.2.2.
Firstly, the first column of Figure 4.14 shows the incubation time against the current density at 150 K, 300 K and 450 K. The same general trend is present at each temperature increment. The 8 nm free layer is significantly faster than the larger free layers, with the 28 nm free layer slightly larger and the taller three thicknesses reaching an asymptotic maximum. It is worth noting, that while the tallest three free layers are not completely overlapping, the small discrepancy between the plots is due to the thermal fluctuations. These trends in incubation time at finite temperature are the same trends that were observed in Figure 4.5. At a fixed temperature, therefore, any increase in current density will initially speedup the incubation time, before reaching a minimum incubation time. The following discussion for incubation times will therefore echo earlier discussion at 0 Kelvin.
The 8 nm free layer is known to display coherent rotation, and so is discussed independently from the taller towers. The incubation time is the time taken to build a sufficient spin accumulation in the free layer to initiate the reversal process. In this sense, the spin accumulation built will be sufficient for coherent rotation once the spin torque can overcome the shape anisotropy. The 8 nm free layer has significantly reduced shape anisotropy compared to the taller free layers as outlined in chapter 3. This can explain the lower incubation time, and similarly explains why the 8 nm free layer may be switched at reduced current densities as low as 0.5×10^{12} Am^{-2}. Increasing the current density rapidly reduces the incubation to a converging minimum incubation time of < 0.15 ns.
The incubation time for the 18 nm free layer is larger than the 8 nm free layer at all current densities and at each temperature increment. This is a particularly interesting free layer dimension, as the incubation time sits between the coherent 8 nm free layer and the taller three towers of this study. The reversal can be triggered with a current density as low as 1.5×10^{12} Am^{-2}, and with increased current density the incubation time plateaus around ≈ 0.3 ns. In the range of current densities studied, the flattening curve has not quite reached

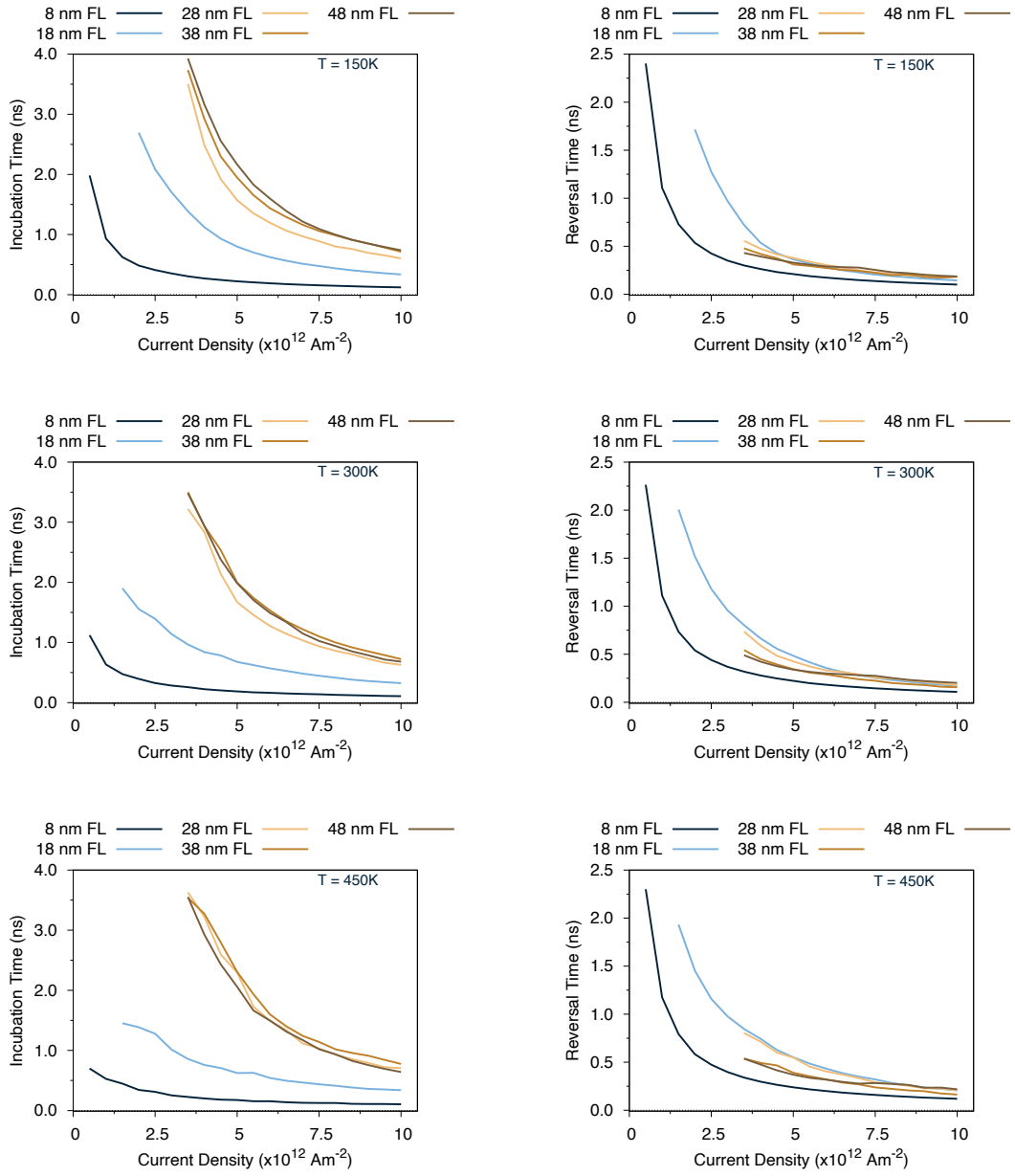

Fig. 4.14 Incubation time (left) and reversl time (right) as a function of current density at three fixed finite temperatures.

its asymptote yet, but by the maximum current density the incubation time is < 0.35 ns in all three graphs.

The tallest three towers overlapping incubation times is an interesting result, and is consistent at each temperature. These taller towers require an even larger minimum current density of 3.5×10^{12} Am^{-2} to initiate reversal. Again, the plot is beginning to plateau at the maximum

current density of this study, with an incubation time of ≈ 0.6 ns. As with the 18 nm free layer, the actual minimum incubation time has not been reached in this range of current densities.

These trends in incubation time can be largely explained with the shape anisotropy of the free layers. The 8 nm free layer has a significantly lower shape anisotropy, since its thickness is only slightly larger than its diameter (5 nm). As a result, a modest spin accumulation is capable of providing sufficient torque to initiate reversal. In contrast, the 18 nm has increased shape anisotropy and thus requires a larger spin accumulation. A particularly suggestive piece of evidence is the overlapping of the tallest three free layers. This is in tandem with these PSA-MRAM dimensions plateauing of shape anistropy, thus they all require the same spin accumulation to initiate a reversal process [116]. Since the incubation time is entirely before any complicated reversal behaviours, these trends are expected and easily accounted for.

Secondly, the second column of Figure 4.14 shows the reversal time against the current density at the same temperature values of 150 K, 300 K and 450 K. Once a sufficient spin accumulation has been built in the free layer, the reversal time is then mostly dependent upon the precise reversal mechanism for that stack. For this reason, the differing reversal time observed for the 8 nm free layer compared to the taller free layers was expected. The 8 nm free layer is the only one in this study to exhibit coherent rotation, while all other free layers exhibit incoherent rotation. This will necessarily lead to different reversal times. However, following the complicated reversal procedures outlined at 0 Kelvin, the reversal times of the taller free layers at finite temperature are worth exploring.

An interesting and unexpected trend is observed for the reversal times of the taller four towers (18nm - 48 nm), which display incoherent rotation. The 18 nn and 28 nm thick free layers appear to follow identical trends, while the taller two towers follow a distinctly separate trend. Further, the smaller two free layers have slower reversal times than the taller free layers until high current densities. At sufficiently high current densities, all four of these incoherent free layers converge on similar reversal times. By eye, they appear to converge at lower current densities at 150 K compared to 300 K and 450 K, though plots of the temperatures is shown in a subsequent figure. These observations are in agreement with the complications in the reversal process at 0 Kelvin. This is a particularly interesting result, however, because in the absence of the oscillating reversal mechanism the reversal time would be expected to decrease with decreasing volume. This expected result would be due to the distance the domain wall would have to propagate.

At 0 Kelvin, the top of the free layer was found to partially reverse and interfere with the domain wall from the bottom of the free layer. Further, only the 18 nm free layer

was small enough to suffer from oscillations at the top and bottom, whereas the taller towers simultaneously had movement at the top and the bottom. The domain wall was not significantly hindered once initiated in these taller towers. This becomes the basis for explaining what is observed in Fig. 4.14. At finite temperature, any domain wall propagation is known to be partially thermally driven. As a result, the small reversal at the top of the free layer may propagate further down the stack than it did in the 0 Kelvin case. Thus, the reversal from the top is able to inhibit the domain wall propagating from the bottom even deeper into the free layer. This explains why the 28 nm free layer now agrees with the 18 nm free layer, while at 0 Kelvin only the 18 nm free layer oscillated between the top and the bottom. The thermally driven boost to the reversal at the top results in the 28 nm free layer not being thick enough to produce a propagated domain wall as easily. Meanwhile, the tallest two free layers still have sufficient separation between the reversal at the top and the actual domain wall from the bottom that the majority of the free layer may reverse before interference. As with the 0 Kelvin case, at increased current density the domain wall can propagate from the bottom before any significant build-up at the top of the free layer, thus the reversal times begin to converge.

As with the 0 Kelvin case, some snapshots of the reversal process help to aid intuition. Therefore snapshots of the reversal time at 300 K for growing free layer thicknesses are shown in Figure 4.15 at a current density of $5 \times 10^{12}\text{Am}^{-2}$. This lower current density is low enough that the taller tower and the smaller towers are still on distinctly different pathways, while being large enough to reverse in a sensible number of snapshots. Again, a GIF of these reversal mechanisms were first produced to ensure the reader captures the key details. These snapshots in Figure 4.15 are for (a) the 8 nm free layer, (b) the 18 nm free layer and (c) the 48 nm free layer.

Figure 4.15 (a) is included for completeness, demonstrating the 8 nm free layer still undergoes coherent rotation at finite temperature. These snapshots are separated by 50 ps. This free layer is the only one to undergo coherent rotation in this study, which is supported by its distinct reversal and incubation time patterns in Figure 4.14.

The reversal of the 18 nm free layer is shown in Figure 4.15 (b) to explain the observed trend for both the 18 nm and 28 nm free layer in Figure 4.14. To be clear, at finite temperature both of these dimensions have the same reversal behaviours. Since the reversal is slower than the other towers at this current density and temperature, the snapshots are separated by 10 ps as indicated on the figure. Further, the oscillating partial reversal at the top and bottom has already been ongoing for around 0.1 ns before the first snapshot. The latter part of the reversal is shown to demonstrate how far into the free layer the partial reversal at the top may propagate. The reversal at the top of the free layer propagates around halfway into the

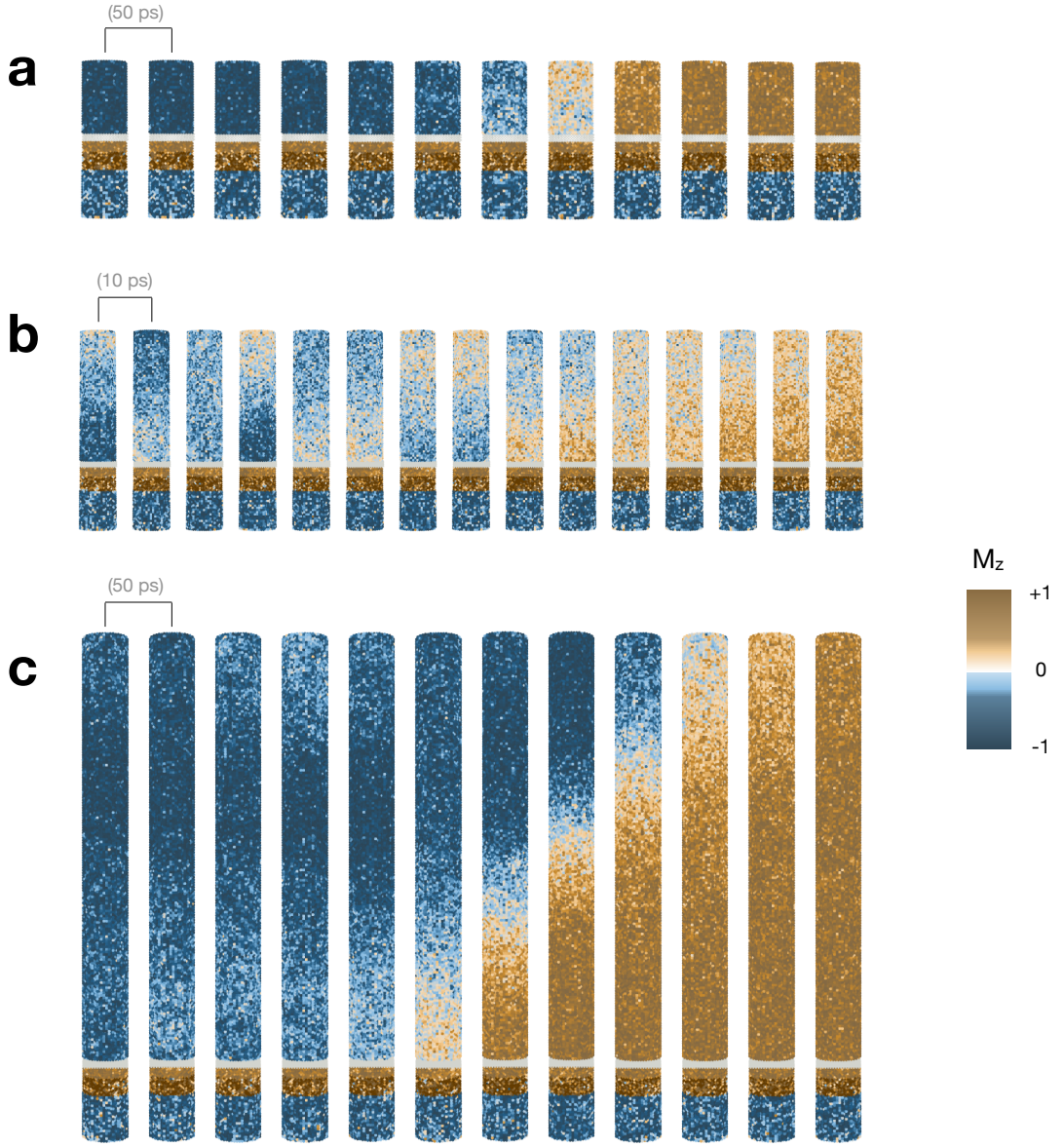

Fig. 4.15 Snapshots of the reversal mechanism for the a) 8 nm free layer, b) the 18 nm free layer and c) the 48 nm free layer at 300 K. In all case, the current density is $5 \times 10^{12}\mathrm{Am}^{-2}$. The smallest tower is coherent, while the taller towers are incoherent. The inhibiting oscillating reversal is present in the 18 nm free layer, while the tallest tower does not suffer significantly from this behaviour.

free layer before finally propagating from the bottom for the full reversal. This is significant interaction between the reversal at the bottom and top, leading to slower reversal times for these heights.

Finally, Figure 4.15 (c) shows the 48 nm free layers reversal, which is identical to the 38 nm free layer. Since the reversal for these free layers does not contain as much complication, these snapshots are presented separated by 50 ps as indicated on the figure. A small amount of reversal at the very top of the free layer is still visible, as in the 0 Kelvin case. The vast majority of the free layer is unaffected by the reversal from the top of the stack due to the increased shape anisotropy of the taller towers. The domain wall then propagates from the bottom of the free layer, and progresses mostly unhindered through the stack. These snapshots collectively support the insight from Figure 4.14. They also further show the complicated incoherent reversal observed in the 0 Kelvin case.

The results discussed and shown in Figure 4.14 explored the trends of current density at fixed temperature. It is also beneficial to explore the effects of temperature, which is achieved by keeping the current density constant. Therefore, in Figure 4.16 plots the incubation and reversal time against the temperature at fixed current densities of 3.5×10^{12} Am^{-2}, 5×10^{12} Am^{-2} and 10×10^{12} Am^{-2}.

Again starting on the left column of Figure 4.16, the trend of the incubation time with temperature is explored. In all plots, the incubation time is decreased as the temperature increases. This is because the increased thermal fluctuations provide pathways for the free layer to cross the energy barrier. chapter 3, in addition to other studies on MRAM [82, 61, 76], have shown that thermal fluctuations begin to drive the reversal mechanism at increased temperature. Since increased thermal fluctuations decrease the amount of spin torque required to initiate reversal, the spin accumulation takes less time to build to satisfactory levels.

It is worth outlining that while the incubation time of the 8 nm free layer appears relatively flat at all current densities in Figure 4.16, it is decreasing by a significant amount. At 450 K its incubation time has decreased by around $\approx 50\%$ compared to 0 K at a current density of 3.5×10^{12} Am^{-2} (from around ≈ 0.4 ns to ≈ 0.2 ns incubation time). The decrease in incubation time at a current density of 5×10^{12} Am^{-2} is similar, dropping by around $\approx 46\%$ incubation time by 450 K. At a large current density of 10×10^{12} Am^{-2} the incubation time only drops by around $\approx 30\%$, suggesting the current density begins to dominate the incubation time and the thermal fluctuations play less of a role. This same general trend is also observed for the 18 nm free layer, with very similar percentage decreases.

The tallest three towers again appear to be reaching an asymptotic maximum, though the 28 nm free layer is slightly reduced compared to the 38 nm and 48 nm free layers. This is due to the shape anisotropy, as discussed in previous figures. The reduction in the incubation time as temperature increases from 0 K to 450 K is also less than the smaller towers, decreasing only around $\approx 20\% - 30\%$ at a current density of 3.5×10^{12} Am^{-2}. This then drops further, with the incubation time dropping by around $\approx 10\% - 15\%$ at a current density of 5×10^{12}

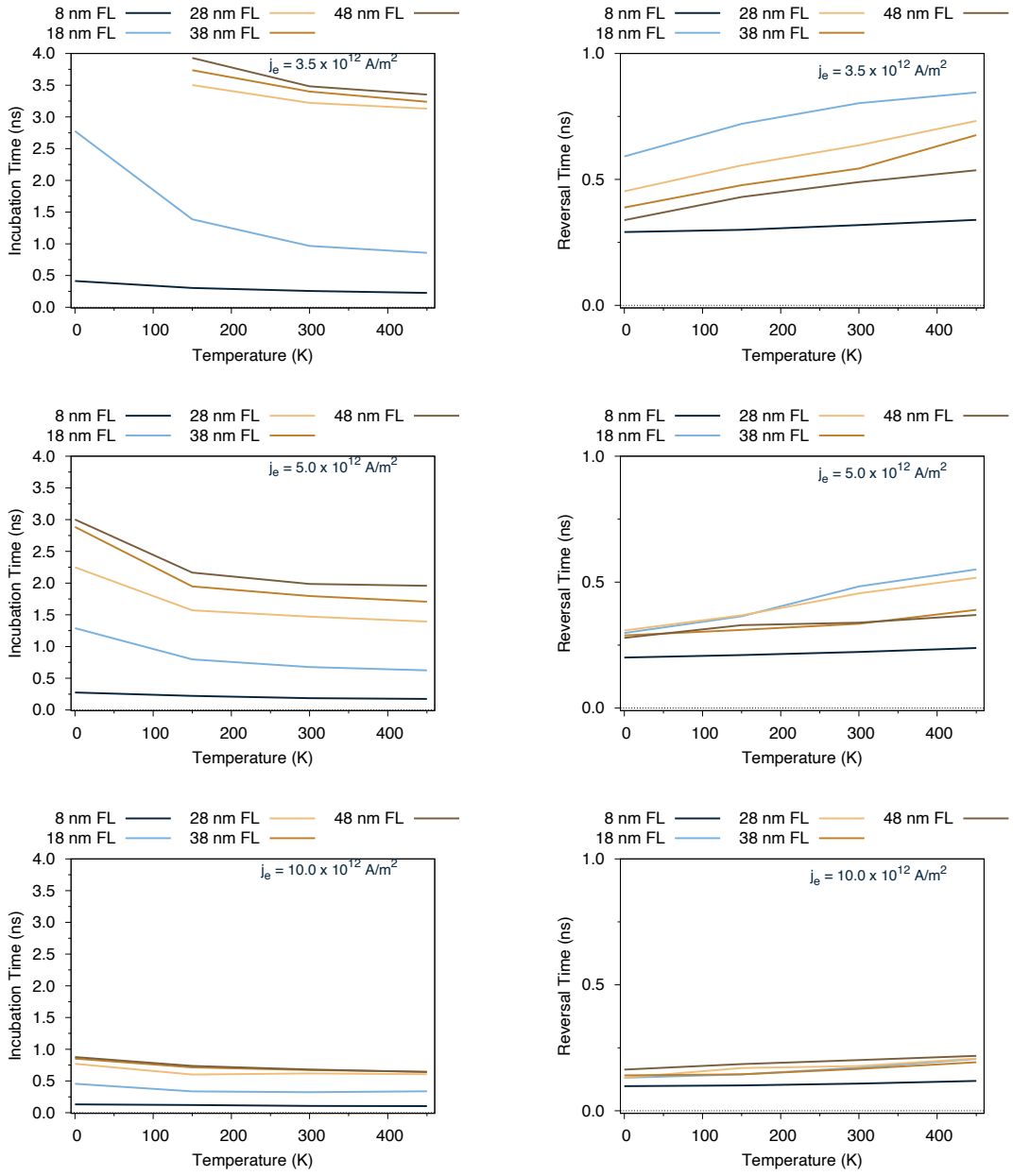

Fig. 4.16 Incubation time (left) and reversal time (right) as a function of temperature at three fixed current densities.

Am^{-2} and $\leq 10\%$ at a larger current density of 10×10^{12} Am^{-2}. This can be explained as a significant growth of shape anisotropy as the free layer thickness increases, and thus an increase in the thermal stability. As a result, the current density alone becomes the dominant factor in reversal over temperature for the taller towers in comparison to the smaller towers.

Finally, the second column of Figure 4.16 is compared, which plots the reversal time against the temperature at fixed current densities of $3.5(5.0)(10.0) \times 10^{12}$ Am^{-2}. Two key observations are; the decreasing reversal time for taller towers and the increasing reversal time as temperature increases. Both of these are unexpected results and are explained with the insight into the complicated incoherent reversal mechanism outlined thus far. It is easier, however, to see the temperature dependence of this behaviour in this figure compared to Figure 4.14.

The reversal time for the 8 nm free layer increases very slightly from 0 K to 450 K at a low current density of 3.5×10^{12} Am^{-2} (increasing by around < 0.04 ns. At a much larger current density of 10×10^{12} Am^{-2}, the increase in reversal time is even smaller at around < 0.02 ns. This is small enough to be within thermal noise and thus the reversal time for the coherent free layer can then be considered unchanged at finite temperature. A coherent rotation is somewhat simpler, in that the increased thermal fluctuation don't have much significant impact on the reversal mechanism once it is underway (i.e. after the incubation time).

It is easiest to discuss the taller free layer at each current separately. For this discussion, the 8 nm free layer is now ignored, as the focus is now on the incoherent reversal. At a current density of 3.5×10^{12} Am^{-2} the reversal time decreases steadily as the free layer increases in thickness at any temperature. The taller free layers did not reverse at this lower current density, which is why they start at 150 K. This counter-intuitive phenomena whereby the smaller towers reverse slower was also discussed in Figure 4.14. It is due to the reversal at the top of the free layer having a larger relative hindrance on the domain wall propagation for the smaller free layer compared to the taller ones.

Additionally, it is now also clear that the relative impact of the thermal fluctuations is much less for the taller free layers. For example, from 150 K to 450 K, the reversal time for the 48 nm free layer increases by ≈ 0.1 ns. In contrast, the 38 nm free layer increases by ≈ 0.12 ns, and the 18 nm by 0.2 ns. An anomalous result is the 28 nm free layer, which jumps up at 450 K. This is a benefit of expressing the data both at fixed current and fixed temperature in this section. The reason for this jump, is this free layer is transitioning between the two incoherent behaviour at this increased temperatures. At this smaller current density, the 28 nm free layer behaves more like the 38 nm and the 48 nm free layer at 150 K and 300 K. At these temperatures, and this low current density, the fluctuations at the top of the stack do not propagate enough into the free layer to cause significant oscillations. As temperature increases, however, the thermally driven reversal from the top becomes more significant and the reversal mechanism will transition. This was much less obvious in Figure 4.14, though it is visible that the 28 nm free layer isn't quite overlapping with the 18 nm free layer until 450

K.

Continuing to focus on the taller free layers, at a current density of 5×10^{12} Am^{-2} it is now seen that the smallest two free layers follow the same trend at all temperatures, and the taller free layers follow a differing one. This effect was alluded to earlier in Figure 4.14, but comparison between this current density and 3.5×10^{12} Am^{-2} offered fresh insight. At this increased current density, the spin accumulation reaching the top of the free layer is sufficient to force the 28 nm free layer to behave like the 18 nm free layer. It is interesting to note that this behaviour is both current and temperature dependent. As a result, both the operational temperatures and the current density used would have to be considered for future STT-PSA-MRAM designs and optimisation.

Finally, at a current density of 10×10^{12} Am^{-2} all of the taller towers are roughly converged. This current density is sufficiently large create a propagated domain wall from the bottom of the stack before any significant accumulation can build at the top of the stack to reverse the process. It is still not quite perfect, as the 18 nm free layer still displays noticeable fluctuation even at this increased current density, as seen in Figure 4.9.

4.4 Summary

In this chapter, the reversal mechanism of 5 nm diameter PSA-MRAM subjected to a STT mechanism are systematically explored at growing current density, temperatures, and free layer thickness. The current density was increased from $1 - 10(\times 10^{12}$ Am$^{-2})$, while the temperature was increased from 0 - 450 K, spanning the operational temperature range. It was found that when the free layer is reduced to 8 nm thick, the reversal is coherent regardless of temperature or current density. The incubation time and reversal time are rapidly decreased with increasing current densities for this tower dimension. Increasing the temperature reduces the incubation time even further, while having negligible effect on the reversal time. Increasing the free layer thickness to 18 nm sees a transition to a complicated incoherent reversal. Particularly, the relative lack of shape anisotropy leads to fluctuations in the magnetisation at the top of the free layer. This is able to inhibit the domain wall from the bottom of the free layer, presenting an oscillating effect before eventually reversing via a propagated domain wall. This behavior was present at these dimensions for all current density and temperature and leads to slower reversal times than the taller towers, which gets worse at increasing temperatures. The 38 nm and 48 nm free layer also display small fluctuation at the top of the stack, but this is neither significant enough to produce oscillations, nor is it present at all current densities. Increasing the current density eventually leads to a smooth propagated domain wall for these taller towers. Finally, the 28 nm free layer demonstrates a

transition from one mechanism to the other. It follows the trend of the taller towers at 0 K, and at 150 K and 300 K if the current density is low. At increased temperature of 450 K, or increased current density, this dimension follows the trends of the 18 nm free layer.

5

Calculation of the energy barrier for PSA-MRAM using Constrained Monte Carlo

One of the most important parameters to determine for the design of magnetic storage device such as MRAM is the dimensionless thermal stability factor Δ. This determines the data retention of the device and should be $\Delta > 60$ to satisfy industry requirements of a 10 year retention time. The thermal stability is given by $\Delta = \frac{K_u V}{k_B T}$, where the numerators product $K_u V$ is the energy barrier separating one magnetisation state from another in a uniaxial system. In PSA-MRAM, the energy barrier is dominated by the shape anisotropy, with a small additional impact from the uniaxial anisotropy at the MgO barrier. In this chapter, the energy barrier for the free layer is obtained by means of the constrained Monte Carlo method outlined in chapter 2. Using this, the thermal stability as a function of temperature and free layer thickness is presented. From results in chapter 3 and chapter 4 it is evident there is a transition from coherent to incoherent reversal of the free layer as the thickness of the free layer is increased. To address this, a constrained method that resembles incoherent reversal is utilised for the taller towers, and one for coherent reversal is used for the smallest tower. The choice of constraint is significant, so two such approaches are presented for the incoherent method. Firstly, a method referred to as the nucleation method is presented though in its current state does not produce good results. Secondly, a double constraint method is presented with more reasonable results for the incoherent reversal. Finally, this is then followed by a section whereby the free layer is forced to coherent rotation. Previously, there has been significant interest in the energy barrier and thermal stability of in-plane MTJ devices [135–137], but comparatively little on PSA-MRAM structures. An atomistic model of these structures capturing finite size and thermal effects is essential to support to the micromagnetic and experimental approach studied thus far [138].

5.1 Nucleation

Throughout this work, the free layer is studied at five thicknesses, 8 nm, 18 nm, 28 nm, 38 nm and 48 nm. Of these, all but the 8 nm free layer display incoherent reversal behaviour. This is an important consideration, as for non-uniform reversal the energy barrier should follow a distinctly different curve to the coherent case. Care must therefore be taken when choosing a constraint method for the free layer. In this section, the energy barrier is obtained from simulation of an incoherent reversal for all towers (including the 8 nm free layer). It is expected that the 8 nm free layer should be anomalous, while the taller towers will be compared to experimental and analytical trends. This is the first of two attempts to model incoherent reversal, where the second is found in section 5.2. This section constrains the top of the free layer to insert a domain wall at the top, which is then allowed to propagate down the stack.

5.1.1 Method

For all the results in this section, the system is first equilibrated for 100000 Monte Carlo steps, then statistics are taken over 2000000 further Monte Carlo steps. The majority of the tower structure is modelled using the adaptive Monte Carlo outlined in subsection 2.2.1, including the CoPt layers and the reference layer. Only the nominated sections of the free layer are modelled with the constrained Monte Carlo method (a more detailed outlined of the method is found in subsection 2.2.2. An outline of the procedure is presented below, which is then repeated at 150 K, 300 K and 450 K to obtain a range of results. As with the results found in chapter 4, this range of temperatures spans the majority of operational temperatures. While smaller temperature increments would be ideal, the results presented in this chapter required significant time and resource.

To obtain a value for the energy barrier, the constrained Monte Carlo method is used on some layers in the free layer. The torque for these layers will therefore not vanish. By sweeping through constraint angles from $0^\circ - 180^\circ$, the restoring torque as a function of constraint angle is produced. Integrating this will provide the energy barrier for the free layer, which is subsequently used to calculate the thermal stability factor.

To explore the energy barrier for the incoherent reversal mechanism via nucleation, several layers at the top of the free layer are constrained to mimic a domain wall insertion. These layers are constrained at 10° increments from $0^\circ - 180^\circ$, while the rest of the free layer is always initialised along the $+z$ easy axis. The large number of equilibration steps and Monte Carlo steps is thus to allow the free layer to evolve from a forced domain wall at the top to a

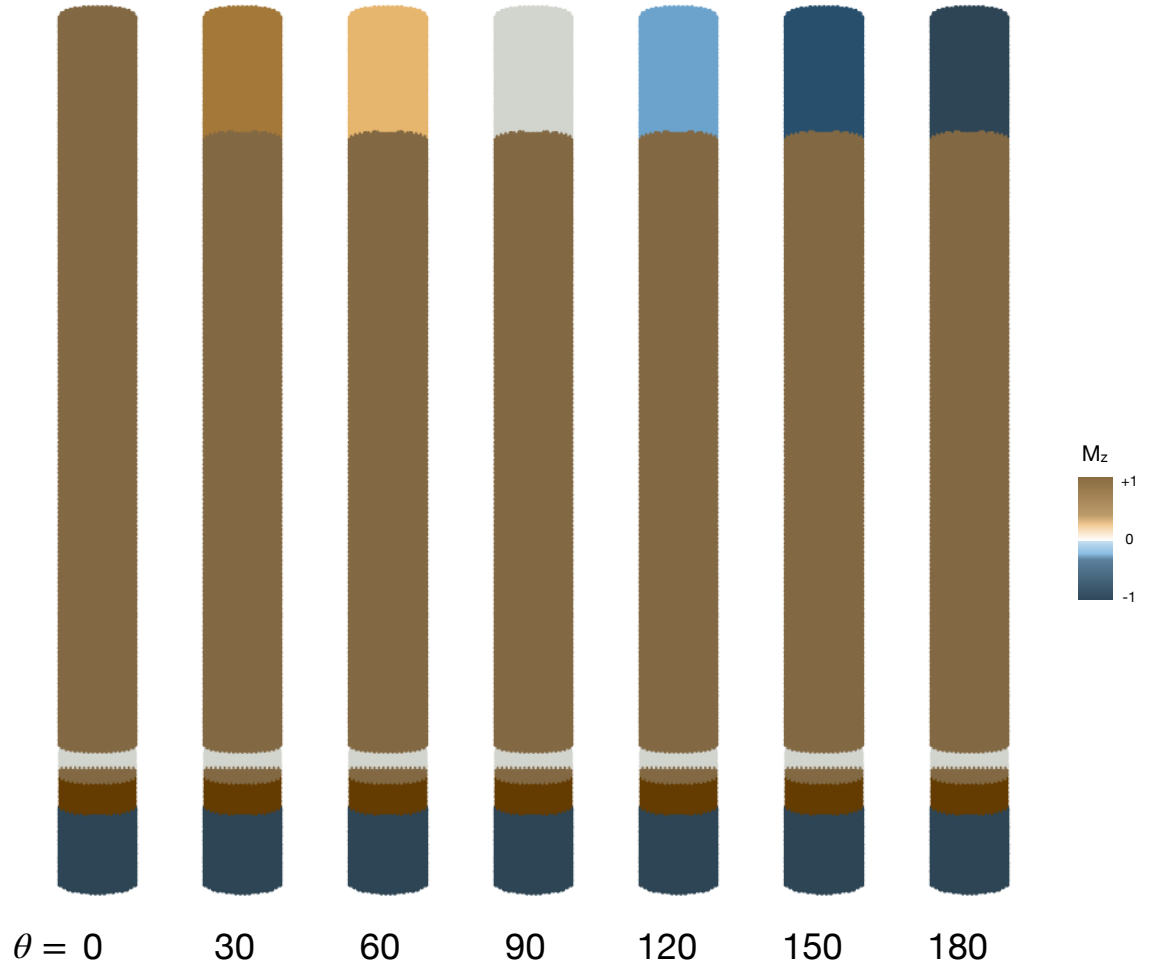

Fig. 5.1 Snapshots every 30° demonstrating the 8 nm at the top of the free layer that are constrained. The rest of the free layer then evolves using the adaptive Monte Carlo method.

propagating domain wall. The restoring torque after evolving is then dependent on the depth of propagation of a domain wall, which itself depends on the starting angle of the constrained layers. Snapshots of the starting conditions every 30° for the tallest tower (48 nm free layer) are shown in Figure 5.1 for clarity. The rotating layers at the top are constrained to their respective angle θ, while the rest of the free layer is allowed to evolve.

Since it has been shown that the 8 nm free layer rotates coherently, the thickness of the constrained section is 8 nm for all the taller towers. In the 8 nm free layer, the constrained layers are only 4 nm, as a special case. This is forcing a domain wall into a free layer that does not naturally form one, and acts as an interesting test of this approach. This should present a larger energy barrier than expected, since it is not favourable to force a domain wall

into these dimensions.
After the equilibration steps and the final Monte Carlo step has completed, the averaged magnetic properties are assumed to be in the final state. This final state is what is used to plot the results in this section. As with the previous chapters, thermal fluctuations lead to a unique evolution of the spin states and an average is required. All results presented in this chapter are therefore an average of forty independent runs, each with a different starting seed.

5.1.2 Results

Firstly, the averaged z-component of the magnetisation of the non-constrained free layer is presented as a function of the constraint angle at 300 K in Figure 5.2. At small angle constraints ($< 30^{\circ}$), the averaged magnetisation is just less than one, demonstrating the spins are not aligning with the constrained layer. The fractional reduction from $M_z = 1$ is due to the thermal fluctuations alone. The torque exerted on the free layer at small angle is not sufficient to propagate a domain wall. Increasing the constrained angle further continues to increase the torque between the constrained layers and the free layer. At a critical angle, the torque becomes sufficient to begin driving a domain wall down the free layer stack. As expected, this critical angle increases as the free layer thickness increases due to the increased shape anisotropy. The shape anisotropy provides stability, which increases the resistance to the domain wall propagation so a larger torque is required.
There is further complication however, since if the shape anisotropy alone was dictating the reversal, the taller towers would be expected to be closer to overlapping. A small discrepancy would be present since the domain wall has further to travel for the taller free layer, so its transition from $M_z = 1$ to $M_z = -1$ would follow a slightly longer path. However, in our data, the critical constraint angle that initiates reversal is clearly different between the taller free layers. This is a consequence of the method used, whereby the reversal mechanism in the free layer hasn't completed before the final step. There are two alternative methods that could fix this discrepancy. The first is to do more Monte Carlo steps per run, allowing the domain wall to propagate the maximum distance based upon the torque. This was not possible as the large number of Monte Carlo steps utilised already requires significant computing time. The second, is to produce a checkpoint of the magnetisation direction for every spin at the end of each constraint angle. Taking this checkpoint of spin direction and then feeding this as the starting position for the subsequent constraint angle means significantly less equilibration would be required. This is also problematic for computing time, since each constraint angle would have to be submitted sequentially. The method used in this study allows each angle constraint to be run independently, saving significant time.
Ultimately, this problem leads to false results for this method and must be overcome with one

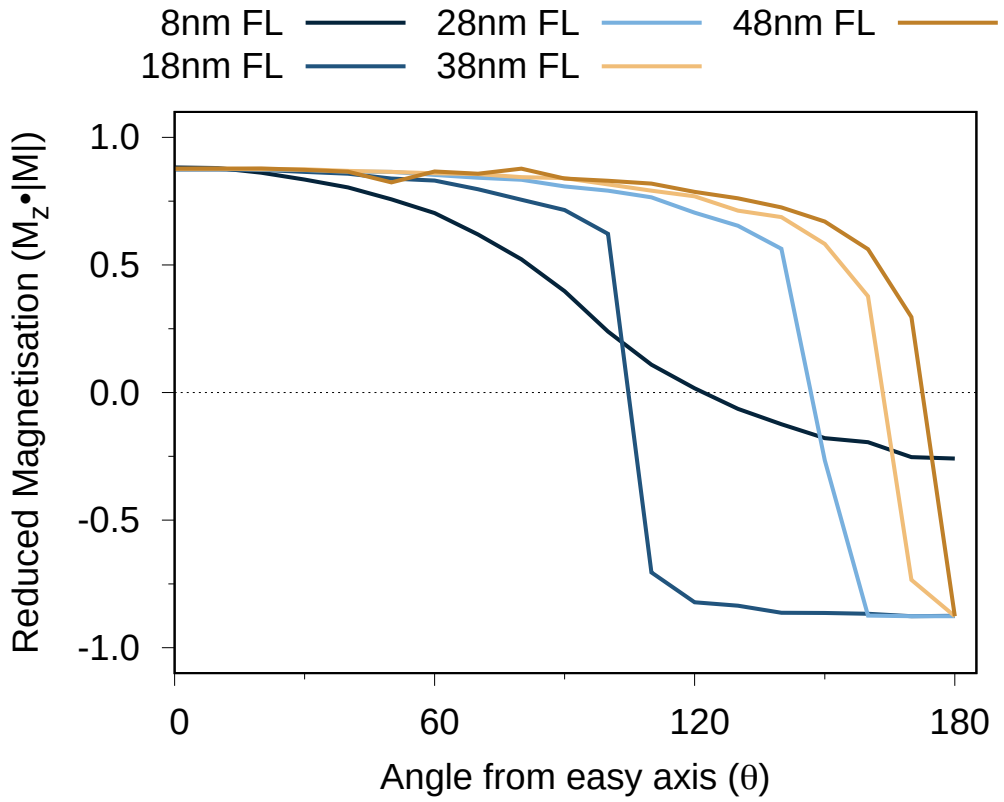

Fig. 5.2 The Magnetisation of the non-constrained bulk of the free layer against the constraint angle of the constrained section. As expected, the 8 nm free layer is not behaving, while the taller towers are following incoherent reversal mechanisms.

of the two solutions outlined above for further study. The results presented in this section are are still presented as a comparison between this method and the alternative method outlined in section 5.2.

Finally, the 8 nm free layer does not undergo reversal under this method, so is rejected from further plots in this section. As mentioned, this free layer was constrained for only 4 nm, allowing the other 4 nm to evolve with the domain wall forced in exactly halfway. This was expected to fail, since this is much smaller than a domain wall should be. At these dimensions, the free layer does not undergo incoherent reversal normally, and forcing a domain wall is unnatural. The thermal stability for these reduced dimensions will instead be presented in (section 5.3).

As outlined in subsection 2.2.2, the Helmholtz energy is obtained via integration of the torque curves with respect to constraint angle. The angle is constrained away from the easy axis along the $x-z$ plane by default, so the y-component of the restoring torque against the constraint angle is presented in Figure 5.3 a) at 300 K. Integration of the angular dependence

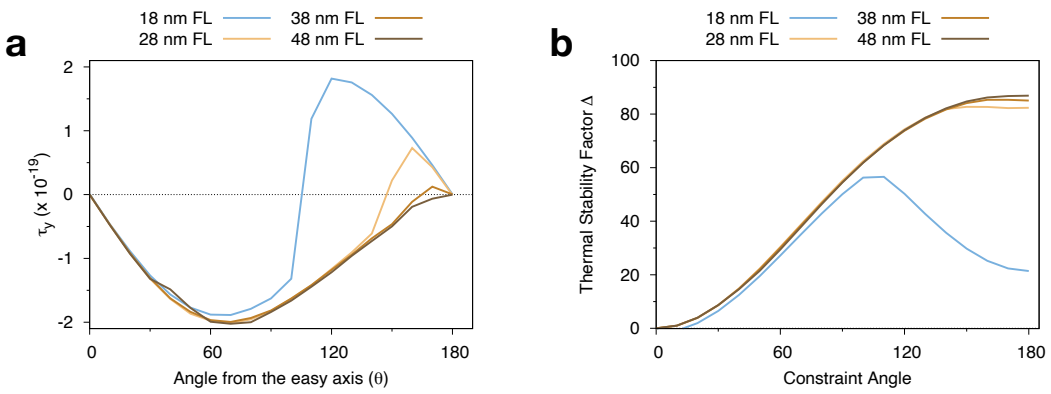

Fig. 5.3 a) the y-component of the restoring torque as a function of constraint angle at 300 K and b) the thermal stability factor, found by integrating a) and dividing by k_BT.

of the torque provides the free energy, which divided by k_BT provides the thermal stability. The corresponding thermal stability is shown in Figure 5.3 b).

In Figure 5.3 a), the torques are initially overlapping for all free layer thicknesses. The torque curves are best explained by comparison with Figure 5.2. At low angle, the domain wall is not propagating as seen in Figure 5.2. The torque between the constrained section and the bulk of the free layer is therefore increasing as the angle increases. By a constraint angle of $\approx 60°$, the evolution of the free layers magnetisation begins to differ between the growing free layer thickness. Once the constraint angle is sufficient to cause domain wall motion in the rest of the free layer, the torque rapidly flips to the opposite sign for the 18 nm free layer. This is because once the domain wall propagates to the bottom of the stack, the bulk of the free layer will then be aligned along the $M_z = -1$ direction. The top of the free layer, however, remains at its constrained angle so will continue to have torque until it is also aligned in this direction at 180°. The 18 nm free layer is seen to do this, while the 28 nm free layer follows a reduced path, the 38 nm free layer has a very small change, and the 48 nm free layer does not flip sign. The 48 nm free layer only manages to propagate a domain wall completely through the free layer stack on the final constraint angle. At this point, the constrained section is at an angle of 180° and the free layer reverses to $M_z = -1$, so the torque drops to zero. The middle towers, with a 28 nm and 38 nm free layer follow the same explanation as the 18 nm free layer, but they require a larger constraint before the free layer reverses. Consequently, the constraint angle is closer to $M_z = -1$, so the torque is relatively smaller.

If these results were correct, all of the taller towers would follow the same path as the 18 nm free layer. They would propagate a domain wall when the angle reaches 90° and thus would flip sign allow the same path. The inability of the taller towers to propagate a domain wall

until very large constraint angle is a consequence of this method. With a much larger number of Monte Carlo steps, or the use of check pointing each constraints final state to feed into the next angle, these results would likely become viable. This will require more time and further study to confirm. Due to this problem, which was also identified in the discussion of Figure 5.2, the thermal stability factors in this section must be rejected.

In Figure 5.3 b), the curves are the result of integrating the curves in Figure 5.3 a) and dividing by k_BT. The integration is performed with the composite Simpson's rule given by

$$\int_a^b f(x) = dx = \frac{h}{3}[f(x_0) + 2\sum_{j=1}^{(n/2)-1} f(x_{2j}) + 4\sum_{j-1}^{n/2} f(x_{2j-1}) + f(x_n)] \tag{5.1}$$

where the step size h is given by

$$h = \frac{b-a}{n} \tag{5.2}$$

and n is the number of points. The thermal stability factor is then extracted as the maximum point on the curve. With the suggested improvements to this method, all of these curves should have a similar shape to the 18 nm curve. They should rise to a maximum value which is the thermal stability factor, before reducing again symmetrically. Even the 18 nm free layer should reduce back down to closer to 0 by $\theta = 180°$. The taller towers would be expected to follow the same shape, but with a higher or lower peak depending on their own thermal stability.

Nonetheless, the thermal stability at 300 K can be compared with those found via a macrospin model by Perrissin et. al. for PSA-MRAM structures [138]. That study found the thermal stability plateaus at $\Delta \approx 80$ for 5 nm diameter devices and free layer thickness greater than ≈ 40 nm. Below this thickness the thermal stability rapidly drops for such small diameters. These studies differ slightly, since the free layer in that study used a thin CoFeB layer coupled to a much larger Co layer. It is reasonable to expect the tower structures in this study are very similar however. Additionally, atomistic studies capture finite size and surface effects that micromagnetic studies cannot, so small discrepancy is expected. For all cases, this method has predicted thermal stability factors that are larger than that found in other studies. These values should be rejected given the failure of the method to initiate reversal as hoped.

This process was repeated at 150 K and 450 K to span the operational temperature range of PSA-MRAM, as in previous chapters. The thermal stability as a function of temperature is presented in Figure 5.4 for the incoherent free layers. The industry target or $\Delta = 60$, corresponding to a ≈ 10 year retention time is added for context.

As expected, increasing the temperature decreases the thermal stability factor. Increased thermal fluctuations are able to partially drive the reversal mechanism as explored in chapter 3.

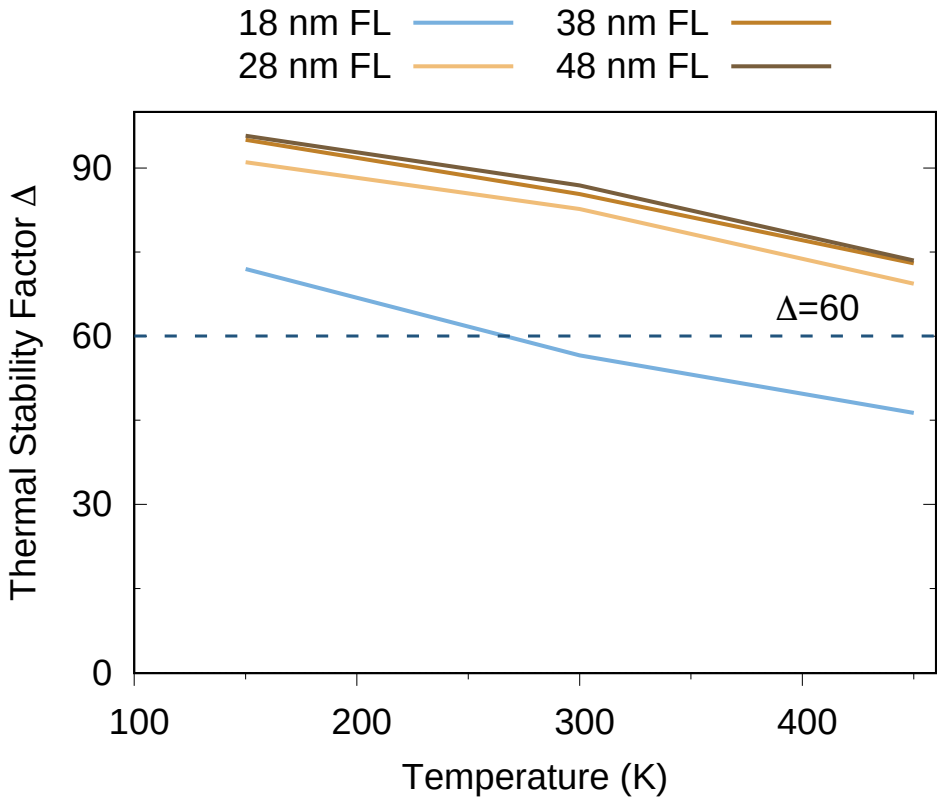

Fig. 5.4 The thermal stability factor as a function of temperature for the free layers that exhibit incoherent reversal. The thermal stability is reduced with temperature as expected. The 18 nm free layer is found to reduce below industry targets by 300 K.

It is therefore unavoidable that increasing the temperature reduces the ability to retain a magnetic state.

Within the range of operational temperatures, the tallest three free layers are found to have a sufficient thermal stability for industry targets. The tallest two towers are almost identical, with the 28 nm free layer only slightly reduced. Despite the shortcomings of this method, this is in good agreement with the coercivity trends found in chapter 3. Further, this is explained as a consequence of the shape anisotropy, since the ratio of the demagnetisation factors in the tallest free layers was found to be plateauing towards a maximum.

In contrast, the 18 nm free layer has significantly reduced shape anisotropy. In Figure 5.4 it was found to reduce below the industrial requirements for thermal stability by operational temperatures. The thermal stability is above the target at 150 K, but has dropped by room temperature. For context, at 150 K the 18 nm thermal stability is $\Delta = 71.9$, which is only just above the 28 nm free layer at 450 K ($\Delta = 69.5$).

5.2 Double Constraint Method

The nucleation method presented in section 5.1 attempted to model incoherent reversal in the free layer to calculate the thermal stability. It's shortcomings could be overcome at the expense of longer computational time, either with more Monte Carlo steps or a checkpoint technique. However, since this wasn't possible within a suitable time frame, an alternative method is presented in this section. The purpose is identical, however, as this section aims to calculate the thermal stability for towers undergoing incoherent reversal. In this section, a monolayer is constrained at the top and the bottom of the free layer. The bulk of the free layer is split into to halves, with the top half starting aligned with the top constrained monolayer, and ditto for the bottom half to the bottom monolayer.

5.2.1 Method

As with the nucleation method, all simulations start with 100000 equilibration steps and then statistics are taken over a further 2000000 Monte Carlo steps. In this method, only a monolayer at the top and bottom of the free layer are modelled using the constrained Monte Carlo method. The rest of the free layer is modelled using the adaptive Monte Carlo method. The free layer is then divided into two halves, always exactly at the center of the free layer. The top halves magnetisation direction is always initialised along the same direction as the top constrained monolayer. Similarly, the bottom half is always initialised along the same direction as the bottom monolayer. Thus, when the top half and the bottom half start at different angles, a domain wall is forced into the center of the free layer. Since the bulk of the free layer is not constrained, this domain wall is then allowed to evolve. Depending on the relative angle of the two halves, the domain wall may propagate upwards, downwards or stay roughly central.

In this method, the top half of the free layer is rotated sequentially through 180° in steps of 10° while the bottom half is left aligned along the positive easy axis (aligned with the reference layer). This is shown in Figure 5.5 a), where for consistency this rotation is referred to as angle θ. Once the top half has rotated 180°, it will be completely anti-aligned with the bottom half. The bottom half of the free layer is then rotated sequentially through 180° in steps of 10°. This is shown in Figure 5.5 b) and is referred to using angle ϕ. This will therefore reduce the torque between the layers with each subsequent increase in angle until the free layer is completely magnetised along the negative easy axis.

Since there are two constrained layers in this method, care must be taken when plotting the torques angular dependence. In this setup, the difference in the torques between the top

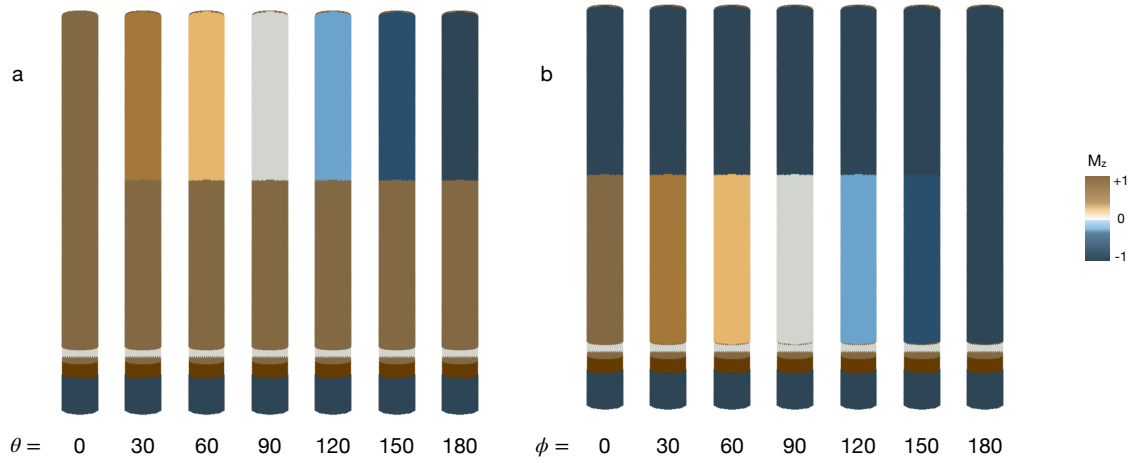

Fig. 5.5 Snapshots every 30° for the starting magnetisation for a) the top halves rotation through angle θ and b) the bottom halves subsequent reversal through angle ϕ.

monolayer and bottom monolayer will provide the torque of the system. That is, $\tau_\theta - \tau_\phi$ where τ is again the y-component of the restoring torque. This method is the same as the process used by Evans et. al [139] which used the constrained Monte Carlo algorithm to obtain the exchange coupling. As with the nucleation method, the torque curves are then integrated using the Simpson's method in Equation 5.1 and divided by k_BT to obtain the thermal stability.

5.2.2 Averaging

Since this method is applied at finite temperature to obtain the thermal stability factor, the impact of thermal fluctuations must be considered. As the angle between the top half and the bottom half of the free layer becomes larger, the subsequent movement of the domain wall becomes less predictable. This is discussed further in the following results section, but for now it is sufficient to demonstrate this when the top of free layer starts at $\theta = 150°$ and the bottom half starts at $\phi = 0°$. At such angles, the domain wall is still mostly expected to propagate upwards, since the bottom half of the free layer is aligned along the stable easy axis. This will overcome the less stable 150° angle of the top half. However, thermal fluctuations are able to partially drive the domain wall, providing a small probability that the domain wall will propagate downwards.

Figure 5.6 shows forty independent runs for these starting angles, with a different starting seed. The vast majority of the simulations show that the domain wall propagates up from the central position, as the averaged magnetisation of the free layer approaches $M_z = 1$.

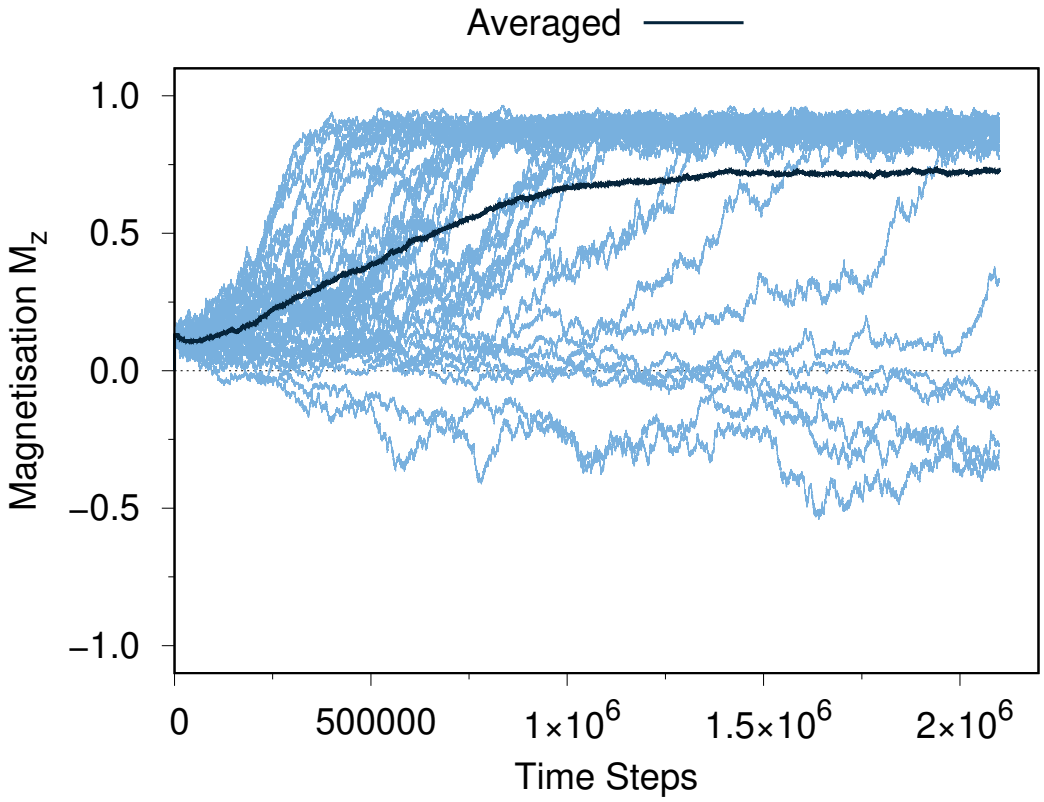

Fig. 5.6 The evolution of the M_z for forty independent simulation with a starting condition of $\theta = 150^\circ$ and $\phi = 0^\circ$ at 300 K. The majority of the runs follow the same path, but with thermal fluctuations some unique pathways are followed. The averaged data is what is used in this chapter.

The averaged magnetisation of the whole free layer will not reach $M_z = 1$ since the top layer is constrained to 150° so at least a small number of layers will not completely align along the easy axis. Importantly, several of the simulations are found to follow unique paths whereby the final averaged magnetisation of the free layer is closer to $M_z = 0$ demonstrating the domain wall has remained towards the middle of the free layer. Similarly, some of the simulations ended with $M_z < 0$ suggesting the domain wall has propagated downwards towards the bottom of the free layer.

To demonstrate this effect, three of the starting seeds were selected from Figure 5.6 and snapshots were produced every 100000 Monte Carlo steps. In Figure 5.7 a), one of the starting seeds that follows the modal path towards a final state of $M_z \approx 0.9$ is chosen. There is clearly a handful of layers at the top of the stack that are stuck at around 150° as they are coupled via exchange with the constrained monolayer. In Figure 5.7 b) one of the seeds that stays around an $M_z = 0$ was chosen. There is a small amount of movement in the domain wall, but it largely stays in the central position. Finally, in Figure 5.7 c) one of the seeds that

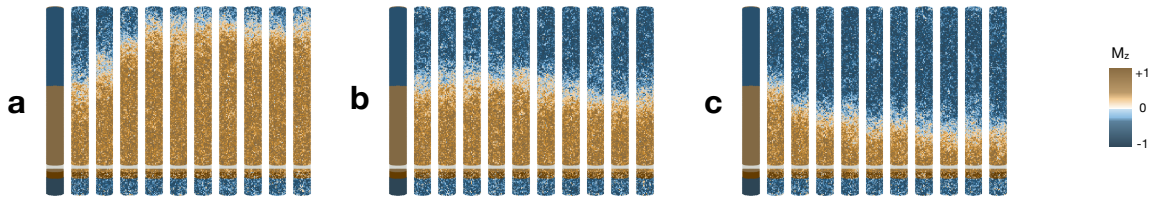

Fig. 5.7 Snapshots of the evolution of the free layer every 100000 Monte Carlo steps at 300 K when starting conditions are $\theta = 150^\circ$ and $\phi = 0^\circ$. In a) the domain wall propagates upwards, as most of the forty runs did in Figure 5.6. In b) the domain wall stays roughly central and in c) the domain wall propagates towards the bottom.

drives the domain wall down was chosen. Similarly to a), the domain wall does not propagate all the way down, as the monolayer at the bottom is constrained at $\phi = 0$. As discussed in chapter 2, the bottom monolayer in these tower structures is enhanced with a larger exchange energy and uniaxial anisotropy term. This produces a slightly larger number of layers that are unable to reverse at the edge when compared to a).

The purpose of Figure 5.6 and Figure 5.7 was to highlight the importance of averaging at finite temperature. Increased thermal fluctuations leads to more possible pathways for the domain wall motion to transition over the energy barrier. It was also worth considering if a larger number of Monte Carlo steps would reduce the number of evolution's that vary from the average. It was not obvious, for example, that with more Monte Carlo steps, more of the plots would eventually converge towards the model M_z. Figure 5.8 shows one of the runs from Figure 5.6 whereby the domain wall stayed roughly central. However, in this plot the number of Monte Carlo steps was increased to 10000000 to see if it eventually converged on the upper M_z. The M_z values stays around $M_z = 0$ for a large number of steps, and eventually begins to propagate down the stack.

This is useful insight and demonstrates how essential averaging is for finite temperature. This shows that the domain wall has a small chance of propagating the opposite way to what is expected at 0 K due to thermal transitions over the energy barrier.

5.2.3 Results

The results presented in this section follow the same process as those presented in subsection 5.1.2. This allows direct comparison between the two approaches to incoherent reversal. Similarly, the results in this section are compared to those expected from experimental and micromagnetic studies. Firstly, the averaged z-component of the magnetisation for the free layer as function of the constraint angle at 300 K is presented in Figure 5.9. This is the average of both halves

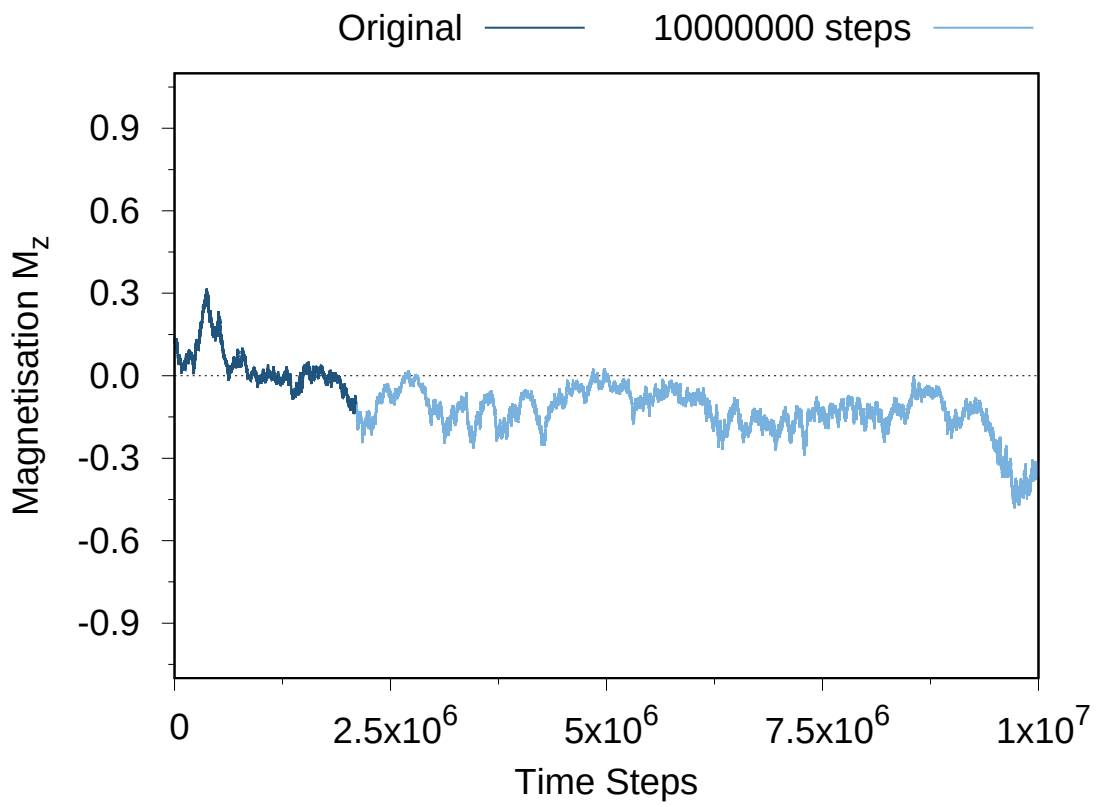

Fig. 5.8 This is one of the central plots in Figure 5.6 extended to 10000000 Monte Carlo steps to demonstrate that it remains at this position. Performing this many steps per simulation would not be possible, and this shows that it would not eliminate this effect.

of the free layer after the 2000000 Monte Carlo steps has completed at it has reached its final state. To clarify, the angle from the easy axis now spans up to 360° because it is the sum of $\theta + \phi$. Therefore, the first 180° shows the magnetisation of the free layer while the top monolayer rotates through 180°, while $\phi = 0$. For the latter half of the graph, $\theta = 180°$ while ϕ is rotated through 180°.

The magnetisation curves follow the expected trend. While the constrained monolayer at the top of the stack is rotated through θ, the rest of the top half of the free layer is initialised along the constraint angle. Under these circumstances, the domain wall has a tendency to propagate upwards as the free layer aligns along the positive easy axis. However, the smaller the tower, the lower the constraint angle needs to be to resist becoming completely aligned along the easy axis. For the 8 nm free layer, one monolayer constrained at an angle from the easy axis becomes significant. This prevents the top few layers of the free layer from aligning with the easy axis, as was seen in Figure 5.7 a). Since these few layers are a much larger relative portion of the whole volume for such small dimensions, the magnetisation is found

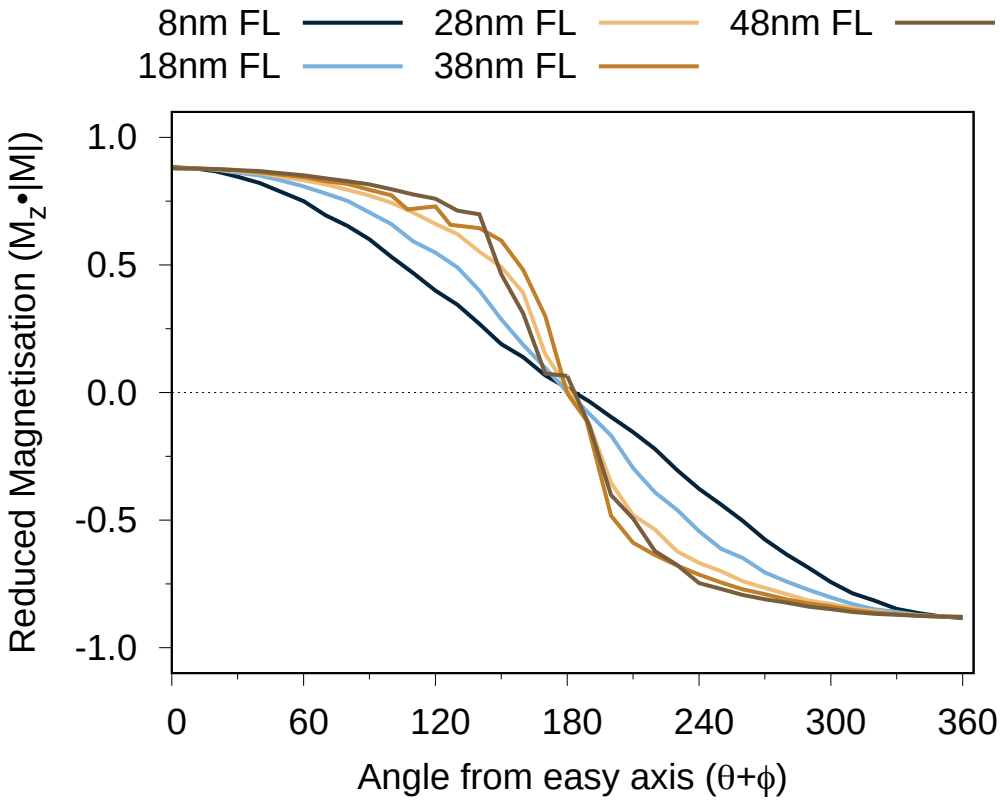

Fig. 5.9 The average magnetisation of the free layer against the sum of the top and bottom constraint angle $\theta + \phi$. First, θ rotates through 180° while $\phi = 0$. Then, ϕ rotates through 180° while $\theta = 180$.

to decrease steadily with constraint angle. In contrast, as the free layer thickness increases, the relative impact of these few layers is lessened when averaging the whole free layer. The magnetisation is therefore seen to reduce by a smaller amount at small constraint angles.
As the constraint angle approaches 180° for the top monolayer, the domain wall that is forced in has a tendency to stay central. This is seen as the $M_z \approx 0$ at such large angles. This is a consequence of this method design, whereby each half of the free layer starts aligned with the respective monolayer. As the starting conditions for the top half starts at angles approaching 180° the two halves of the free layer approach perfectly anti-aligned. It is then not energetically favourable to propagate the domain wall in one direction over the other.
Once $\theta = 180°$, the bottom half of the free layer is then rotated along with the constrained monolayer at the bottom (constrained at angle ϕ). This angle rotation is then roughly symmetrical with the top halves rotation. At smaller angles of ϕ ($180° \leq \theta + \phi \leq 210°$) the domain wall begins to propagate down through the stack. This is the reverse of the low θ constraint angles, since the top half of the free layer will now be initialised along the negative

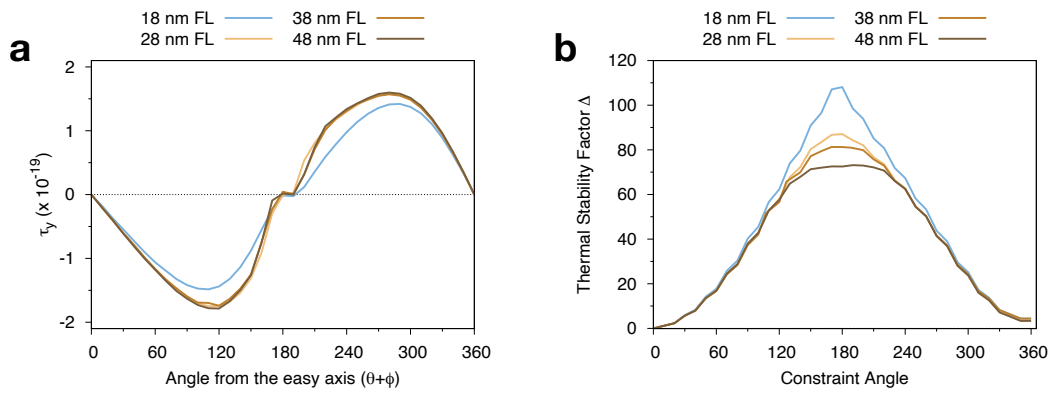

Fig. 5.10 a) the difference in the y-component of the restoring torque for the two constrained monolayers ($\tau_\theta - \tau_\phi$) as a function of constraint angle at 300 K and b) the thermal stability factor obtained by integrating a) and dividing by k_BT.

easy axis. Again, the domain wall is unable to propagate the whole way down the free layer, since the constrained angle will exert torque on its nearest neighbours. Once again this has a larger effect on the 8 nm free layer, which is the reason for the smoother elongated plots compared to taller towers.

The y-component of the restoring torque as a function of the constraint angle is presented in Figure 5.10 a). Since this method consists of two constrained layers, the restoring torque is actually the difference between the torque on the top monolayer and the bottom monolayer. The torque is thus $\tau_\theta - \tau_\phi$ at each constraint angle. The 8 nm free layer is rejected from this point onwards, because the thermal stability calculated was an order of magnitude too large. This is expected, as forcing a domain wall into a free layer of those dimensions requires a significant amount of energy.

Integrating the torque curves in Figure 5.10 a) and dividing by k_BT produces the thermal stability curves seen in Figure 5.10 b). These results show the thermal stability factor decreasing as the free layer thickness increases. This is not expected, since the shape anisotropy increases with growing free layer thickness. This unusual prediction is due to forcing the domain wall into the free layer at the exact halfway point. For all height towers, the maximum thermal stability is found when the domain wall is in the center of the free layer. For the 18 nm free layer, this results in 9 nm of the top half magnetised in an opposing direction to the 9 nm of the bottom half. 9 nm is smaller than a whole domain wall for theses towers (which was estimated in chapter 3 to be around 15nm). This may explain the thermal stability factor being so unexpectedly large for this tower. As the free layer increases, the thermal stability reduces, likely towards a more accurate result. The thermal stability factor for the 48 nm free layer is similar to that found in micromagnetic and experimental results at 300 K [138].

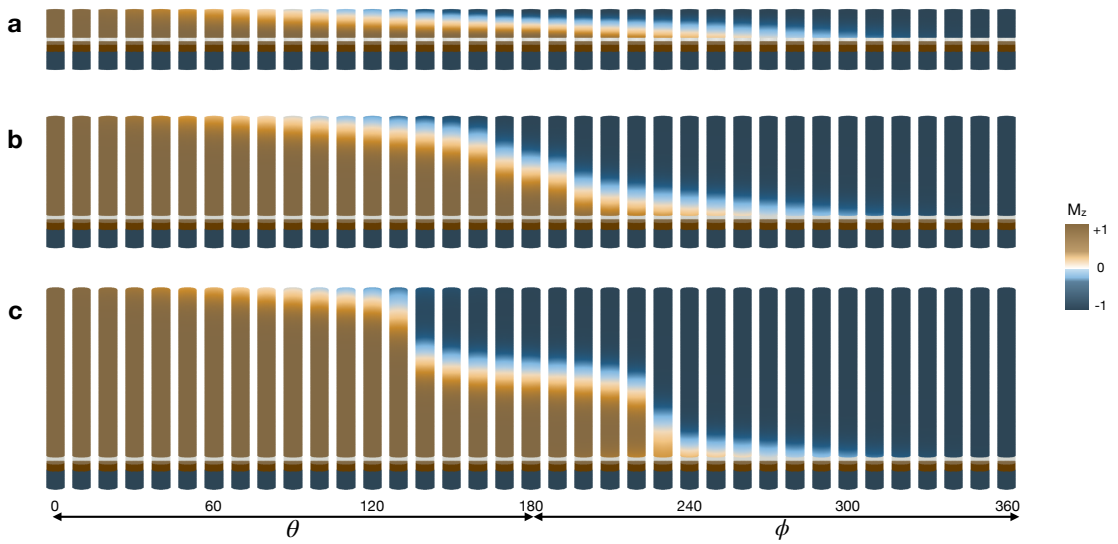

Fig. 5.11 Snapshots of the final magnetic state at 0 K for the each sequential constraint angle for the a) 8 nm free layer, b) 28 nm free layer and c) 48 nm free layer.

There is also a notable change in shape for the thermal stability curves as the free layer thickness is increased. The peak tends to get broader as the free layer thickness increases. For context, while the 8 nm free layer was omitted from this data for being far too large, it was very close to triangular shaped. This is slightly more extreme than the 18 nm, which has a very small width at its peak. This can be compared to the torque curves in Figure 5.10 a), whereby the curves are seen to flatten around constraint angles of $\theta = 180$, $\phi = 0$. To better see what is going on, snapshots of the reversal process at these starting constraints are required.

Snapshots of the final magnetic states of the free layers at each sequential constraint angle are presented in Figure 5.11 a),b) and c) for the 8 nm, 28 nm and 48 nm free layer respectively. The first observation, is that all three free layer thicknesses display partial reversal at the top of the stack at the same angle constraints. That is, when $70^\circ \leq \theta \leq 130^\circ$ ($\phi = 0$) the small amount of reversal at the top of the stack is very similar for all heights. Similarly, the small residue resistance to complete reversal after the majority of the stack is reversed is very similar in the range $60^\circ \leq \phi \leq 120^\circ$ ($\theta = 180$). This is reflective of the identical start and end of the torque curves and thermal stability curves presented in Figure 5.10. The difference between the free layer occurs between this range, for $\theta \geq 130$ and $\phi \leq 60$.

The 8 nm free layer shown in Figure 5.11 a) is found to propagate a domain wall with each subsequent snapshot, which would be expected to require a large amount of energy. It is not the natural state for these dimensions, but it is worth noticing that the energy barrier for this tower are an order of magnitude larger than expected. The constrained layer at the

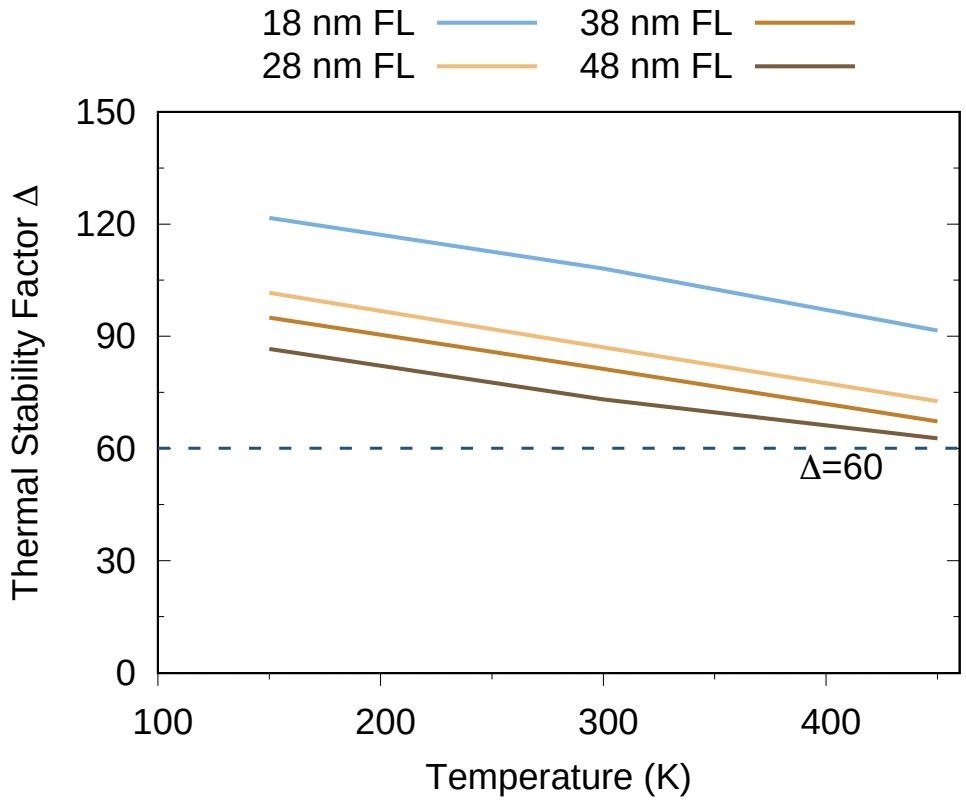

Fig. 5.12 The calculated thermal stability factor as a function of temperature. This approach predicts the thermal stability factor is larger than the industry requirements at these dimensions. This is most likely an overestimate.

bottom of the stack prevents the free layer from simply reversing completely at a critical constraint angle, which is the energetically favourable evolution naturally. Similarly, the 28 nm free layer shown in Figure 5.11 b) shows a propagated domain wall with each subsequent snapshot. In particular, this is in contrast to the 48 nm free layer shown in Figure 5.11 c). In this case, the domain wall stays centrally in the free layer during multiple snapshots. For a span of several starting constraint angle combinations, it is energetically favourable to keep a domain wall in the centre of the stack, rather than propagation. This explains the broadening of the peak in Figure 5.10 b) for the tallest tower. This is closer to what is expected in these results, whereby the the taller towers should reach a peak in thermal stability once a domain wall is inserted and this should be fairly steady through propagation. This also supports the thermal stability factors for the taller towers being close to those found experimentally, whereas the smaller towers are too high in this method.

Finally, the trend of the thermal stability factor as a function of temperature is presented in Figure 5.12. With increasing temperatures, the trend appears consistent, with all free layer

dimensions suffering from a linear reduction in thermal stability. These results predict that all of the taller towers would have sufficient thermal stability to meet industry requirements at operational temperature ranges. Further, at any given temperature, the thermal stability decreases with increasing free layer thickness. This is explained as a consequence of the method design, but is not desirable and the calculated thermal stability at each point can't be taken to predict reality. The tallest tower is in good agreement with experimental and micromagnetic predictions, but this does not validate the method since all other towers disagree.

5.3 Coherent Reversal

A final method, is to force a coherent reversal into the free layer, rather than a domain wall. This reversal mechanism is what was found found for the 8 nm free layer. This alternative method is therefore important to obtain the thermal stability factor for the 8 nm free layer.

5.3.1 Method

With this method, a monolayer at the top of the free layer is constrained with the constrained Monte Carlo method, while the rest of the free layer evolves with the adaptive Monte Carlo method. However, in this case, the bulk of the free layer starts aligned with the constrained layers at each angle. As with the incoherent method, each run is averaged over forty independent simulations due to thermal fluctuations. All results are equilibrated for 100000 Monte Carlo steps, then statistics are taken over the 2000000 further Monte Carlo steps.
An alternative method would be to constrain the whole free layer, however this is computationally expensive for the taller free layers due to the number of atomic sites. For the 8 nm free layer, which is the motivation for this section, constraining the whole free layer is possible. This gave identical thermal stability factors to the method outlined above for the 8 nm free layer. For this reason, the computationally viable method of constraining a monolayer at the top of the stack is used.

5.3.2 Results

These results follow the exact same procedure as in subsection 5.1.2 for direct comparison. Firstly, the averaged z-component as a function of the constraint angle at 300 K is presented in Figure 5.13. The focus is the 8 nm free layer, which follows a characteristic coherent reversal shape. As the angle of the constrained angle increases, the magnetisation smoothly

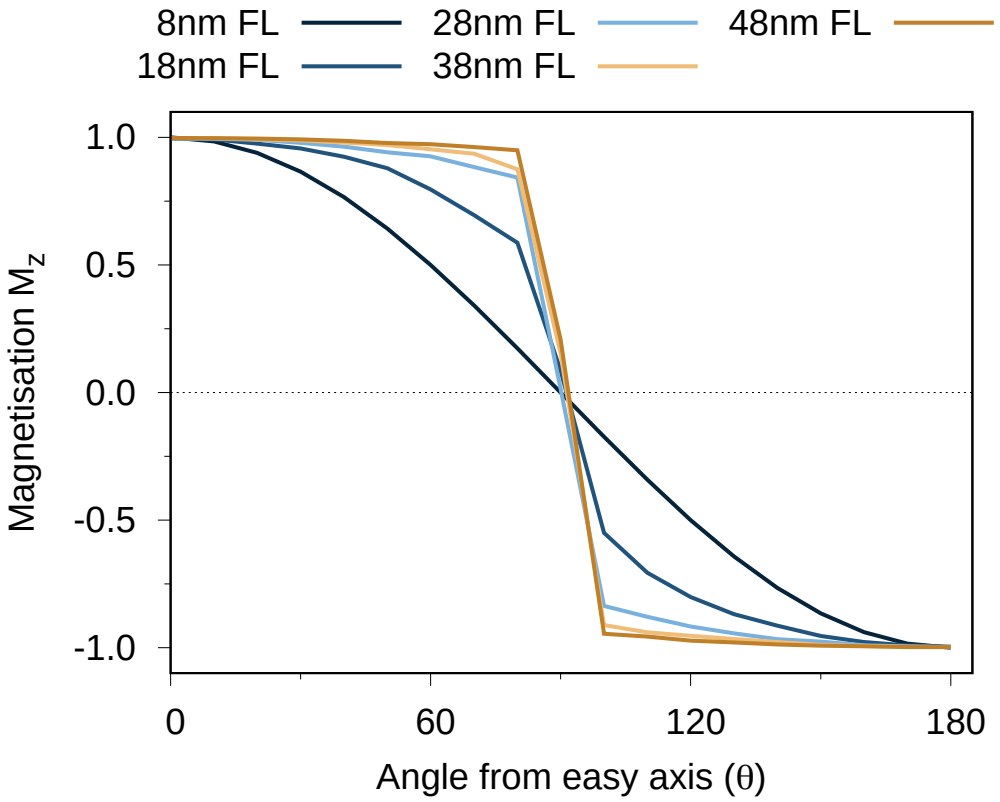

Fig. 5.13 The Magnetisation of the non-constrained bulk of the free layer against the constraint angle of the constrained monolayer. The 8 nm free layer is the focus and follows a characteristic coherent reversal shape.

transitions from $M_z = 1$ to $M_z = -1$. The bulk of the free layer starts off aligned with the constraint angle, but is free to evolve (it is not constrained). However, at these dimensions the bulk of the free layer appears to remain aligned with the constrained layer. This is the tendency of coherent reversal that the 8 nm free layer has demonstrated throughout this work. The taller free layers are not as smooth as the free layer does not remain aligned with the constrained monolayer. For constraint angles $< 90°$, the free layer will evolve back to its nearest resting magnetisation direction which is $M_z = 1$. This is the lowest energy state for the free layer to be in for such large shape anisotropy along the z-axis. Similarly, when the constraint angle is $> 90°$, the free layer will then evolve to the $M_z = -1$ magnetisation direction. For the tallest three towers, this is a sharp transition, whereas the 18 nm free layer has less shape anisotropy. For this reason, at smaller constraint angles, the 18 nm free layer stays closer to a limbo magnetisation, rather than aligning along the easy axis.

As before, it was useful to include the magnetisation plot to better understand the torque curves. Again, the restoring torque as a function of the constraint angle are presented in

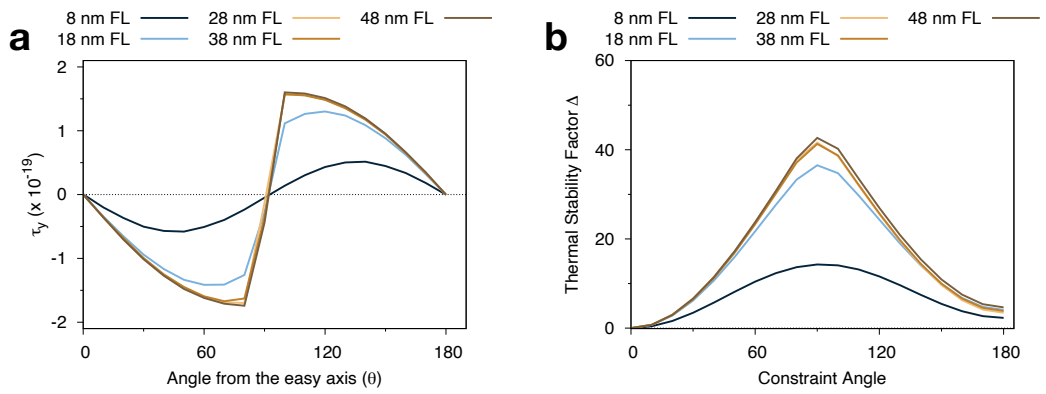

Fig. 5.14 a) the restoring torque of the constrained layer versus the constraint angle and b) the thermal stability factor as a function of constrained angle. Obtained by integrating a) and dividing by k_BT.

Figure 5.14 a). Integrating these curves and dividing by k_BT produces the thermal stability curves shown in Figure 5.14 b).

The torque curves are as expected, with the 8 nm free layer following a smooth and almost symmetric curve with a lower magnitude than the taller free layers. The bulk of the free layer is roughly aligned with the constrained layer, rotating coherently. The torque is therefore expected to be relatively low. As with the incoherent data, the torque flips sign after the halfway point as the free layer transitions from $M_z = 1$ to $M_z = -1$.

In contrast, the taller free layer have much larger torques due to the bulk of the free layer aligning along the easy axis and not with the constrained layer. Once the angle is large enough to flip the free layer magnetisation from $M_z = 1$ to $M_z = 1$, the torque then suddenly flips sign. Theses plots are also roughly symmetric. None of the free layer thicknesses are perfectly symmetric and this is due to two main contributions. Firstly the stray field from the other layers give the free layer a small tendency to align with the reference layer as discussed in chapter 3. Secondly, the monolayer in contact with the MgO at the bottom of the free layer has an enhanced exchange constant and uniaxial anisotropy constant. Since this monolayer also suffers from the stray field and has a preference to align, this has a larger effect on its nearest neighbours than the monolayer at the top of the free layer.

The thermal stability factor as a function of the constraint angle are presented in Figure 5.14 b). Much like the taller free layer in section 5.2, the 8 nm free layer is in good agreement with Perrissin et. al. [138]. At 300 K, both this study and the work of Perrissin et. al. find the thermal stability of the 8 nm free layer to be between $10-20$.

Comparison of the taller towers in Figure 5.14 b) and Figure 5.3 b) demonstrates a significant difference. When subjected to incoherent motion via a propagated domain wall, the thermal stability factors are much higher for the taller towers. When subjected to a coherent reversal,

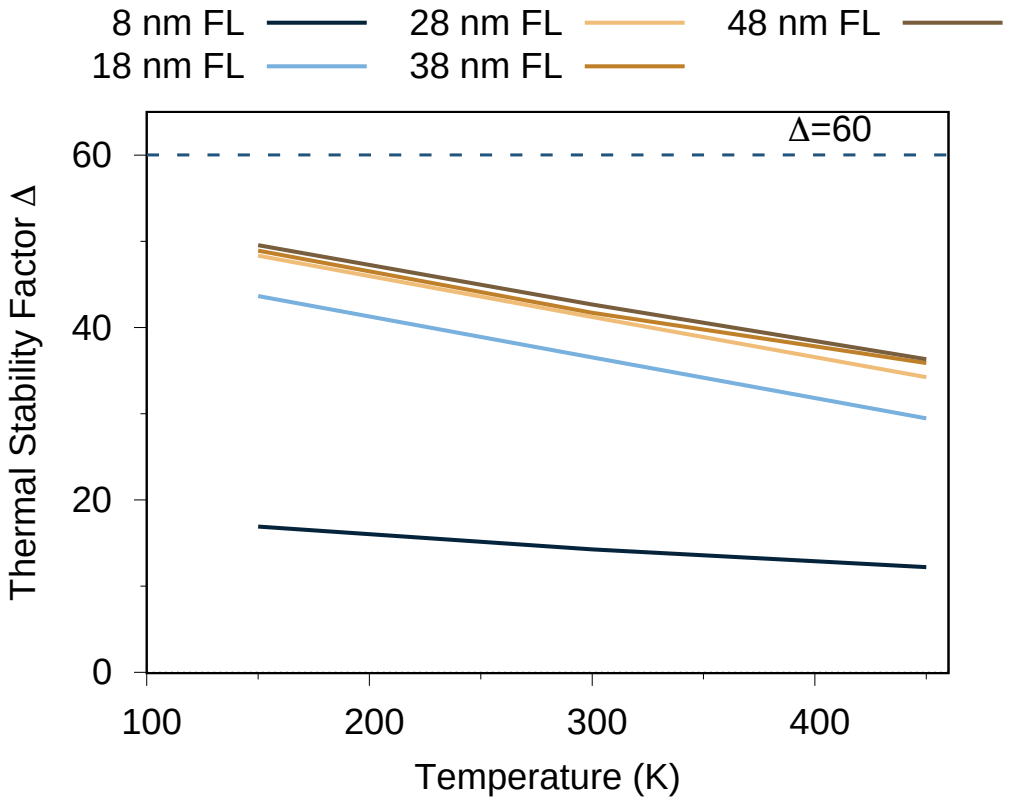

Fig. 5.15 The thermal stability of the free layer against temperature for the coherent reversal. All free layers are below the industry target.

the thermal stability is found to reach just over $\Delta = 40$ for the tallest towers. Given how well the results agree with other studies under the incoherent regime, these thermal stabilites should not be taken as true for these dimensions.

Finally, this process is repeated at 150 K and 450 K to explore the trend of the thermal stability with temperature under the coherent regime. This is presented in Figure 5.15 and again includes the industry target of $\Delta = 60$ for context. Under the coherent regime, the tallest free layers do not reach the minimal threshold, in contrast with the results found in section 5.2. These results are rejected for the free layer of 18 nm or larger thickness.

The 8 nm free layer is also significantly below the industry target, but this is in strong agreement with Perrissin [138]. At these dimensions, the shape anisotropy is too low for appropriate data retention. These results suggest PSA-MRAM of these dimensions would not satisfy the requirements and would not be worth pursuing.

5.4 Summary

In this chapter, the thickness and temperature dependence of the energy barrier was explored for PSA-MRAM structures using the constrained Monte Carlo method. Free layers of thickness 18 nm, 28 nm, 38 nm and 48 nm are known to undergo incoherent reversal mechanisms with a propagated domain wall. These four free layers were explored using two methods for incoherent reversal. The first method is referred to as the nucleation method and forces a domain wall at the top of the free layer. This method is proposed to be the better method if the bulk of the free layer does not start aligned along the easy axis every time. Using a checkpoint method to feed the final state of one constraint into the starting position of the subsequent constraint is expected to give improved results. This study did not have time to utilise this improvement, and the subsequent predictions for the thermal stability should be discarded. A second method referred to as the double constraint method was then presented, whereby a monolayer at the top and bottom of the free layer are constrained, while the bulk is free to evolve. The top half always starts aligned with the top monolayer, and the bottom half aligns with the bottom monolayer, inserting a domain wall at sufficient angles. This method overestimates the smaller towers significantly, due to the forced domain wall insertion being smaller than the actual domain wall for these towers. For sufficiently high towers, this method does seem to improve, showing good agreement with other studies for the 48 nm free layer. However, these results too should be discarded and as this method does not produce appropriate energy barriers. Finally, a coherent method was presented for the 8 nm free layer, which showed good agreement with experimental studies. This method is appropriate for towers that display coherent reversal, but underestimates the thermal stability for towers that undergo incoherent reversal. Given the failures of the two incoherent methods at this stage, only the 8 nm free layer thermal stability is believed to have been captured, and is too small to meet industry requirements at all temperatures.

6

Conclusions and Further Work

This final chapter will outline the main conclusions of this thesis, identifying the key results found. It will subsequently outline further work that could be undertaken to develop the work of this thesis further. This whole thesis utilised an atomistic spin model. This model choice is significant for two main reasons. Firstly it is able to capture finite size and edge effects which have been found to be hugely significant for PSA-MRAM. Additionally, thermal effects, which are shown to be hugely important for the intricate behaviours of nanoscale devices, are a motivation for this model. First, the magnetic properties and reversal behaviour of PSA-MRAM structures of 5 nm diameter and varying free layer thickness were explored when subjected to a magnetic field. Then, the reversal of these structures was further explored using STT in place of a magnetic field.

6.1 Thermodynamic Properties and Switching Mechanisms of PSA-MRAM

The purpose of chapter 3 was to explore the thermodynamic properties and switching mechanics for the PSA-MRAM design using an atomistic model. It was shown that for a 5 nm diameter device, the shape anisotropy in the free layer plateaus when the thickness is increased to 30 nm. Increasing the free layer further does not provide any additional thermal stability to this design. This was supported with plots of the susceptibility, which found uniform magnetisation modes in the 8 nm free layer, but evidence of non-uniform magnetisation modes as the free layer increases. The importance of thermal fluctuations was highlighted by the hysteresis data, which showed a significant switching field distributions with increasing temperature. For these systems, the thermal fluctuations at operational temperatures are capable of partially driving the reversal mechanism. Further, by extracting

the coercivities at $0K$ our atomistic model was compared to the analytical Sharrock model. There was good agreement at 0 K, further suggesting the plateauing of thermal stability beyond 30 nm free layer thickness at these dimensions. Finally, the reversal mechanism was explored for different free layer thicknesses. Both at $0K$ and finite temperature, a free layer of 8 nm thickness displays coherent rotation. All taller towers in this study have transitioned to an incoherent reversal mechanism propagated by a domain wall.
Due to computation time, this study only explored PSA-MRAM structures with a diameter of 5 nm. Further study should include larger diameters to span a range of PSA-MRAM designs. Tower structures as thin as 8 nm have been reported experimentally, so it would be useful to span up to at least this diameter. Structures with larger numbers of atomic sites have been done on previous perpendicular MRAM studies, so are achievable. Further, this study model the tower structures as smooth cylinders, with key magnetic parameters assigned to each layer assumed to be constant throughout the layer. Further insight into the fabrication and growth process would provide more accurate tower structures. Particular details would be the deviation from a perfect cylinder that is found experimentally during the fabrication process. It has been shown that during the manufacture of such nanoscale devices, there is a ballooning effect at material boundaries whereby the width increases. Similarly, any damage or warping to the crystal structure, and any impurities, would have an effect on the coercivity. This are unavoidable experimental defects during the lithography and annealing process.

6.2 Dynamics of STT-PSA-MRAM

The purpose of chapter 4 was to explore the reversal mechanism of the PSA-MRAM structured free layer subjected to a STT mechanism. It is important to explore how this phenomena impacts the reversal mechanism for these structures. Again, the inclusion of thermodynamic effects is significant, as the reversal mechanism was found to depend on both thermal fluctuations and the current density. First the effect of the spin torque upon the reversal mechanism in the absence of temperature was presented. The smallest tower was still found to be coherent, but the incoherent reversal of the taller towers was complicated. At lower current density, the spin accumulation can travel through the whole free layer and build at the top of the stack. This occurs before a sufficient spin accumulation is built at the bottom of the free layer, leading to partial reversal at both sides. These fluctuations can inhibit the propagation of the domain wall in the smaller towers, while the taller towers suffer less from this. At higher current densities the domain wall can propagate from the bottom of the stack before this effect can begin. In the absence of temperature, only the 18 nm was found to suffer from any significant hindrance of the domain wall. The taller towers had sufficient

shape anisotropy that impact from the top is minimised. The inclusion of temperature was subsequently found to exaggerate this behaviour. Particularly, the next tallest tower with a 28 nm free layer was found to become affected. This was because the thermal fluctuations can drive the partial reversal at the top of the stack further into the free layer, inhibiting the domain wall.

This work could also be furthered in the same way as chapter 3, with larger diameters and attention to manufacturing defects. These suggestions are outlined above and are not discussed again here. Instead, an additional improvements for this study would be the inclusion of a spin orbit torque (SOT) reversal mechanism, and subsequently a combination of STT and SOT. This would be very interesting, as PSA-MRAM with SOT is a possible candidate for fast cache memory. Further, modelling a combination of STT and SOT for the disc structures of perpendicular MRAM design with STT and SOT have been reported. Direct comparison of those structures with the tower like structures of PSA-MRAM would be an interesting development.

6.3 Calculation of the Energy Barrier for PSA-MRAM Using the Constrained Monte Carlo Method

PSA-MRAM must display a data retention rate of a minimum of 10 years to satisfy industry requirements. A key parameter for this requirement, is the energy barrier, which divided by k_BT provides the dimensionless thermal stability factor Δ. In line with industry requirements, the thermal stability factor must be a minimum of $\Delta = 60$. It is of high importance, therefore, to find the thermal stability for the PSA-MRAM devices studied in this thesis. The purpose of chapter 5 was to attempt to calculate the energy barrier and thus the thermal stability factor for the dimensions studied in this thesis. While appropriate methods were not completed in time to reliably produce these values, several approaches were explored and the subsequent failures of these approaches were outlined.

Firstly, for towers that display evidence of incoherent reversal, two methods were attempted. The first constrains several layers at the top of the free layer with the constrained Monte Carlo method. The rest of the free layer is allowed to evolve using the adaptive Monte Carlo method. The hope, was that this would force a domain wall into the free layer that will propagate downwards. This method is referred to as the nucleation method in this work. By plotting the angular dependence of the torque and then integrating, the energy barrier is obtained. However, given computational limitations, this method is much faster if the non-constrained section of the free layer is initialised along the easy axis. However, for free

layer of thickness greater than 18 nm, the constrained layers do not provide sufficient torque on the non-constrained layer to produce the expected reversal at appropriate constraint angles. Subsequently, plotting the restoring torque showed that this method was not reliable and producing physically unreasonable evolution's.

The second method to attempt to calculate the thermal stability in incoherent free layers was a two constraint method. A single layer at the top and the bottom of the free layer were constrained, while the rest was non-constrained. The top half of the free layer started aligned with the top constraint, while the bottom half started aligned with the bottom constraint. Thus, by rotating the top half first, then the bottom half, a domain wall was forced into the centre of the stack. This method seemed to produced more reasonable predictions for the thermal stability factor as the free layer increased in thickness. By 48 nm, the thermal stability factor calculated at room temperature was in good agreement with other literature. However, for smaller free layers, this method massively overestimated the thermal stability factors. It was still worth exploring these two methods, as clearly the choice of the constraint will provide different answers. The lessons learnt will provide a more informed choice for future study into the thermal stability of PSA-MRAM.

Finally, the coherent reversal was also presented, which consists of constraining a monolayer at the top and the bottom of the free layer, while the rest of the free layer is free to evolve. The difference, is the the bulk of the free layer starts aligned with the two constrained layers, which are always equal. This creates a coherent like starting position, though the free layer can then evolve. This method was successful for the 8 nm free layer, showing very good agreement with experimental studies. This method does not work for taller towers, however, where it massively underestimates the thermal stability factor compared to other literature.

Further work on this chapter is currently ongoing for the nucleation method. It was outlined in this chapter, that while the nucleation method failed in its current state, it is likely salvageable by using a check pointing method. With this method, each constraint angle must be run one at a time. The final magnetic state of the constraint is then used as the starting condition for the next constraint angle. This is in contrast to the current method, whereby the non-constrained free layer was always initialised along the easy axis. This check pointing method could not be achieved in time for this thesis, due to its heavy computational requirements. Each constrained angle takes significant resource and time, such that doing one after the other to range through 180° would take several weeks per temperature. This is expected to provide significantly improved thermal stability factors much closer to experimental findings.

As with the other chapters, exploring other dimensions and shapes would also be useful further work. The thermal stability factor (or the energy barrier) are hugely significant for design and represent a significant test of a devices potential reliability/validity. It would also

be interesting to further this study with applied fields, whereas all of this chapter is in the absence of a field. A field will directly impact the reversal mechanism as found in chapter 3, which will change the energy barrier of the system.

References

[1] Muhammad Usman Ashraf, Fathy Alboraei Eassa, Aiiad Ahmad, and Abdullah Algarni. Empirical investigation: performance and power-consumption based dual-level model for exascale computing systems. *IET Software*, 14(4):319–327, August 2020.

[2] Marcin Pospieszny. Electricity in hpc centres. *Zenodo*, 2017.

[3] Woong Shin, Vladyslav Oles, Ahmad Maroof Karimi, J. Austin Ellis, and Feiyi Wang. Revealing power, energy and thermal dynamics of a 200pf pre-exascale supercomputer. In *Proceedings of the International Conference for High Performance Computing, Networking, Storage and Analysis*, SC '21. ACM, November 2021.

[4] Xun Jian, Pavan Kumar Hanumolu, and Rakesh Kumar. Understanding and optimizing power consumption in memory networks. In *2017 IEEE International Symposium on High Performance Computer Architecture (HPCA)*. IEEE, February 2017.

[5] Aniruddha N. Udipi, Naveen Muralimanohar, Niladrish Chatterjee, Rajeev Balasubramonian, Al Davis, and Norman P. Jouppi. Rethinking dram design and organization for energy-constrained multi-cores. In *Proceedings of the 37th annual international symposium on Computer architecture*, ISCA '10. ACM, June 2010.

[6] Bharan Giridhar, Michael Cieslak, Deepankar Duggal, Ronald Dreslinski, Hsing Min Chen, Robert Patti, Betina Hold, Chaitali Chakrabarti, Trevor Mudge, and David Blaauw. Exploring dram organizations for energy-efficient and resilient exascale memories. In *Proceedings of the International Conference on High Performance Computing, Networking, Storage and Analysis*, SC13. ACM, November 2013.

[7] Ivy Peng, Ian Karlin, Maya Gokhale, Kathleen Shoga, Matthew Legendre, and Todd Gamblin. A holistic view of memory utilization on hpc systems: Current and future trends. In *The International Symposium on Memory Systems*, MEMSYS 2021. ACM, September 2021.

[8] Michael Fowler. *Historical Beginnings of Theories of Electricity and Magnetism*, chapter 1. University of Virginnia, Physics, 1997.

[9] R Skomski. Nanomagnetics. *Journal of Physics: Condensed Matter*, 15(20):R841–R896, May 2003.

[10] Ernst Ising. Beitrag zur theorie des ferromagnetismus. *Zeitschrift für Physik*, 31(1):253–258, February 1925.

[11] Albert Fert. Origin, development, and future of spintronics (nobel lecture). *Angewandte Chemie International Edition*, 47(32):5956–5967, July 2008.

[12] Supriyo Bandyopadhyay and Marc Cahay. *Introduction to Spintronics*. CRC Press, March 2008.

[13] Igor Žutić, Jaroslav Fabian, and S. Das Sarma. Spintronics: Fundamentals and applications. *Reviews of Modern Physics*, 76(2):323–410, April 2004.

[14] M. Julliere. Tunneling between ferromagnetic films. *Physics Letters A*, 54(3):225–226, September 1975.

[15] T. Miyazaki and N. Tezuka. Giant magnetic tunneling effect in fe/al2o3/fe junction. *Journal of Magnetism and Magnetic Materials*, 139(3):L231–L234, January 1995.

[16] J. S. Moodera, Lisa R. Kinder, Terrilyn M. Wong, and R. Meservey. Large magnetoresistance at room temperature in ferromagnetic thin film tunnel junctions. *Physical Review Letters*, 74(16):3273–3276, April 1995.

[17] Shinji Yuasa, Taro Nagahama, Akio Fukushima, Yoshishige Suzuki, and Koji Ando. Giant room-temperature magnetoresistance in single-crystal fe/MgO/fe magnetic tunnel junctions. *Nature Materials*, 3(12):868–871, oct 2004.

[18] Stuart S. P. Parkin, Christian Kaiser, Alex Panchula, Philip M. Rice, Brian Hughes, Mahesh Samant, and See-Hun Yang. Giant tunnelling magnetoresistance at room temperature with MgO (100) tunnel barriers. *Nature Materials*, 3(12):862–867, oct 2004.

[19] Y. M. Lee, J. Hayakawa, S. Ikeda, F. Matsukura, and H. Ohno. Effect of electrode composition on the tunnel magnetoresistance of pseudo-spin-valve magnetic tunnel junction with a mgo tunnel barrier. *Applied Physics Letters*, 90(21), May 2007.

[20] Dmytro Apalkov, Bernard Dieny, and J. M. Slaughter. Magnetoresistive random access memory. *Proceedings of the IEEE*, 104(10):1796–1830, October 2016.

[21] J.C. Slonczewski. Current-driven excitation of magnetic multilayers. *Journal of Magnetism and Magnetic Materials*, 159(1-2):L1–L7, June 1996.

[22] L. Berger. Emission of spin waves by a magnetic multilayer traversed by a current. *Physical Review B*, 54(13):9353–9358, October 1996.

[23] Daniel C. Worledge. Spin-transfer-torque mram: the next revolution in memory. In *2022 IEEE International Memory Workshop (IMW)*. IEEE, May 2022.

[24] S. Aggarwal, K. Nagel, G. Shimon, J. J. Sun, T. Andre, S. M. Alam, H. Almasi, M. DeHerrera, B. Hughes, S. Ikegawa, J. Janesky, H. K. Lee, H. Lu, and F. B. Mancoff. Demonstration of a reliable 1 gb standalone spin-transfer torque mram for industrial applications. In *2019 IEEE International Electron Devices Meeting (IEDM)*. IEEE, December 2019.

[25] G. Hu, D. Kim, J. Kim, C. Kothandaraman, G. Lauer, H K Lee, N. Marchack, M. Reuter, R. P. Robertazzi, J. Z. Sun, T. Suwannasiri, J. J. Nowak, P. L. Trouilloud, S. Woo, D. C. Worledge, M. G. Gottwald, S. L. Brown, B. Doris, C. P. D'Emic, P. Hashemi, D. Houssameddine, and Q. He. Spin-transfer torque mram with reliable 2 ns writing for last level cache applications. In *2019 IEEE International Electron Devices Meeting (IEDM)*. IEEE, December 2019.

[26] Hao Meng and Jian-Ping Wang. Spin transfer in nanomagnetic devices with perpendicular anisotropy. *Applied Physics Letters*, 88(17), April 2006.

[27] S. Mangin, D. Ravelosona, J. A. Katine, M. J. Carey, B. D. Terris, and Eric E. Fullerton. Current-induced magnetization reversal in nanopillars with perpendicular anisotropy. *Nature Materials*, 5(3):210–215, February 2006.

[28] T.L. Gilbert. Classics in magnetics a phenomenological theory of damping in ferromagnetic materials. *IEEE Transactions on Magnetics*, 40(6):3443–3449, November 2004.

[29] R F L Evans. VAMPIRE software package v5 available from https://vampire.york.ac.uk/. *git://github.com/richard-evans/vampire.git*, 2020.

[30] R F L Evans, W J Fan, P Chureemart, T A Ostler, M O A Ellis, and R W Chantrell. Atomistic spin model simulations of magnetic nanomaterials. *J. Phys. Condens. Matter*, 26(10):103202, March 2014.

[31] W. Pauli. Über den zusammenhang des abschlusses der elektronengruppen im atom mit der komplexstruktur der spektren. *Zeitschrift für Physik*, 31(1):765–783, February 1925.

[32] Norbert Straumann. The role of the exclusion principle for atoms to stars: A historical account, 2004.

[33] W. Heisenberg. Zur theorie des ferromagnetismus. *Zeitschrift für Physik*, 49(9-10):619–636, September 1928.

[34] S. Blundell. *Magnetism in condensed matter*, chapter 4. Oxford University Press, 2001.

[35] Alastair I. M. Rae and Jim Napolitano. *Quantum Mechanics*, chapter 13, pages 314–321. CRC press, Taylor and Francis group, sixth edition, 2016.

[36] W. Heitler and F. London. Wechselwirkung neutraler atome und homöopolare bindung nach der quantenmechanik. *Zeitschrift für Physik*, 44(6-7):455–472, June 1927.

[37] O. N Mryasov, U Nowak, K. Y Guslienko, and R. W Chantrell. Temperature-dependent magnetic properties of FePt: Effective spin hamiltonian model. *Europhysics Letters (EPL)*, 69(5):805–811, mar 2005.

[38] Junlin Wang, Mara Strungaru, Sergiu Ruta, Andrea Meo, Yifan Zhou, András Deák, László Szunyogh, Paul-Iulian Gavriloaea, Roberto Moreno, Oksana Chubykalo-Fesenko, Jing Wu, Yongbing Xu, Richard F. L. Evans, and Roy W. Chantrell. Spontaneous creation and annihilation dynamics of magnetic skyrmions at elevated temperature. *Physical Review B*, 104(5), August 2021.

[39] Forschungszentrum Jülich. *Ferienkurse des Forschungszentrums*, chapter 24. Forschungszentrum Jülich GmbH, 1993.

[40] Sarah Jenkins. *Spin Dynamics Simulations of Iridium Manganese Alloys*. PhD thesis, University of York, May 2020.

[41] H. W. Babcock. Zeeman effect in stellar spectra. *The Astrophysical Journal*, 105:105, January 1947.

[42] Edmund C. Stoner. XCVII. the demagnetizing factors for ellipsoids. *The London, Edinburgh, and Dublin Philosophical Magazine and Journal of Science*, 36(263):803–821, dec 1945.

[43] J. C. Maxwell. *A treatise on Electricity and Magnetism*, volume 1. Claredon Press, Oxford, Uk, 1873.

[44] D. J. Griffiths. *Introduction to Electrodynamics*. Pearson Education Limited, 4th edition, 2014.

[45] Sarah Jenkins, Andrea Meo, Luke E Elliott, Stephan K Piotrowski, Mukund Bapna, Roy W Chantrell, Sara A Majetich, and Richard F L Evans. Magnetic stray fields in nanoscale magnetic tunnel junctions. *Journal of Physics D: Applied Physics*, 53(4):044001, November 2019.

[46] E.D. Boerner, O. Chubykalo-Fesenko, O.N. Mryasov, R.W. Chantrell, and O. Heinonen. Moving toward an atomistic reader model. *IEEE Transactions on Magnetics*, 41(2):936–940, February 2005.

[47] B.R.A. Nijboer and F.W. De Wette. The internal field in dipole lattices. *Physica*, 24(1-5):422–431, January 1958.

[48] G J Bowden, G B G Stenning, and G van der Laan. Inter and intra macro-cell model for point dipole–dipole energy calculations. *Journal of Physics: Condensed Matter*, 28(6):066001, jan 2016.

[49] Sutee Sampan-A-Pai, Rattaphon Phoomatna, Worawut Boonruesi, Andrea Meo, Jessada Chureemart, Richard F. L. Evans, Roy W. Chantrell, and Phanwadee Chureemart. Magnetization dynamics at finite temperature in CoFeB–MgO based MTJs. *Scientific Reports*, 13(1), February 2023.

[50] Roberto Moreno, Samuel Poyser, Daniel Meilak, Andrea Meo, Sarah Jenkins, Vlado K. Lazarov, Gonzalo Vallejo-Fernandez, Sara Majetich, and Richard F. L. Evans. The role of faceting and elongation on the magnetic anisotropy of magnetite fe3o4 nanocrystals. *Scientific Reports*, 10(1), February 2020.

[51] Sarah Jenkins and Richard F L Evans. Scalable space and time hierarchical dipole-dipole interactions in the vampire code. *OpenAIRE*, 2020.

[52] Nicholas Metropolis and S. Ulam. The monte carlo method. *Journal of the American Statistical Association*, 44(247):335–341, September 1949.

[53] J. E. Gubernatis. Marshall rosenbluth and the metropolis algorithm. *Physics of Plasmas*, 12(5):057303, May 2005.

[54] Nicholas Metropolis, Arianna W. Rosenbluth, Marshall N. Rosenbluth, Augusta H. Teller, and Edward Teller. Equation of state calculations by fast computing machines. *The Journal of Chemical Physics*, 21(6):1087–1092, June 1953.

[55] John S. Thomsen. Logical relations among the principles of statistical mechanics and thermodynamics. *Physical Review*, 91(5):1263–1266, September 1953.

[56] D. Hinzke and U. Nowak. Monte carlo simulation of magnetization switching in a heisenberg model for small ferromagnetic particles. *Computer Physics Communications*, 121-122:334–337, September 1999.

[57] J D Alzate-Cardona, D Sabogal-Suárez, R F L Evans, and E Restrepo-Parra. Optimal phase space sampling for monte carlo simulations of heisenberg spin systems. *Journal of Physics: Condensed Matter*, 31(9):095802, January 2019.

[58] P. Asselin, R. F. L. Evans, J. Barker, R. W. Chantrell, R. Yanes, O. Chubykalo-Fesenko, D. Hinzke, and U. Nowak. Constrained monte carlo method and calculation of the temperature dependence of magnetic anisotropy. *Physical Review B*, 82(5), August 2010.

[59] Sarah Jenkins, Roy W. Chantrell, Timothy J. Klemmer, and Richard F. L. Evans. Magnetic anisotropy of the noncollinear antiferromagnet irmn_3. *Physical Review B*, 100(22), December 2019.

[60] Richard F. L. Evans, Levente Rózsa, Sarah Jenkins, and Unai Atxitia. Temperature scaling of two-ion anisotropy in pure and mixed anisotropy systems. *Physical Review B*, 102(2), July 2020.

[61] A. Meo, R. Chepulskyy, D. Apalkov, R. W. Chantrell, and R. F. L. Evans. Atomistic investigation of the temperature and size dependence of the energy barrier of CoFeB/MgO nanodots. *Journal of Applied Physics*, 128(7):073905, August 2020.

[62] L. Landau and E. Lifshits. On the theory of the dispersion of magnetic permeability in ferromagnetic bodies. *Phys. Zeitsch. der Sow. 8*, 1935.

[63] M. O. A. Ellis, R. F. L. Evans, T. A. Ostler, J. Barker, U. Atxitia, O. Chubykalo-Fesenko, and R. W. Chantrell. The landau–lifshitz equation in atomistic models. *Low Temperature Physics*, 41(9):705–712, September 2015.

[64] Sutee Sampan a pai, Jessada Chureemart, Roy W. Chantrell, Roman Chepulskyy, Shuxia Wang, Dmytro Apalkov, Richard F. L. Evans, and Phanwadee Chureemart. Temperature and thickness dependence of statistical fluctuations of the gilbert damping in co-fe-b /mgo bilayers. *Physical Review Applied*, 11(4), April 2019.

[65] Satoshi Iihama, Shigemi Mizukami, Hiroshi Naganuma, Mikihiko Oogane, Yasuo Ando, and Terunobu Miyazaki. Gilbert damping constants of ta/CoFeB/MgO(ta) thin films measured by optical detection of precessional magnetization dynamics. *Physical Review B*, 89(17), May 2014.

[66] M. L. Schneider, Th. Gerrits, A. B. Kos, and T. J. Silva. Gyromagnetic damping and the role of spin-wave generation in pulsed inductive microwave magnetometry. *Applied Physics Letters*, 87(7), August 2005.

[67] Yi Liu, Zhe Yuan, R. J. H. Wesselink, Anton A. Starikov, and Paul J. Kelly. Interface enhancement of gilbert damping from first principles. *Physical Review Letters*, 113(20), November 2014.

[68] Ehsan Barati and Marek Cinal. Quantum mechanism of nonlocal gilbert damping in magnetic trilayers. *Physical Review B*, 91(21), June 2015.

[69] W. Brown. Thermal fluctuation of fine ferromagnetic particles. *IEEE Transactions on Magnetics*, 15(5):1196–1208, September 1979.

[70] A Lyberatos, D V Berkov, and R W Chantrell. A method for the numerical simulation of the thermal magnetization fluctuations in micromagnetics. *Journal of Physics: Condensed Matter*, 5(47):8911–8920, nov 1993.

[71] José Luis García-Palacios and Francisco J. Lázaro. Langevin-dynamics study of the dynamical properties of small magnetic particles. *Physical Review B*, 58(22):14937–14958, dec 1998.

[72] U. Nowak, O. N. Mryasov, R. Wieser, K. Guslienko, and R. W. Chantrell. Spin dynamics of magnetic nanoparticles: Beyond brown's theory. *Physical Review B*, 72(17), nov 2005.

[73] D V Berkov and N L Gorn. Thermally activated processes in magnetic systems consisting of rigid dipoles: equivalence of the ito and stratonovich stochastic calculus. *Journal of Physics: Condensed Matter*, 14(13):L281–L287, mar 2002.

[74] Makoto Matsumoto and Takuji Nishimura. Mersenne twister. *ACM Transactions on Modeling and Computer Simulation*, 8(1):3–30, jan 1998.

[75] George Marsaglia and Wai Wan Tsang. The ziggurat method for generating random variables. *Journal of Statistical Software*, 5(8), 2000.

[76] Andrea Meo, Carenza E Cronshaw, Sarah Jenkins, Amelia Lees, and Richard F L Evans. Spin-transfer and spin-orbit torques in the landau–lifshitz–gilbert equation. *Journal of Physics: Condensed Matter*, 35(2):025801, November 2022.

[77] Andrea Meo, Jessada Chureemart, Roy W. Chantrell, and Phanwadee Chureemart. Magnetisation switching dynamics induced by combination of spin transfer torque and spin orbit torque. *Scientific Reports*, 12(1), March 2022.

[78] S. Zhang, P. M. Levy, and A. Fert. Mechanisms of spin-polarized current-driven magnetization switching. *Physical Review Letters*, 88(23), May 2002.

[79] Yuta Yahagi, Daisuke Miura, Akimasa Sakuma, and Jakub Železný. Theoretical study of extrinsic spin current generation in ferromagnets induced by anisotropic spin-flip scattering. *Physical Review B*, 104(9), September 2021.

[80] D.C. Ralph and M.D. Stiles. Spin transfer torques. *Journal of Magnetism and Magnetic Materials*, 320(7):1190–1216, April 2008.

[81] Phanwadee Chureemart. *Models of spin torque using self-consistent solutions of the magnetisation and spin accumulation*. PhD thesis, University of York, August 2015.

[82] Andrea Meo. *Atomistic model of magnetisation dynamics and equilibrium properties of magnetic tunnel junctions*. PhD thesis, University of York, September 2018.

[83] S. Zhang and Z. Li. Roles of nonequilibrium conduction electrons on the magnetization dynamics of ferromagnets. *Physical Review Letters*, 93(12), September 2004.

[84] Jun ichiro Kishine and A. S. Ovchinnikov. Adiabatic and nonadiabatic spin-transfer torques in the current-driven magnetic domain wall motion. *Physical Review B*, 81(13), April 2010.

[85] A. G. Aranov. Spin injection in metals and polarization in nuclei. *JETP*, 24:37–39, 1976.

[86] Mark Johnson and R. H. Silsbee. Interfacial charge-spin coupling: Injection and detection of spin magnetization in metals. *Physical Review Letters*, 55(17):1790–1793, oct 1985.

[87] P M Levy. The role of spin accumulation in current-induced switching of magnetic layers, or the first 10^{-12}s in a magnetic multilayer after the current is switched on. *Journal of Physics D: Applied Physics*, 35(19):2448–2451, September 2002.

[88] Cyril Petitjean, David Luc, and Xavier Waintal. Unified drift-diffusion theory for transverse spin currents in spin valves, domain walls, and other textured magnets. *Physical Review Letters*, 109(11), sep 2012.

[89] P Chureemart, I D'Amico, and R W Chantrell. Model of spin accumulation and spin torque in spatially varying magnetisation structures: limitations of the micromagnetic approach. *Journal of Physics: Condensed Matter*, 27(14):146004, mar 2015.

[90] John G. Simmons. Generalized formula for the electric tunnel effect between similar electrodes separated by a thin insulating film. *Journal of Applied Physics*, 34(6):1793–1803, jun 1963.

[91] Kamaram Munira, William H. Butler, and Avik W. Ghosh. A quasi-analytical model for energy-delay-reliability tradeoff studies during write operations in a perpendicular STT-RAM cell. *IEEE Transactions on Electron Devices*, 59(8):2221–2226, aug 2012.

[92] K. Watanabe, B. Jinnai, S. Fukami, H. Sato, and H. Ohno. Shape anisotropy revisited in single-digit nanometer magnetic tunnel junctions. *Nature Communications*, 9(1), feb 2018.

[93] N. Caçoilo, S. Lequeux, B.M.S. Teixeira, B. Dieny, R.C. Sousa, N.A. Sobolev, O. Fruchart, I.L. Prejbeanu, and L.D. Buda-Prejbeanu. Spin-torque-triggered magnetization reversal in magnetic tunnel junctions with perpendicular shape anisotropy. *Physical Review Applied*, 16(2), aug 2021.

[94] Sabpreet Bhatti, Rachid Sbiaa, Atsufumi Hirohata, Hideo Ohno, Shunsuke Fukami, and S.N. Piramanayagam. Spintronics based random access memory: a review. *Materials Today*, 20(9):530–548, nov 2017.

[95] S Yuasa and D D Djayaprawira. Giant tunnel magnetoresistance in magnetic tunnel junctions with a crystalline MgO(0 0 1) barrier. *Journal of Physics D: Applied Physics*, 40(21):R337–R354, oct 2007.

[96] X.-G. Zhang and W. H. Butler. Large magnetoresistance in bcc co/mgo/co and feco/mgo/feco tunnel junctions. *Physical Review B*, 70(17), nov 2004.

[97] Shoji Ikeda, Jun Hayakawa, Young Min Lee, Fumihiro Matsukura, Yuzo Ohno, Takahiro Hanyu, and Hideo Ohno. Magnetic tunnel junctions for spintronic memories and beyond. *IEEE Transactions on Electron Devices*, 54(5):991–1002, may 2007.

[98] Shinji Yuasa, Yoshishige Suzuki, Toshikazu Katayama, and Koji Ando. Characterization of growth and crystallization processes in cofeb/mgo/cofeb magnetic tunnel junction structure by reflective high-energy electron diffraction. *Applied Physics Letters*, 87(24), dec 2005.

[99] Y. S. Choi, K. Tsunekawa, Y. Nagamine, and D. Djayaprawira. Transmission electron microscopy study on the polycrystalline cofeb/mgo/cofeb based magnetic tunnel junction showing a high tunneling magnetoresistance, predicted in single crystal magnetic tunnel junction. *Journal of Applied Physics*, 101(1), jan 2007.

[100] S. Ikeda, K. Miura, H. Yamamoto, K. Mizunuma, H. D. Gan, M. Endo, S. Kanai, J. Hayakawa, F. Matsukura, and H. Ohno. A perpendicular-anisotropy CoFeB–MgO magnetic tunnel junction. *Nature Materials*, 9(9):721–724, jul 2010.

[101] Riki Shimabukuro, Kohji Nakamura, Toru Akiyama, and Tomonori Ito. Electric field effects on magnetocrystalline anisotropy in ferromagnetic fe monolayers. *Physica E: Low-dimensional Systems and Nanostructures*, 42(4):1014–1017, feb 2010.

[102] Mukund Bapna, Stephan K. Piotrowski, Samuel D. Oberdick, Mingen Li, C.-L. Chien, and Sara A. Majetich. Magnetostatic effects on switching in small magnetic tunnel junctions. *Applied Physics Letters*, 108(2), jan 2016.

[103] S. S. P. Parkin. Systematic variation of the strength and oscillation period of indirect magnetic exchange coupling through the 3d, 4d and 5d transition metals. *Physical Review Letters*, 67(25):3598–3601, dec 1991.

[104] Taehyun Kim, In Ho Cha, Yong Jin Kim, Gyu Won Kim, Andrey Stashkevich, Yves Roussigné, Mohamed Belmeguenai, Salim M. Chérif, Alexander S. Samardak, and Young Keun Kim. Ruderman–kittel–kasuya–yosida-type interfacial dzyaloshinskii–moriya interaction in heavy metal/ferromagnet heterostructures. *Nature Communications*, 12(1), jun 2021.

[105] Lihui Zhou, Jens Wiebe, Samir Lounis, Elena Vedmedenko, Focko Meier, Stefan Blügel, Peter H. Dederichs, and Roland Wiesendanger. Strength and directionality of surface ruderman–kittel–kasuya–yosida interaction mapped on the atomic scale. *Nature Physics*, 6(3):187–191, jan 2010.

[106] D. A. Garanin. Self-consistent gaussian approximation for classical spin systems: Thermodynamics. *Physical Review B*, 53(17):11593–11605, may 1996.

[107] H. Sato, P. Chureemart, F. Matsukura, R. W. Chantrell, H. Ohno, and R. F. L. Evans. Temperature-dependent properties of CoFeB/MgO thin films: Experiments versus simulations. *Physical Review B*, 98(21), dec 2018.

[108] Alina Crisan, Florin Vasiliu, Ionel Mercioniu, Cristina Bartha, Monica Enculescu, and Ovidiu Crisan. Annealing-induced high ordering and coercivity in novel l10 CoPt-based nanocomposite magnets. *Metals*, 8(6):466, jun 2018.

[109] R. A. McCurrie and P. Gaunt. The magnetic anisotropy of ordered equiatomic platinum cobalt. *Philosophical Magazine*, 19(158):339–347, feb 1969.

[110] Andrea Meo, Phanwadee Chureemart, Shuxia Wang, Roman Chepulskyy, Dmytro Apalkov, Roy W. Chantrell, and Richard F. L. Evans. Thermally nucleated magnetic reversal in CoFeB/MgO nanodots. *Scientific Reports*, 7(1), dec 2017.

[111] M. Ležaić, Ph. Mavropoulos, and S. Blügel. First-principles prediction of high curie temperature for ferromagnetic bcc-co and bcc-FeCo alloys and its relevance to tunneling magnetoresistance. *Applied Physics Letters*, 90(8), feb 2007.

[112] Thomas Bose, Ramon Cuadrado, Richard F L Evans, Roman V Chepulskii, Dmytro Apalkov, and Roy W Chantrell. First-principles study of the fe | MgO(0 0 1) interface: magnetic anisotropy. *Journal of Physics: Condensed Matter*, 28(15):156003, mar 2016.

[113] Jodi M. Iwata-Harms, Guenole Jan, Huanlong Liu, Santiago Serrano-Guisan, Jian Zhu, Luc Thomas, Ru-Ying Tong, Vignesh Sundar, and Po-Kang Wang. High-temperature thermal stability driven by magnetization dilution in CoFeB free layers for spin-transfer-torque magnetic random access memory. *Scientific Reports*, 8(1), sep 2018.

[114] Naoki Nozawa, Shin Saito, Shintaro Hinata, and Migaku Takahashi. Large uniaxial magnetocrystalline anisotropy for co50pt50 disordered alloy films with hexagonal-close-packed stacking structure by substituting pt with rh. *Journal of Physics D: Applied Physics*, 46(17):172001, apr 2013.

[115] T. Devolder, P.-H. Ducrot, J.-P. Adam, I. Barisic, N. Vernier, Joo-Von Kim, B. Ockert, and D. Ravelosona. Damping of CoxFe80-xB20 ultrathin films with perpendicular magnetic anisotropy. *Applied Physics Letters*, 102(2), jan 2013.

[116] Wayne Lack, Sarah Jenkins, Andrea Meo, Roy W Chantrell, Keith M McKenna, and Richard F L Evans. Thermodynamic properties and switching dynamics of perpendicular shape anisotropy mram. *Journal of Physics: Condensed Matter*, 36(14):145801, January 2024.

[117] J A Osborn. Demagnetizing factors of the general ellipsoid. *Phys. Rev.*, 67(11-12):351–357, June 1945.

[118] Johannes Ender, Mohamed Mohamedou, Simone Fiorentini, Roberto Orio, Siegfried Selberherr, Wolfgang Goes, and Viktor Sverdlov. Efficient demagnetizing field calculation for disconnected complex geometries in stt-mram cells. In *2020 International Conference on Simulation of Semiconductor Processes and Devices (SISPAD)*. IEEE, September 2020.

[119] M. Sharrock and J. McKinney. Kinetic effects in coercivity measurements. *IEEE Transactions on Magnetics*, 17(6):3020–3022, nov 1981.

[120] M.P. Sharrock. Time-dependent magnetic phenomena and particle-size effects in recording media. *IEEE Transactions on Magnetics*, 26(1):193–197, 1990.

[121] R W Chantrell, G N Coverdale, and K O'Grady. Time dependence and rate dependence of the coercivity of particulate recording media. *Journal of Physics D: Applied Physics*, 21(9):1469–1471, sep 1988.

[122] William Fuller Brown. Thermal fluctuations of a single-domain particle. *Physical Review*, 130(5):1677–1686, June 1963.

[123] Persistence of Vision Pty. Ltd. (2024). Persistence of vision raytracer (version 3.7). Retrieved from http://www.povray.org/download/.

[124] Kazi Asifuzzaman, Milan Pavlovic, Milan Radulovic, David Zaragoza, Ohseong Kwon, Kyung-Chang Ryoo, and Petar Radojković. Performance impact of a slower main memory: A case study of stt-mram in hpc. In *Proceedings of the Second International Symposium on Memory Systems*, MEMSYS '16. ACM, October 2016.

[125] A. Meo, S. Sampan-a pai, P. B. Visscher, R. Chepulskyy, D. Apalkov, J. Chureemart, P. Chureemart, R. W. Chantrell, and R. F. L. Evans. Spin transfer torque switching dynamics in cofeb/mgo magnetic tunnel junctions. *Physical Review B*, 103(5), February 2021.

[126] Asya Shpiro, Peter M. Levy, and Shufeng Zhang. Self-consistent treatment of nonequilibrium spin torques in magnetic multilayers. *Physical Review B*, 67(10), March 2003.

[127] Tomohiro Taniguchi, Satoshi Yakata, Hiroshi Imamura, and Yasuo Ando. Determination of penetration depth of transverse spin current in ferromagnetic metals by spin pumping. *Appl. Phys. Express*, 1, March 2008.

[128] W Boonruesi, J Chureemart, R W Chantrell, and P Chureemart. Temperature dependence of spin-transport properties and spin torque in a magnetic nanostructure. *Phys. Rev. B.*, 102(13), October 2020.

[129] Kuntal Roy. Estimating the spin diffusion length and the spin hall angle from spin pumping induced inverse spin hall voltages. *Physical Review B*, 96(17), November 2017.

[130] Xinde Tao, Qi Liu, Bingfeng Miao, Rui Yu, Zheng Feng, Liang Sun, Biao You, Jun Du, Kai Chen, Shufeng Zhang, Luo Zhang, Zhe Yuan, Di Wu, and Haifeng Ding. Self-consistent determination of spin hall angle and spin diffusion length in pt and pd: The role of the interface spin loss. *Science Advances*, 4(6), June 2018.

[131] Gyung-Min Choi, Jung Hyun Oh, Dong-Kyu Lee, Seo-Won Lee, Kun Woo Kim, Mijin Lim, Byoung-Chul Min, Kyung-Jin Lee, and Hyun-Woo Lee. Optical spin-orbit torque in heavy metal-ferromagnet heterostructures. *Nature Communications*, 11(1), March 2020.

[132] S Bhattacharjee, K Gupta, N Jung, S J Yoo, U V Waghmare, and S C Lee. Site preference of NH3-adsorption on co, pt and CoPt surfaces: the role of charge transfer, magnetism and strain. *Phys. Chem. Chem. Phys.*, 17(14):9335–9340, April 2015.

[133] S. S. A. Razee, J. B. Staunton, and F. J. Pinski. First-principles theory of magnetocrystalline anisotropy of disordered alloys: Application to cobalt platinum. *Physical Review B*, 56(13):8082–8090, October 1997.

[134] P Chureemart, R Cuadrado, I D'Amico, and R W Chantrell. Modeling spin injection across diffuse interfaces. *Phys. Rev. B Condens. Matter Mater. Phys.*, 87(19), May 2013.

[135] Y. Takeuchi, H. Sato, S. Fukami, F. Matsukura, and H. Ohno. Temperature dependence of energy barrier in cofeb-mgo magnetic tunnel junctions with perpendicular easy axis. *Applied Physics Letters*, 107(15), October 2015.

[136] H. Sato, M. Yamanouchi, K. Miura, S. Ikeda, R. Koizumi, F. Matsukura, and H. Ohno. Cofeb thickness dependence of thermal stability factor in cofeb/mgo perpendicular magnetic tunnel junctions. *IEEE Magnetics Letters*, 3:3000204–3000204, 2012.

[137] Eli Christopher Inocencio Enobio, Mathias Bersweiler, Hideo Sato, Shunsuke Fukami, and Hideo Ohno. Evaluation of energy barrier of cofeb/mgo magnetic tunnel junctions with perpendicular easy axis using retention time measurement. *Japanese Journal of Applied Physics*, 57(4S):04FN08, March 2018.

[138] N. Perrissin, S. Lequeux, N. Strelkov, A. Chavent, L. Vila, L. D. Buda-Prejbeanu, S. Auffret, R. C. Sousa, I. L. Prejbeanu, and B. Dieny. A highly thermally stable sub-20 nm magnetic random-access memory based on perpendicular shape anisotropy. *Nanoscale*, 10(25):12187–12195, 2018.

[139] R F L Evans, Q Coopman, S Devos, W J Fan, O Hovorka, and R W Chantrell. Atomistic calculation of the thickness and temperature dependence of exchange coupling through a dilute magnetic oxide. *Journal of Physics D: Applied Physics*, 47(50):502001, November 2014.